Addis Ababa University

Addis Ababa Institute of Technology

School of Mechanical and Industrial Engineering

Numerical Based Parametric Study on the Static Structural and Modal response of Composite UAV Wing

A Thesis Submitted to the school of Mechanical & Industrial Engineering, Addis Ababa Institute of Technology in Partial Fulfillment of the Requirements for the Degree of Master of Science in Mechanical Engineering (Mechanical Design)

By:

Fasil Erkyhun Marew

Advisor: Dr. Daniel Tilahun

Co-advisor: Mr. Muluken Masiresha (Ph.D. candidate)

March 2022

Addis Ababa University

Addis Ababa Institute of Technology

School of Mechanical and Industrial Engineering

Numerical Based Parametric Study on the Static Structural and Modal response of Composite UAV Wing

By:

Fasil Erkyhun Marew

Approved by Board of Examiners:

Dr. Daniel Tilahun	_____	_____
Advisor	Signature	Date
Mr. Muluken M. (PhD Candidate)	_____	_____
Co - Advisor	Signature	Date
Dr. Haileleoul Sahle	_____	_____
Internal Examiner	Signature	Date
Dr. Mulugeta Habtemariam	_____	_____
External Examiner	Signature	Date
Dr. Araya Abera	_____	_____
Chairman	Signature	Date
Dr. Yilma Tadesse	_____	_____
SMIE, Dean	Signature	Date
Dr. Ermias Tesfaye	_____	_____
PG Program Director	Signature	Date

DECLARATION

I hereby declare that the work which is being presented in this thesis, **"Numerical Based parametric study on the Static Structural and Modal response of Composite UAV Wing,"** is original work of my own has not been presented for a degree of any other university and all the resources of materials used for the thesis have been duly acknowledged.

Name: Fasil Erkyhun

Signature: _____

Date: _____

This thesis has been submitted for examination with my approval as a university advisor and Co-Advisor.

Dr. Daniel Tilahun Signature: _____ Date: _____

Advisor

Mr. Muluken Masiresha Signature: _____ Date: _____

(PhD Candidate)

Co-Advisor

ACKNOWLEDGMENT

My first and most sincere thank goes to God Almighty; without his help, all mercy, and endless love, the completion of this work would not have been possible. Next, I want to thank my advisor, Dr. Daniel Tilahun, for his supportive comments in completing this thesis. Also, I would like to thank my co-advisor, Mr. Muluken Masiresha for his valuable guidance.

I want to express my most profound appreciation to Mr. Nakachew Assefa for his unconditional support and giving me access to a high-performance computer for numerical simulations.

Finally, my greater appreciation goes to my family for believing in me and supporting me, and also, I would like to say thanks to my friends and to those of you who were on my side no matter what in every situation.

ABSTRACT

In this research, an Unmanned Aerial Vehicle (UAV) wing made of carbon epoxy composite material was used to investigate the wing static structural and modal response. The aerodynamic pressure load was calculated on ANSYS fluent by taking into account practical operational conditions. Two parametric studies were conducted where the first study had three models by varying the wing front and rear spar locations. The location of the front spar of model 1, model 2, and model 3 was at 18%, 22%, and 25%, whereas the rear spar was located at 62%, 65%, and 65%, respectively. On the other hand, the second parametric study had five different composite ply orientations of the wing skin, including [0/30/0/30/0], [0/45/0/45/0], [0/60/0/60/0], [0/90/0/90/0], and [-45/45/-45/45/-45].

Results from static structural analysis of varying spar locations showed that deformation has a maximum value at model 3 whereas bending and shear stress were maximum at model 2. On the other hand, deformation, bending, equivalent, and shear stress was minimum at model 1. The result from varying composite ply orientations showed that maximum and minimum deformation occurs at [0/30/0/30/0] and [0/90/0/90/0] ply orientations, respectively. The shear stress value was maximum at [-45/45/-45/45/-45]; Meanwhile, bending and equivalent stress were maximum at [0/30/0/30/0], while all stresses were minimum at [0/90/0/90/0]. From the modal analysis result, varying the spar location shows less effect on the natural frequency of the wing. Moreover, it was observed that model 1 had better structural performance than the other two models. On the other hand, the natural frequency of the first mode was maximum at [0/90/0/90/0] and minimum at [0/30/0/30/0], while in the last mode, the maximum and minimum values occur at [0/30/0/30/0] and [0/90/0/90/0], respectively.

In General, the study showed that when the wing front and rear spar are close to each other and when [0/90/0/90/0], wing skin ply orientation applied, the wing had a better structural performance.

Keywords: Static Structural, Modal, UAV, Composite Wing

TABLE OF CONTENTS

LIST OF FIGURES

LIST OF TABLES

NOMENCLATURE

UAV	Unmanned Aerial Vehicle
CFD	Computational Fluid Dynamics
ACP	Ansys Composite Prep- Post
NACA	National Advisory Committee for Aeronautics
FEM	Finite Element Method
C_L	Lift Coefficient
C_D	Drag Coefficient
k-ω `	K Omega
CFRP	Carbon Fiber-Reinforced Polymer
L	Lift
D	Drag
AOA	Angle of Attack
CLT	Classical Laminate Theory
c	Chord
b	Span length
UD	Unidirectional

CHAPTER ONE

1 INTRODUCTION

The wing is the most significant component of an Unmanned Aerial Vehicle (UAV). Its primary job is to create the lifting power that maintains the aircraft in the air (Sadraey, 2017). The UAV wing's design is crucial because it directly forms the aerodynamic structure of the aircraft. The structural design is based on the aerodynamic loads generated during each flight stage, including takeoff, climb, cruise, diving, and landing (Valavanis & Vachtsevanos, 2015). A UAV performance is highly impacted by the weight and strength of its components, where the contribution of the wing component to the overall UAV structural weight is significant. The Wing surface of the UAV is subject to high aerodynamic load due to the operational environment (Kurtulus, 2017). A typical wing construction comprises - spar, ribs, stringers, and wing skin. The spar is the longitudinal component that gives the high Wing stiffness, and the ribs are the transversal component of the wing which helps the wing skin stay in its aerodynamic shape. Whereas the wing skin covers the internal structure and helps to sustain the aerodynamic pressure load.

1.1 Background of the Study

Reducing the weight of the UAV's structure can accomplish longer flight endurance and higher speed; thus, lightweight materials are preferd (Yayli et al., 2017). The structural components of airplanes are made of Aluminum alloy material. Due to its lightweight, workability, and low cost. Currently, due to the mechanical characteristics, fatigue strength and toughness, and corrosion resistance of composites; Carbon and Glass fiber reinforced polymers have emerged as the most competitive material for aircraft wing construction (Kaushik, 2017)(Gloria et al., 2019).

Some of the requirements for aircraft Wing construction include; lightweight, reliability, passenger safety, strength, high aerodynamics performance, and all-weather operation capability. Glass, aramid, and carbon are typical reinforcing fibers in aerospace applications, whereas epoxies, Phenolic, Polyester, Polyimides, and PPS are polymer matrixes. The author also explained how reinforcements and matrices rose to

improve composites (Mangalgiri, 1999). When advanced composites are used instead of traditional metal constructions, the weight of the aircraft structure can be lower by around 25% to 30%. To conduct stress and strain analysis, the authors constructed a parametric modeling technique, parametric finite element model optimization design, and numerical simulation for the composite structure of a UAV Wing. Through composites optimization design, it lowered the entire mass of the wing by 41.3 percent, and the material utilization ratio was considerably raised (Zhang et al., 2011).

Over the four generations of composites, the application and development of composite materials in the aerospace sector have increased. Glass-fiber reinforced composites, High-Performance Composites in the Post-Sputnik Era, The New Markets, and the Characteristics of Properties emphasis on Hybrid Materials, Biomimetic Strategies, and Nan composites are the four generations. Composites offer a 20 percent higher strength-to-weight ratio than metals, with carbon fiber being the most widely used fiber among others (Arif et al., 2017). Carbon fiber, glass fiber, and Kevlar reinforced composites are the most common composite materials utilized in UAV Wings. Because of the differences in material properties, availability, and cost of various composites, careful material selection is required when using composites on UAV Wings. Carbon fiber reinforced polymer (CFRP) seems to have a density, strength, and modulus of elasticity advantage over glass fiber reinforced polymer (GFRP), but (CFRP) is more brittle (Verma, 2018).

The finite element method approach using ANSYS software is the current trend to evaluate the structural performance of the wing. (Kansan et al., 2014) has validated the finite element analysis on NACA 4415 UAV Wing structure using experimental method. Composites such as Carbon Fiber Fabric, Kevlar Veil, Honeycomb Cores can be used for different Wing parts. The author's experimented to obtain deflection of the wing under bending mode, and the result shows that the difference between the experiment and FE analysis have good agreement.

Numerical software ANSYS widely used a finite element analysis tool to determine most UAV Wings' structural and aerodynamic characteristics. (Fairuz et al., 2016) showed that a fluid interaction approach can help study Wing deformation's effect on aerodynamic performance. The static and fatigue life prediction on the wing can also be determined using ANSYS, which helps us evaluate the wing's performance (Kumar

et al., 2013). (Basri et al., 2019) has studied the structural performance of the NACA 4415 UAV Wing and the author used conventional aluminum alloy materials for the wing. The model has two spars and eight ribs, and the load is applied on the wing using Schrenk's Approximation by considering elliptical load distribution on the wing and zero lift load at the tip of the wing. The author conducted another paper on the same model for different composite materials with various ply orientations under different loading conditions to study the deformation and stress on the wing. As a result, this research focuses on using composite material to build UAV Wing and conduct static structural and modal analysis; the research will also show a parametric study on the wing.

1.2 Statement of the Problem

Because of its structural weight and aerodynamic load created during flight, the wing in the UAV is subjected to large deflection, significant stress, and higher natural frequency, which leads to severe structural failure and result in limited flying endurance. Previous research on the finite element analysis of composite wing has only incorporated either static structural or modal response, which is not adequate to study the structural performance of the wing. Moreover, their finite element analysis did not consider the practical aerodynamic pressure loading condition during the maneuvering of the UAV. On the other hand, researchers do not address the effect of spar location and composite ply orientation on the composite wing.

Therefore, in this research, the structural performance analysis of a composite UAV wing will be conducted under the practical aerodynamic pressure load. Moreover, the effect of varying spar locations and composite ply orientations on the composite UAV wing will be investigated.

1.3 Objective

1.3.1 General objective

The main objective of this research is to study the effect of varying spar location and ply orientation on composite UAV wing under practical aerodynamic pressure load using a numerical method.

1.3.2 Specific objective

This Study has the following specific objectives:

- To determine the aerodynamic pressure load using computational fluid dynamic (CFD).
- To investigate the effect of varying spar locations on the Wing deformation, stress, and natural frequency.
- To Investigate the effect of composite ply orientation on the wing skin's deformation, stress, and natural frequency.

1.4 Scope and Limitation

In this Study, the model used for finite element analysis was only one UAV type. In contrast, half of the Wing part was considered due to UAV symmetrical behavior. The Study carried out a practical aerodynamic analysis of the UAV using the ANSYS fluent module where static structural and modal analyses to determine the wing deformation, stress, natural frequency, and mode shape.

The whole simulation was limited to one critical flight condition by considering the design angle of attack. The Study wouldn’t include the remaining flight condition effects on the structural performance due to their lower significance on the result and time consumption. The parametric Study focuses only on the spar and Wing skin due to their significant effect on wing performance.

1.5 Significance

This research helps to determine the structural performance of the UAV Wing. With the structural failure of the Wing part, the performance of the UAV would decrease. In this regard, the simulation of the static and modal behavior of the wing helps us determine the deformation, stress, and mode of vibration during maneuvering the vehicle and assists the design of the wing that has high stiffness, which will sustain the load applied on it.

The numerical simulation by ANSYS software on the wing determines the current Wing structural behavior, suggesting the structure stiffness. Based on the analysis, the best spar arrangement and the ply orientation of the composite laminate on the wing will be recommended.

1.6 Organization of the thesis

This thesis has been organized into five chapters as follows:

Chapter one

The first chapter includes an introduction, detailed literature on the Background of the Study, a statement of the problem, objective, scope, limitation, and significance of the Study.

Chapter two

The second chapter contains a comprehensive overview of the literature on composite materials, aerodynamics, static structural analysis, and modal analysis of the wing.

Chapter three

The Study methodology includes the model specification and 3D modeling of the wing using modeling software such as solid work and blender. Second, the determination of aerodynamic load on the wing under a different angle of attack and the actual design angle of attack of the Wing model calculate on the ANSYS fluent module. Third, the finite element analysis procurers explained the model meshing and the Wing model boundary condition. Finally, the wing static structural and modal analysis would

conduct to determine the deformation, stress, and natural frequency value and deferent parameters study effect studied on the wing.

Chapter four

In the fourth chapter, the result from the static structural and modal analysis on the wing is discussed and briefly explained. Furthermore, a comparison of the different cases on the obtained result was also determined.

Chapter five

The last chapter, with conclusions, recommendations, and future works on the Study, explains the whole work.

CHAPTER TWO

2 LITERATURE REVIEW

2.1 Introduction

Because of its excellent mechanical properties, aircrafts used composite materials. Therefore, the choice of material on the wing, which seems to be the UAV's primary focus region, also directly affects the UAV's performance. Several studies on UAV Wing material have been published, with some publications reviewing wing materials and finite element analysis on wing aerodynamics load, static and modal analysis. In addition, different literature was reviewed regarding composite materials and finite element analysis.

2.2 Composite materials

The composite material consists of a strong carry load and weaker materials, while the stronger is the reinforcement, and the weaker is the matrix. The purpose of reinforcement is to improve the composite's mechanical properties, and standard composites used in aircraft are fiberglass, carbon fiber reinforced polymer, and aramid fiber (Maria, 2013).

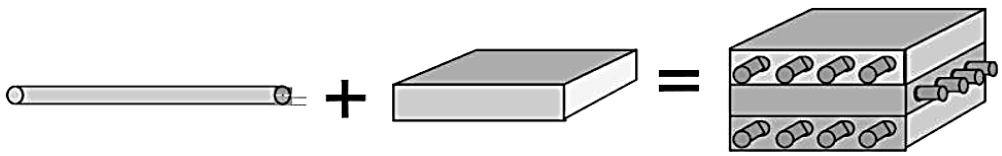

Figure 1 Composition of composite (Maria, 2013)

Rajak and others reviewed different papers about composite material, especially on fiber-reinforced polymer composites. Finally, the authors classified the composite material into three categories (Rajak et al., 2019).

Classification of composite Materials: -

1. Fiber-Reinforced Composites

- Synthetic fiber-reinforced composite

    - ✓ Glass Fiber-Reinforced Polymers (GFRPS)
    - ✓ Carbon Fiber-Reinforced Polymer (CFRP)
    - ✓ Graphene Fiber
    - ✓ Basalt Fiber-Reinforced Polymer (BFRP)
    - ✓ Kevlar Fiber-Reinforced Composites (KFRCS)

- Natural fiber-reinforced composite

    - ✓ Sisal fiber- reinforced with polyester composite
    - ✓ Kenaf fiber with Polylactic acid (PLA)
    - ✓ Flax fiber-reinforced polypropylene composites (FF/PPS)
    - ✓ Ramie fiber-reinforced polypropylene composites (RF/PPS)
    - ✓ Coir fiber-reinforced polypropylene
    - ✓ Palm fibers in low-density polyethylene (LDPE)

- Hybrid fiber

    - ✓ Hemp and glass fiber hybrid polypropylene composites
    - ✓ Palm/kenaf fiber-reinforced epoxy hybrid composite

2. Particle-Reinforced Composite
3. Sheet-Molded Composites

FRP replaces conventional materials and has a vast application area in the civil, mechanical, automobile, aerospace, biomedical, and marine.

2.2.1 Application of composite Material

Composite materials are used for structural applications, while short fiber reinforced epoxy resin composites have better mechanical properties. Therefore, they are used in many automotive, aerospace, and defense industries. For example, kevlar pulp is a short fiber and has high resistance to impact load (Hallad et al., 2018).

Polymer matrix-natural fiber composites show stronger, lighter, and cost effective applications like aerospace, automobiles, roofing structures, and interiors. The paper

Polymers are categorized as thermoplastic and thermoset-based natural fiber composites. In the first case, Polypropylene (PP), Polyethylene (PE), Polystyrene (PS), Polycarbonates (PC and Polyvinyl chloride (PVC) based composites are involved, whereas in the second thermoset, polyester, epoxy, and Polyurethanes. The most common natural fiber used in the polymer matrix is: - Flax, sisal, jute, banana, bamboo, coconut, flax, pineapple, hemp. Polyamide-Imide and epoxy are the most common polymers used in aerospace applications (Gowda et al., 2018).

(Vijayanandh et al., 2018) studied micro aerial vehicle (MAV) for the objective of selecting suitable composite material for high forward speed operation by withstanding high impact air load using (Fluid-Structure Integration) FSI simulation. Composites such as - Kevlar, Glass Fiber Reinforced Plastic (GFRP), and Carbon Fiber Reinforced Plastic (CFRP) were used for four different cases in which two cases for Horizontal Take-off and Landing (HTOL) and the other two cases for Vertical Take-off and Landing (VTOL) to predict the structural behavior of MAV by using static and dynamic analysis. The authors modeled the design by CATIA and have optimized it by FSI simulations with the help of Ansys Workbench 16.2 and from deformation. Von Mises stress analysis result shows that Kevlar MAV for high-speed HTOL operation and GFRP MAV has more suitable material for high-speed VTOL operation.

(Olaitan et al., 2017) conducted finite element analysis on the wing using composite graphite-epoxy for the application of aircraft Wings, while MATLAB and ANSYS were used to analyze the wing's structure. In the analysis, laminas are arranged in a different orientation to assemble laminate. In the laminate analysis, Hooke's law is applied to determine the strain and stress relationships between three different types of graphite-epoxies of low, high and extra modulus composites used, and in the ANSYS analysis distributed, a load of shear force is used to get the deflection. Bending moment from the analysis result, LM and UM have the best design property, whereas HM and UM have less relative deformation.

Glass fiber reinforced materials are used in many structures, especially in aerospace and automobile applications, and epoxy rose is the best polymer matrix for advanced composites (Rao et al., 2011). The author's studied a hybrid composite of glass and bamboo with two treated and untreated cases in which impact and dielectric strength analysis was conducted for a different combination. In the loaded molding box, the

material is prepared by using bamboo fiber, chopped glass, epoxy resin LY 556, and 1% NaOH solution for making the composite. After the test was completed, the authors found that alkali-treated bamboo has higher impact properties than untreated(RAO, 2011).

2.2.2 Classical laminate theory of composite material

Lamina is a typical composite material sheet and a fundamental building block. A fiber-reinforced lamina consists of many fibers embedded in a matrix material. Unidirectional fiber-reinforced lamina exhibits the highest strength and modulus in the direction of the fibers. Still, they have very low strength and modulus transverse to the fibers. At the same time, laminate is a collection of laminae stacked to achieve the desired stiffness and thickness (R. Jones,1975).

2.2.2.1 Stress-strain relation for an orthotropic material

Classical laminate theory (CLT) is used to determine the stress-strain behavior of lamina while expressing in the equation form of the k^{th} lamina in the laminate the variation of stress-strain through the thickness of laminate and the relation of force and moment of laminate to the strain.

$\varepsilon_i = \text{subj}$…… (Eq 2.1)

$$[s_{ij}] = \begin{bmatrix} \frac{1}{E_1} & \frac{-V_{21}}{E_2} & \frac{-V_{31}}{E_3} & 0 & 0 & 0 \\ \frac{-V_{12}}{E_1} & \frac{1}{E_2} & \frac{-V_{31}}{E_3} & 0 & 0 & 0 \\ \frac{-V_{13}}{E_1} & \frac{V_{23}}{E_2} & \frac{1}{E_3} & 0 & 0 & 0 \\ 0 & 0 & 0 & \frac{1}{G_3} & 0 & 0 \\ 0 & 0 & 0 & 0 & \frac{1}{G_{31}} & 0 \\ 0 & 0 & 0 & 0 & 0 & \frac{1}{G_{12}} \end{bmatrix} \quad \text{…… (Eq 2.2)}$$

Where:

E_1 ,E_2 and E_3 are young's moduli in the 1,2,3 direction

V_{ij} = Poisson's ratio in the ij direction

G_{23}, G_{31}, G_{12} = Shear moduli in the 2-3, 3-1, 1-2 direction

For unidirectional lamina the stress strain relation equation is: -

$$\begin{bmatrix}\sigma_1\\ \sigma_2\\ \tau_{12}\end{bmatrix}\begin{bmatrix}Q_{11} & Q_{12} & 0\\ Q_{12} & Q_{22} & 0\\ 0 & 0 & Q_{66}\end{bmatrix}\begin{bmatrix}\varepsilon_1\\ \varepsilon_2\\ \gamma_{12}\end{bmatrix} \quad \text{..... Eq (2.3)}$$

Where:

$$Q_{11} = \frac{E_1}{1-V_{12}V_{21}},\ Q_{22} = \frac{E_2}{-V_{12}V_{21}}, Q_{12} = \frac{V_{12}E_2}{1-V_{12}V_{21}} = \frac{V_{21}E_1}{1-V_{12}V_{21}},\ Q_{66} = G_{12}$$

For orthotropic lamina whose principal axis is aligned with the natural body axis

$$\begin{bmatrix}\sigma_X\\ \sigma_Y\\ \tau_{XY}\end{bmatrix} = \begin{bmatrix}\sigma_1\\ \sigma_2\\ \tau_{12}\end{bmatrix} = \begin{bmatrix}Q_{11} & Q_{12} & 0\\ Q_{12} & Q_{22} & 0\\ 0 & 0 & Q_{66}\end{bmatrix}\begin{bmatrix}\varepsilon_1\\ \varepsilon_2\\ \gamma_{12}\end{bmatrix} \quad \text{..... Eq (2.4)}$$

2.2.2.2 Lamina stress-strain behavior

The stress-strain relation in the x-y coordinate for a lamina of an orthotropic material under plane stress are

$$\begin{bmatrix}\sigma_X\\ \sigma_Y\\ \tau_{XY}\end{bmatrix} = \begin{bmatrix}\overline{Q}_{11} & \overline{Q}_{12} & \overline{Q}_{16}\\ \overline{Q}_{12} & \overline{Q}_{22} & \overline{Q}_{26}\\ \overline{Q}_{16} & \overline{Q}_{26} & \overline{Q}_{66}\end{bmatrix}\begin{bmatrix}\varepsilon_X\\ \varepsilon_Y\\ \gamma_{XY}\end{bmatrix} \quad \text{.....Eq (2.5)}$$

$$\overline{Q}_{11} = Q_{11}\cos^4\theta + 2(Q_{12} + 2\,Q_{66})\sin^2\theta\cos^2\theta + Q_{22}\sin^4\theta$$

$$\overline{Q}_{12} = (Q_{11} + Q_{22} - Q_{66})\sin^2\theta\cos^2\theta + Q_{12}(\sin^4\theta + \cos^4\theta)$$

$$\overline{Q}_{22} = Q_{11}\sin^4\theta + 2(Q_{12} + 2Q_{66})\sin^2\theta\cos^2\theta + Q_{22}\cos^4\theta$$

$$\overline{Q}_{16} = (Q_{11} - Q_{12} - 2Q_{66})\sin\theta\cos^3\theta + (Q_{12} - Q_{22} + 2Q_{66})\sin^3\theta\cos\theta \quad \text{..... Eq (2.6)}$$

$$\overline{Q}_{26} = (Q_{11} - Q_{12} - 2Q_{66})\, sin^3\theta\, cos\,\theta + (Q_{12} - Q_{22} + 2Q_{66})\, sin\,\theta\, cos^3\theta$$

$$\overline{Q}_{66} = (Q_{11} + Q_{22} - 2Q_{12} - 2Q_{66})\, sin^2\theta\, cos^2\theta + Q_{66}(sin^4\theta + cos^4\theta)$$

Where Θ angle of the principal material axis from the X-Y axis.

The stress-strain relation for the K[th] layer of a multilayered laminate the equation can be written as: -

$$\{\sigma\}_k = \left[\overline{Q}\right]_K \{\varepsilon\}_K \ldots\ldots\ldots\ldots\ldots\ldots\ldots\ldots\ldots\ldots\ldots\ldots\ldots\ldots\ldots\ldots\ldots\ldots \text{Eq (2.7)}$$

2.2.2.3 Stress and strain variation in a laminate

The laminate is assumed to be perfectly bonded, and the bond is infinitesimally thin and non-shear deformable. Therefore, the displacement is continuous across lamina boundaries, and their no restriction for flat, curved, or shell-like laminates.

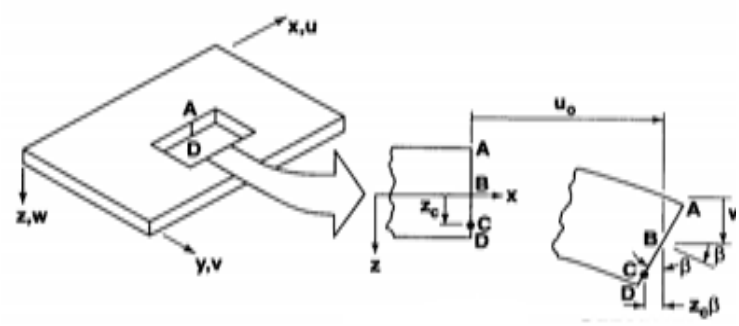

Figure 2 Geometry of deformation in an x-z plane (R.Jones, 1975)

$$U_C = U_O - Z_C\beta \ldots\ldots\ldots\ldots\ldots\ldots\ldots\ldots\ldots\ldots\ldots\ldots\ldots\ldots\ldots\ldots\ldots\ldots\ldots \text{Eq (2.8)}$$

Under deformation, the line ABCD further remains perpendicular to the middle surface is the slope of laminate in the middle surface x-direction.

$$\beta = \frac{\partial w_O}{\partial x} \ldots\ldots\ldots\ldots\ldots\ldots\ldots\ldots\ldots\ldots\ldots\ldots\ldots\ldots\ldots\ldots\ldots\ldots\ldots\ldots \text{Eq (2.9)}$$

The displacement u at any point z thickness in the laminate

$$U = U_O - z\frac{\partial w_O}{\partial x} \ldots\ldots\ldots\ldots\ldots\ldots\ldots\ldots\ldots\ldots\ldots\ldots\ldots\ldots\ldots\ldots\ldots\ldots\ldots\ldots \text{Eq (2.10)}$$

The displacement v in the y-direction

$$V = V_O - z\frac{\partial w_O}{\partial y} \quad \text{Eq (2.11)}$$

According to the Kirchhoff hypothesis, the strain value is simplified, and the remaining value is set as zero.

$$\varepsilon_x = \frac{\partial u}{\partial x}$$

$$\varepsilon_y = \frac{\partial v}{\partial y}$$

$$\gamma_{xy} = \frac{\partial u}{\partial y} + \frac{\partial v}{\partial x} \quad \text{Eq (2.12)}$$

For derived displacement in the equation (2.10) and (2.11), strains are: -

$$\varepsilon_x = \frac{\partial u_o}{\partial x} - z\frac{\partial^2 w_o}{\partial x}$$

$$\varepsilon_y = \frac{\partial v_o}{\partial y} - z\frac{\partial^2 w_o}{\partial y^2}$$

$$\gamma_{xy} = \frac{\partial u_o}{\partial y} + \frac{\partial v_o}{\partial x} - 2z\frac{\partial^2 w_o}{\partial x \partial y} \quad \text{Eq (2.13)}$$

Or

$$\begin{bmatrix} \varepsilon_x \\ \varepsilon_y \\ \gamma_{xy} \end{bmatrix} = \begin{bmatrix} \varepsilon^o{}_x \\ \varepsilon^o{}_y \\ \gamma^o{}_{xy} \end{bmatrix} + z\begin{bmatrix} k_x \\ k_y \\ k_{xy} \end{bmatrix} \quad \text{Eq (2.14)}$$

Where the middle surface strains are: -

$$\begin{bmatrix} \varepsilon^o{}_x \\ \varepsilon^o{}_y \\ \gamma^o{}_{xy} \end{bmatrix} = \begin{bmatrix} \frac{\partial U_o}{\partial x} \\ \frac{\partial V_o}{\partial y} \\ \frac{\partial U_o}{\partial y} + \frac{\partial V_o}{\partial x} \end{bmatrix} \quad \text{Eq (2.15)}$$

And the middle surface curvatures are: -

$$\begin{bmatrix} k_x \\ k_y \\ k_{xy} \end{bmatrix} = \begin{bmatrix} \frac{\partial^2 w_o}{\partial x^2} \\ \frac{\partial^2 w_o}{\partial y^2} \\ 2\frac{\partial^2 w_o}{\partial x \partial y} \end{bmatrix} \quad \text{..... Eq (2.16)}$$

By substituting the equation of strain variation through the thickness in the stress-strain relation, the stress in the kth layer can be expressed in terms of laminate mid surface strain and curvature as

$$\begin{bmatrix} \sigma_x \\ \sigma_y \\ \tau_{xy} \end{bmatrix}_k = \begin{bmatrix} \overline{Q}_{11} & \overline{Q}_{12} & \overline{Q}_{16} \\ \overline{Q}_{12} & \overline{Q}_{22} & \overline{Q}_{26} \\ \overline{Q}_{16} & \overline{Q}_{26} & \overline{Q}_{66} \end{bmatrix}_k \left[\begin{bmatrix} \varepsilon^o{}_x \\ \varepsilon^o{}_y \\ \gamma^o{}_{xy} \end{bmatrix} + z \begin{bmatrix} k_x \\ k_y \\ k_{xy} \end{bmatrix} \right] \quad \text{..... Eq (2.17)}$$

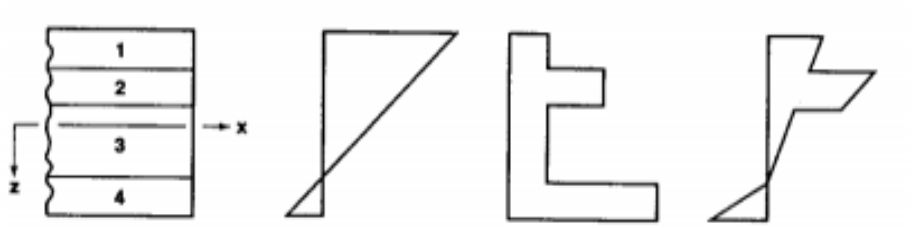

LAMINATE STRAIN DISTRIBUTION CHARACTERISTIC MODULI STRESS DISTRIBUTION

Figure 3 Variation of strain and stress through the laminate thickness (R. Jones, 1975)

2.3 Aerodynamics of Wing

If a vertical plane parallel cuts an aircraft Wing to the vehicle's centerline, the resultant section is called the airfoil or airfoil section. The generated lift and geometry of the airfoil have a high impact on the stall characteristics of the wing.

2.3.1 Aerodynamics theory on an airfoil

Following the term "NACA," a series of digits describe the shape of the NACA airfoils. There are six-digit series Wing sections and four-digit series Wing sections, according to NACA. The first digit specifies the maximum camber (m) in the percentage of the

chord (airfoil length), the second indicates the position of the maximum camber (p) in tenths of a chord, and the last two numbers define the maximum thickness (t) of the airfoil in the percentage of the chord. For example, the NACA 4412 airfoil has a maximum thickness of 12% and a camber of 4% situated 40 percent back from the airfoil leading-edge (or 0.4c) (http://airfoiltools.com/airfoil/naca4digit).

The flow of air in the airfoil and any other shape inclined to the flow direction shows the pressure of air on the above surface reduced and on the lower surface increased. The resulting pressure difference creates a net force that pushes the wing upward and backward. The wing is the main part of the aircraft, which develops the resultant lift force by using the pressure difference in the upper and lower surface of the wing and placing the aircraft in the air during takeoff and flying. The resultant lift force will split into the lift and drag force components. It also found that a much greater lift force creates than the drag one in curved airfoil surfaces (Dwivedi, 2007).

2.3.2 Pressure distribution on the wing

The pressure distribution, lift and drag coefficients in the airfoil change as the angle of attack. The following parameters determine the UAV's flight condition where the pressure distribution is not evenly distributed in the airfoil.

2.3.2.1 The angle of attack (AOA)

The angle between the direction of airflow and the wing's chord line greatly affects the generation of lift in the wing. Therefore, although the AOA may be positive or negative and will produce lift in both cases, it can also have no lift if we tilt the airfoil at a negative angle.

2.3.2.2 Lift curve

The lift curve shows the lift coefficient (CL) value with the angle of attack. It shows a zero-lift angle of attack and stalls angle which is the angle of attack where the maximum lift coefficient occurs that airfoil after that the lift coefficient tend to decrease.

2.3.2.3 Drag curve

This curve shows the relation between the drag coefficients with angle of attack (AOA). The drag is at least near 0 ^{o} and increases very slowly until stalling angle and then increases rapidly after that.

2.3.2.4 Lift to drag ratio curve

The most important parameter in the Wing Airfoil gives us the best flight condition. It can be determined using the maximum lift/ drag coefficient value and the corresponding angle of attack.

Analytically the lift and drag force can be calculated as: -

$$L = ½ C_L . \rho . V^2 . S \quad \text{Eq (2.18)}$$

$$D = ½ C_D . \rho . V^2 . S \quad \text{Eq (2.19)}$$

Where: - L = lift force, C_L = lift coefficient, ρ = air density, V= the airfoil velocity S= Wing area, D = drag force and D_L= drag coefficient (Dwivedi, 2007).

2.3.3 Aerodynamic load analysis using CFD

(Hasan et al., 2019) Conducted aerodynamic analysis on HALE UAV wing using finite volume method in the ANSYS fluent. The Wing geometry was modeled with half Wingspan, root chord a, tip chord, and Airfoil 27.709 m, 3.148 m, and 1.889 m, NACA 4415, respectively. The authors state grid generation was conducted in the rectangular fluid domain of 5c in the inlet, above, and below domain, while 20 c behind the wing and 2b from the tip of the wing where c and are chord and span length, respectively. Meshing parameters include 50 divisions with ten bias factors in the Wing edge, while the inflation layer is set as 20 with a 1.2 growth rate. Pressure-based, steady-state, and incompressible flow boundary conditions were considered, and for simulation, 2nd order accuracy with input parameters at h = 15000m operating condition was used. Two turbulent models, Spalart Allmaras and SST K-ω used in the solver with -4˚ to 18˚ Angle of Attack (AOA) and 97.22 m/s inlet velocity used. Both models show they have a small variation in the lift coefficient, and SST K-ω has fewer values than other

models. The higher lift coefficient showed 16^0 angles of attack for all models in another case; the drag coefficient has the same values. It is also seen that as the angle of attack increase, the pressure gradient in the upper surface Wing decrease and increase on the lower surface. In contrast, the velocity gradient increases on the upper surface and decreases on the lower surface.

(Eftekhari & Al-obaidi, 2019) investigated the aerodynamic characteristics of the NACA 0012 Wing using numerical and wind tunnel experiments. C type grid method used to mesh the Wing model while the boundary model with 20 chords away from the geometry and to achieve the wall Y^+ and for accuracy the following mesh parameters selected: - First cell height selected as one × 10^-5, entire fluid domain 10 mm and edge sizing 0.1 mm while 1.3 million cells generated as fine mesh. In The paper, the numerical Setup considers the flow as incompressible. The Spalart-Allmaras turbulence model was selected for three Reynold's numbers of 1 × 105, 2 × 105, and 3 × 105, while the angle of attack was 0 to 90 degrees. The result shows lift coefficients increase until 32 ^{o,} and the corresponding values measured CL of 0.58, 0.63, and 0.65 at Re of 1 × 105, 2 × 105, and 3 × 105, respectively. On the other hand, the drag coefficient is lower at 0^o angles and increases to 90^o. The authors validate their result with a wind tunnel experiment with 13.1m/s and lift and drag coefficients for 0° to 20° angle of attack, and the result has 13% variation at 20 ^{o} AOA in and 3% at below 15 ^{o} AOA. This is because of the increase of wall Y+ at the leading edge.

The aerodynamics of aircraft Wings were conducted using ANSYS fluent in the paper 3D, the geometry of the wing was modeled using NACA 2415 airfoil with 100mm for root and 18mm for root and tip chord, respectively, while span length was 177mm. Unstructured tetrahedral mesh with 10 mm Maximum faces size, 15 mm Maximum size, 1.2 Growth Rate, and 0.1 mm first layer thickness was set for the mesh parameters. The turbulent Spalart-Allmaras model was used because of the low Mach number, while the solver used constant air property and different angles of attack of 3^0,5^0,8^0,$10^{0,}$ and 12^0. From the analysis result, higher CL at 12^0 with a value of 0.5344 and a high lift to drag ratio L/D found at 5^0 angles of attack with a value of 16.60 determined (Jain et al., 2016).

A comparative study of the NACA 4412 Wing was conducted using three different methods of the newly designed aerodynamic analysis tool, XLFR5 and ANSYS-Fluent.

In contrast, the nonlinear numerical lifting-line method was applied to all solvers (Körpe, 2019). The authors use a 30-time chord length for the boundary layer of the wing in the ANSYS fluent, and in the mesh method, prism cells are used for the element type. At the same time, the first height is calculated as 0.015 mm by considering the wall Y^+ value as 1and 61 inflation layers and a 1.1 growth rate applied on the mesh control parameters with this values maximum of 0.95 skewness gained. On the other hand, in the solver, 1% turbulence intensity and 1600 iterations were used, and the $\gamma - Re\theta$ SST model was used for convergence purposes; the authors state the results are accurate when the Cl and CD fluctuate within the range of ±0:001. The result of those three methods shows they have the same effect until 15^0 angles of attack, and after that, the fluent result diverges from the aerodynamic tool. The maximum lift coefficient was obtained at 18^0 Angle of Attack in all three methods, with a value around 1.4 obtained.

(Mosaad & Abdelmonaem, 2019) conducted CFD on Boeing 737-700 NG aircraft and its airfoil at a mean chord length of 6.55m in the study mesh generation of 3D airplane model has 0.006 first layer thickness for the corresponding Y+ value of 750 with five layers of inflation and 1.2 growth rate in this parameter 5.5 - million unstructured grid created. In the 2D airfoil 780,000-element, the structured grid was generated. The authors selected the Spalart-Allmaras model for the 3D model and K-ε for the 2D airfoil; the boundary conditions are steady-state Pressure-Velocity Coupling scheme and inlet velocity as 150 m/s used for the calculations. The simulation result shows the instability of the solution initially due to low mesh quality. After improving mesh quality, the lift and drag coefficients converge below 300 iterations with Cd and Cl values of 0.056 and 0.245, respectively, in the Airfoil of 0° and 1.8° AOA. The result shows both lift and drag coefficients are higher at 1.8 AOA but, the pitching moment coefficient (Cm) has less value.

2.4 Static structural analysis of UAV Wing

(Basri et al., 2019) studied the structural design of composite UAV tubercles wing to improve performance of Wing structure. They use Airfoil of NACA4415 geometrical model of tubercle leading edge (TLE) modeled and imported into the static structural domain in ANSYS Workbench 17.0. in the first stage, two alternative Structural configurations for rib-reinforced and Structural configurations for monocoque-foam-

reinforced modeled and generated mesh for both alternatives. Then, the second stage of the composite construction of the wing is carried out in the ACP domain of ANSYS Workbench 17.0 for both options. They have different materials of carbon fiber fabric and styrene-acrylonitrile (SAN) foam. The final stage is used to determine the response of the structures subjected to the external influence of the load applied. Finally, from analysis results and comparison, the author concluded that the monocoque-foam reinforced design configuration has better structural performance, reducing 50.72% of deformation and 35.88% of stress compared to rib-reinforced design.

The structure and modal analysis of subsonic aircraft Wings with Airfoil NACA 4412 was selected for the wing, and the chosen material for this wing is aluminum alloy and titanium alloy. The 3D model was done on ANSYS while the chord length of one end is 0.4 m, the other end is 1m, and the Wing length is 5m. The authors fixed one end and applied 500 pa pressures on the top and gravitational force. The structural and modal analysis result shows that total deformation, equivalent stress, and strain are less in aluminum alloy, making alloy more preferable for subsonic aircraft (Kathiravan et al., 2018).

The paper aimed to identify the proper material for aircraft Wings was studied using the finite element method (Kumar Das & Roy, 2018). The authors designed the wing using Catia while the model has 15 ribs and two spars, and also the load applied is 500 Mpa at the bottom of the center of pressure, whereas the boundary condition is fixed on one end and free the other end with 6 degrees of freedom. The static structure is conducted under different speeds for the following materials Epoxy-carbon UD, Epoxy S-glass UD, Aluminum 2024 T3, Epoxy-carbon Woven, Epoxy E-glass Ansys result shows the deformation of the Wing increases as rotational speed increases, and Epoxy-carbon has less deformation when compared with other material.

Structural analysis of the NACA 2412 3D model using two different composites of carbon fiber and aramid fiber has been studied. The ANSYS analysis result shows carbon fiber has less deformation, less strain, and less stress than aramid fiber (Sawadi, 2017).

The research was conducted on NACA0016 using AL-2024, AL-6061, AL-7075) for the ribs and Kevlar in which DESIGN FOIL software and MS excel spreadsheets were

used for the coordinate generation, and the 3D model was done on CATIA. The author boundary conditions applied for the wing from translational and rotational movements with the application pressure of 200 MPa resulted in al-7075-t6 & Kevlar having less stress (Aliywy, 2017).

Structural analysis on A300 flight Wing conducted by two materials AL alloy and AL 7068 and NACA 64-215 selected for airfoil then the Catia model is imported to ANSYS. The two materials were compared for static analysis where boundary condition is taken on the top of the wing after finding the equivalent stress and deformation. The result shows aluminum 7068 can replace the AL alloy (Sureka & Meher, 2015).

Structural and modal analysis of the composite wing was studied by considering three fibers Wings plain, aluminum - carbon fiber, and aluminum - aramid fiber. The authors used Catia to model the wing imported into ANSYS. In the structural analysis, deformation, stress, and strain were calculated, whereas, in the vibration analysis, wing deformation and frequency were calculated. The analysis result shows deformation and stress were less for carbon fiber, and the frequencies were less for aramid fiber; however, the hybrid composite aluminum Wing produces good results (Saripalli et al., 2015).

Study the effect of S Glass, Kevlar 49, and Boron Fiber materials on aircraft wing using FEM analysis where the airfoil was selected from NACA library and the 3D model is on CAD & PRO/ENGINEER. The result shows in the case of static analysis, boron fiber has less stress, and the modal analysis result shows S glass has fewer frequencies. In contrast, the buckling analysis S glass has better performance, and the author concludes that adding ribs and spars increases the wing's strength and S glass had better than the others (Kavya & Reddy, 2015).

Experimental research on the Wing model consists of two spars, 25 ribs at the different Wing positions, and three parts of skins as major structural components. Geometrical modeling of NACA 4415 done on Solid work and imported to Abaqus/CAE. Carbon Fiber Fabric, Kevlar Veil, Honeycomb Cores are used for different Wing parts. The authors also experiment to obtain deflection of the wing under bending mode. The result

shows that the difference between the experiment and FE analysis ranges from 0.35% to 16.4%, which is good it's less than 20% (Kansan et al., 2014).

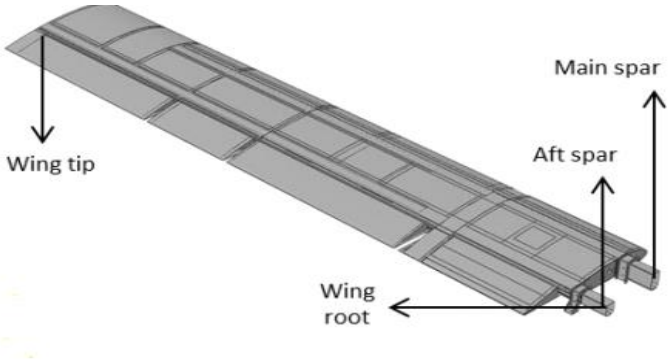

Figure 4 UAV Wing geometry (Kansan et al., 2014)

The wing comprises CFRP composites, while linear static was studied using ANSYS. The authors consider pressure, drag, and gravity; the load on the aircraft Wing is assumed to be uniformly distributed loads and a magnitude of 56 KN/m. The wing is ideals as a cantilever beam, and ANSYS is used to model the wing as a shell element. From the analysis result, the maximum stress on the preliminary model is more than the permissible stress of CFRP. In contrast, the refined Wing model, which has a 6mm thickness in the top panel, has less stress and is uniformly distributed on the Wing (Mathai et al., 2014).

Structural analysis on the FEM modeled UAV tail beam, made from composite material, has been done on the MSC/NASTRAN software package. The authors used Von Misses stress criterion for the strength check of the isotropic materials, and the Tsai-Wu failure theory is employed for composite materials (Stevan, 2013). Experimental testing on the UAV was done for ultimate loading condition, and the deflection was measured. A comparison of the structural analysis with experiments shows a good correlation between the results.

The wing was treated as a cantilevered shell and used two materials of Carbon/epoxy and aluminum alloy laminated composite structure where airfoil NACA 4412 was selected for a subsonic aircraft Wing. The wing is tapered at one end with chord length at the free end is 0.8m and at the fixed end is 1.8m. The author considered self-load due

to gravity and combined load for analysis and analysis ANSYS (Pugazhenthi et al., 2018).

2.5 Modal analysis of UAV Wing

The modal analysis is used to determine the dynamic behavior of the wing, mainly natural frequency and mode shape. The wing's geometry is taken from the A300-600R aircraft and modeled in Catia according to its specification. At the same time, the numerical modal analysis is done on ANSYS workbench 14.0 by considering the wing as a cantilever beam that is fixed at one end in the root chord, and aluminum is used for defining the material. The author has also done theoretical calculations using Euler-Bernoulli Beam's theory. The result shows a small amount of difference occurred, validating the FE model of modal analysis (Khadse & Zaveri, 2015).

Studies on modal analysis of UAVs by designing the airfoil for three different Wing sections are attached with different angles from each other. The material used is lightweight Mylar and has good physical properties (Anderson et al., 2015).

(Bayraktar & ALI, 2019) studied free vibration on aircraft Wing using theoretical and numerical methods. The theoretical calculation was based on Euler- Bernoulli beam theory for every mode by taking data from airfoil tools.

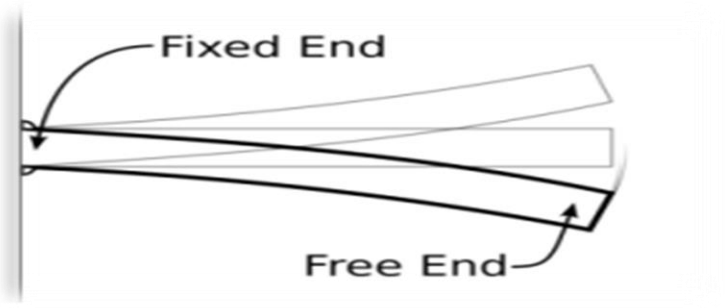

Figure 5 Cantilever beam (Bayraktar & ALI, 2019)

(Krishna et al., 2016) conducted Modal analysis of aircraft Wings with two models, one original and the other modified model. NACA 4412 airfoil was used for modeling. Four different materials: aluminum alloy T6061, C-fiber glass, boron fiber, and Ceramic fiber, were used separately for the original model, and the modified model combination of aluminum with rest fibers was used. The final result from the vibrational analysis of

three modes shows the frequency is less for modified ceramic, and the deformation is more than the original.

Flutter is one of the main vibration problems in aircraft operation. It occurs when one of the damping values becomes negative; therefore, determining the value of natural frequency and mode shape is important in using ANSYS to prevent such problems. The author models the aircraft Wing using solid works, and the material selected for the skin is canvas but not included in the analysis. At the same time, the remaining part is aluminum alloy (M., 2014). In the finite element analysis, tetrahedron mesh is used with it has 196 610 nodes and 94 986 elements. At the same time, the boundary condition considers the wing as a cantilever beam that is fixed at one end. From the analysis result, six bending and twisting modes with their perspective frequencies are presented: 3.22, 11.32, 23.35, 34.22, 59.60, and 68.83 were determined.

Study on the wing to find the natural frequency of the aircraft Wing to calculate the resonance and prevent the wing's deformation due to the critical vibration. The authors considered the pre-stress condition to analyze the total Wing deformation with its respective nodal displacement. At the same time, the result of the analysis shows the deformation ranges from 0.12 m to 0.174 m, and the frequency ranges from 73.93 Hz to 1359.8 Hz, which helps to calculate the resonance and prevent the failure of the components of the Wing structure (Saran et al., 2017).

2.6 Summary of literature and Gap

According to the literature discussed above, the material used to make a UAV wing significantly impacts its performance. Therefore, researchers are focusing on substituting conventional materials such as aluminum alloy and titanium alloy with high strength-to-weight ratio composite materials. The finite element analysis of composite wing materials shows that carbon fiber polymer composite and glass fiber polymer composite have better structural performance. Even if glass fiber polymer composite has good behavior on the modal response, it has high density and less strength than carbon, indicating we should apply carbon fiber polymer composite for the UAV wing.

It is observed that the finite element analysis of composite wing of most researches are conducted either static structural or modal analysis in their simulations which is not adequate to study composite wing rather, they should include both analyses. Furthermore, several studies used only gravitational loading even though the aerodynamic pressure load during the flight was the main load on the wing. The influence of spar location and different ply orientations was given less attention in their study. As a result, this study aims to fill the gaps in previous research.

CHAPTER THREE

3 METHODOLOGY

3.1 Introduction

The methodology begins with gathering and analyzing relevant data from various sources. The finite element method (FEM) is a method for approximate computing solutions to boundary value problems. These inaccurate answers are obtained using numerical techniques and computational simulations, also known as finite element analysis. Converting the physical domain into finite elements and meshing the resulting set of elements, known as a finite element mesh, is part of the method. The three primary stages in a conventional FEM technique are preprocessing, solution, and postprocessing (Hutton, 2004). The ANSYS workbench 2021 Rb2 version of numerical simulation software was used for all analyses on a computer with 16 GB RAM and a Core i7 processor. The first step was choosing the right material and defining the UAV Wing's geometrical parameters and operating conditions. The simulation model will start when the geometrical specification of the wing, the kind of airfoil, cord length dimension, and Wingspan dimension have been determined. Next, the airfoil coordinates are imported in text from MS Excel, and the surface body is created for all parts using solid works modeling software. In contrast, the Wing skin is extruded to the end of the Wingspan to develop the aerodynamic shape of the wing.

Computational fluid dynamics via ANSYS fluent were used to calculate the aerodynamic load acting on the wing. The domain and all of the input parameters derived from the literature and the operating conditions at 2000 m above sea level would be considered. The wing's design angle of attack will obtain the maximum lift-to-drag ratio. The computed aerodynamic pressure load will be employed as the loading condition for static and modal analysis. The fluid domain size and fluent mesh will be created initially, followed by selecting a turbulence model depending on the solution requirements. Finally, the solver will run until the result converge.

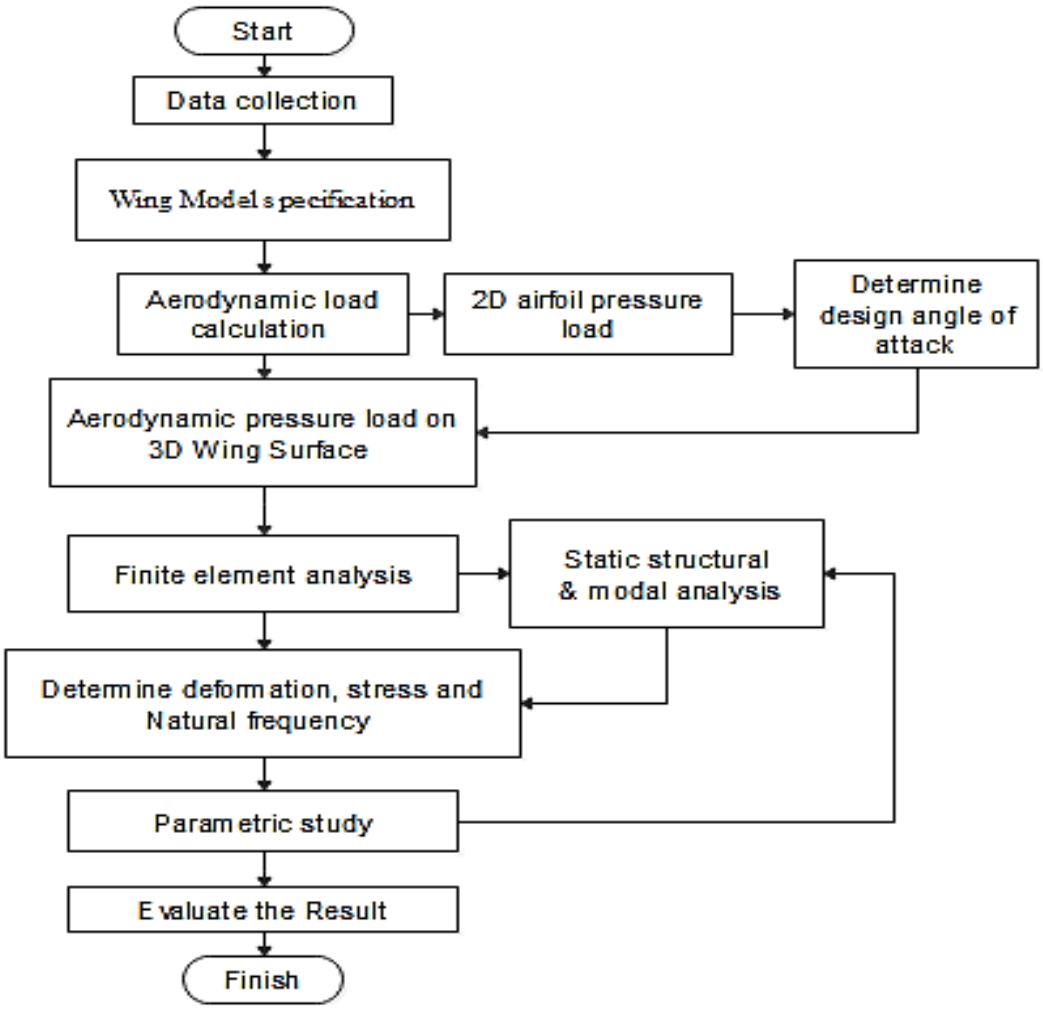

Figure 6 Methodology flow chart

The finite element analysis used the static structural and modal analysis modules. The ANSYS Workbench is used to calculate the Wing model's deformation, stress, and natural frequency. Preprocessing, process, and post-process are the three main processes in the analysis. The analysis begins with creating a mesh to define the elements and nodes, with the mesh quality and type of mesh determined under various types of literature that use the ANSYS manual. The UAV Wing's boundary condition could primarily be considered as a cantilever beam that only employs half of the wing due to its symmetrical nature, with the wing fixed on one end and free on the other. The output parameters are total deformation, maximum shear stress, bending stress, and natural frequency. The effect of spar location and ply orientation on the Wing skin will be investigated using various cases. Finally, the result obtained from the different simulations will compare, and results will be evaluated.

3.2 Wing Geometry description

The Wing shape is modeled using the surface method in SolidWorks, and it has a constant chord length of 0.5 m and a span length of 2.5 m, with a NACA 4415 airfoil for the wing's aerodynamic profile as well as a wing skin thickness of 1 mm (Basri et al., 2019). The Wing airfoil coordinates were generated using the NACA airfoil library website. The final geometry was imported into ANSYS using the IGES format.

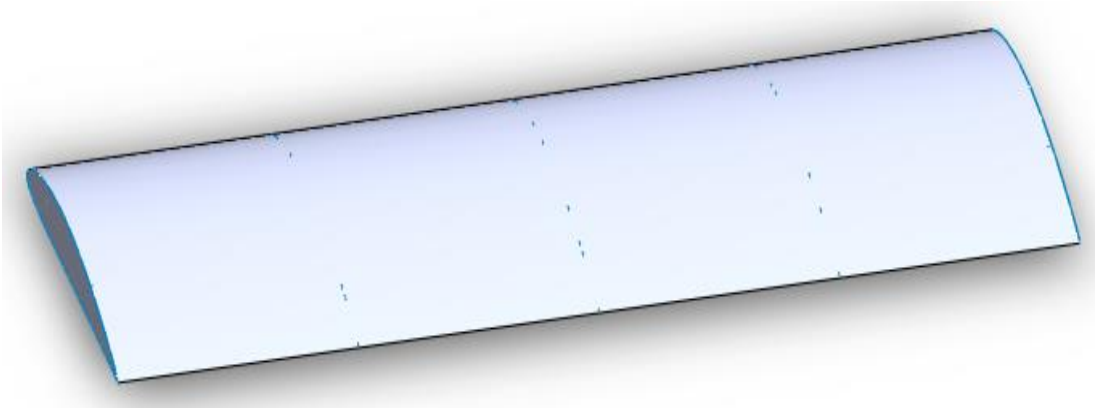

a) Outer structure

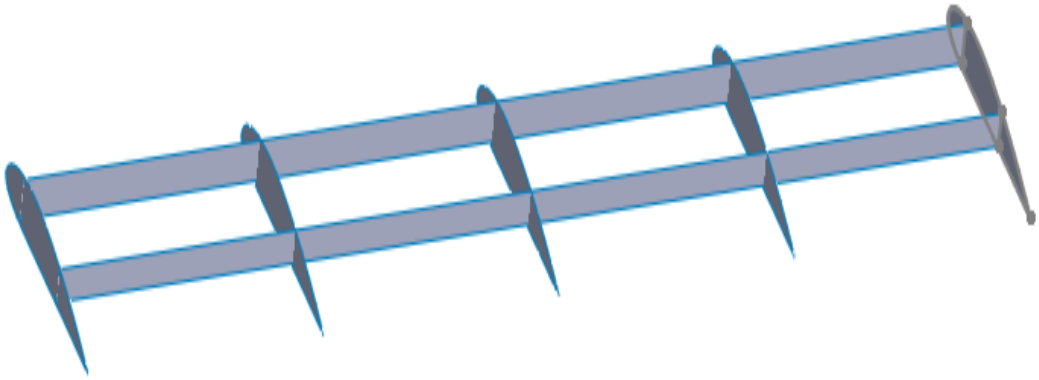

b) Inner structure

Figure 7 Wing 3D Model

3.3 Aerodynamic pressure load

The ANSYS, workbench 21.2 simulation software, was used in this thesis to perform a Computational Fluid Dynamics (CFD) analysis of a Wing to determine the aerodynamic pressure load on the Wing surface, which can be used as a boundary condition for the static structural and modal analysis. The aerodynamic characteristics of the NACA 4415 UAV Wing model were calculated under the given operating conditions.

3.3.1 Aerodynamic load on a 2D airfoil

The design angle of attack of the wing at which the maximum value of the ratio of lift coefficient to drag coefficient occurs. The lift and drag coefficient for each angle of attack will be determined, and from the result, the highest ratio is considered as the design angle. It is the input parameter for the 3D Wing aerodynamic load calculation.

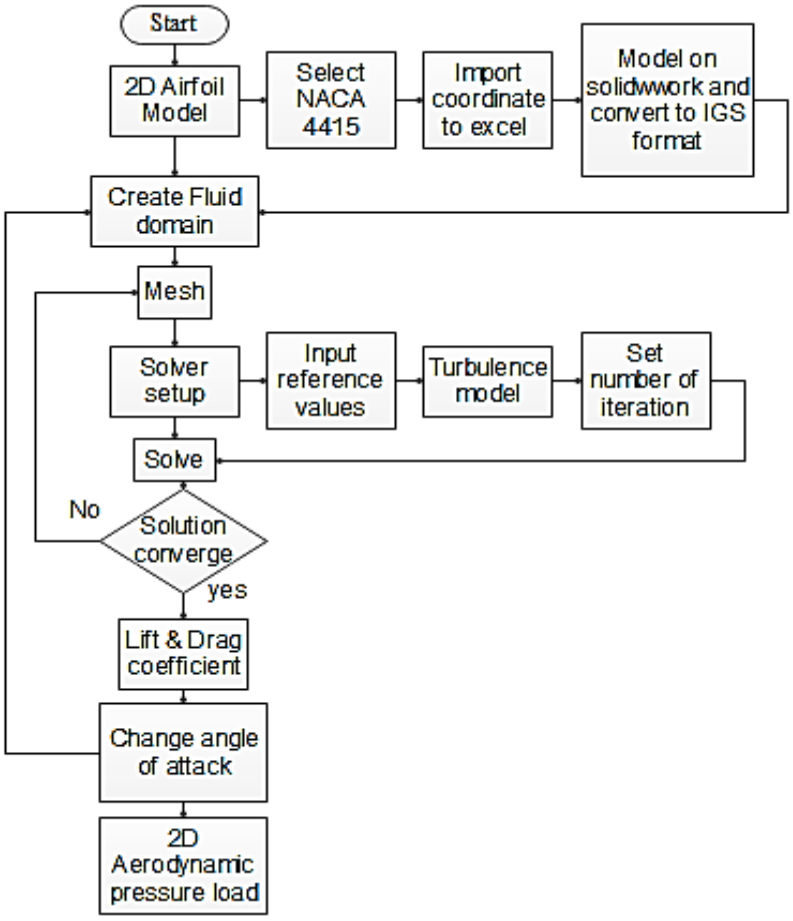

Figure 8 Ansys Fluent flow chart

3.3.1.1 Fluid Domain

The rectangular fluid domain illustrated in Figure 11 is used, and its dimensions are determined by the chord length (c), where the length from the leading edge to the trailing edge of the wing, and span length (b), where the length from root to the tip of the wing. The domain has six wall surfaces, including one symmetry wall attached to the Wing, three inlet and outlet walls, and one symmetry wall attached. Domain 5c inlet side is away from the wing's leading-edge; domain 20c outlet side is away from the

wing, the upper and lower wall domains are 5c away from the Wing (Khchine & Sriti, 2017).

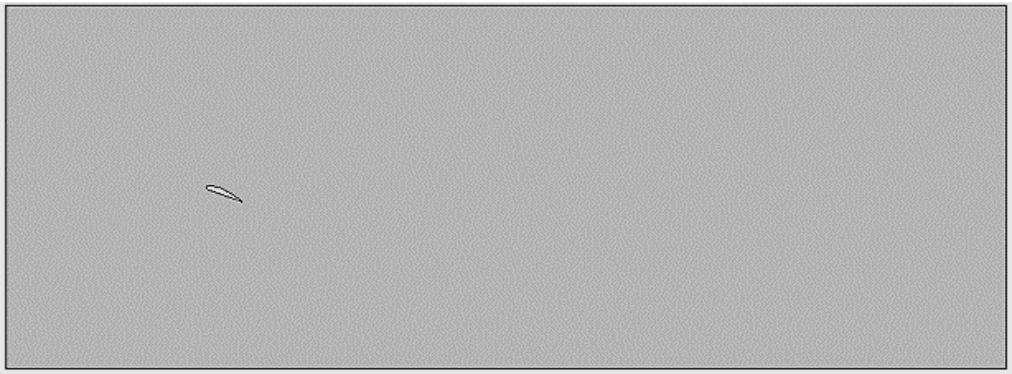

Figure 9 Fluid Domain

The critical flight condition of the airfoil is determined by using a lift to drag ratio Vs. The angle of attack of the wing where the maximum value is considered as the critical flight condition.

3.3.1.2 Mesh generation on fluent

Generating fine mesh is very important for obtaining the correct solution. Before proceeding to the solver stage of CFD, the unstructured tetrahedron meshing method with an independent patch algorithm was selected due to the model's shape having a high curvature feature. The final mesh parameter set as a maximum element size of 30 mm and with a 1.2 growth rate is set for the global mesh. The Wing edge is divided using 300 divisions for finer mesh around the airfoil, while the minimum size of the element is 5mm. The boundary layer and first layer height estimation are the other important parameters in the CFD mesh used for the turbulent model. To satisfy this model, the value of **y+** should be less than one (Khchine & Sriti, 2017).

Hence, to get the value of y+<1, the layer's first height is estimated using Eq. (3.1).

$$y^+ = \frac{yu*}{v} \quad \text{..... Eq. (3.1)}$$

It is possible to estimate the value substituting y^+ as one in Eq. (3.2)

$$y = \frac{vy^+}{u*} \quad \text{.....Eq. (3.2)}$$

$u* = \sqrt{\frac{\tau_p}{\rho}}$……...……Eq. (3.3)

Where: -

y is the first layer height from the Wing surface

u* is the friction velocity

ρ air density

υ kinematic viscosity

τp friction coefficient

μ Dynamic viscosity

Re = (ρ*l*v)/ μ = (1.225Kg/m^3*0.5* 35 m/s)/ 1.7974 10^{-5}

= 1192695

For external flow: -

$\tau p = 0.058 * Re^{-0.2}$

$0.058*(1192695)^{-0.2} = 3.53*10^{-3}$ m/s

u * = 0.05368

Finally, after calculating the first layer height value as 0.015 mm by setting y+ as a target value of less than one, then set the y value as 0.015 mm and 20 inflation layers with the growth rate of 1.2 for finer mesh. The final mesh for the CFD analysis is 86112 elements with maximum skewness of 0.86, which is very acceptable for the CFD analysis.

(a) Mesh in the 2D fluid domain

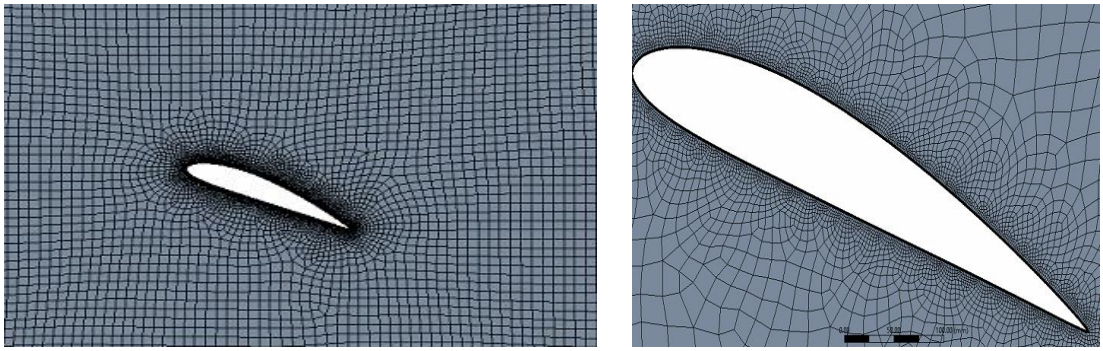

(b) Mesh close to the airfoil (c) Mesh at the airfoil

Figure 10 Mesh

3.3.1.3 Numerical Setup for fluent

Due to subsonic flying settings, the fluid flow is considered incompressible airflow, and its property is evaluated at given operating parameters. The inlet and outlet boundary conditions are 35 m/s velocity inlet and pressure outlet. The operating height is 2000 m above sea level (Liu et al., 2019). For the accuracy of the solution, a pressure-based steady-state solver and pressure velocity coupling with the COUPLE scheme was applied, while the 2nd order approach was used. The Turbulence model K-ω applied effectively captures low behavior in the viscous sub-layer region of the Wing surface (Hasan et al., 2019). Solver setup summarized input parameters are shown below: -

- ✓ Fluid property: - Air density (ρ = 1.225 kg/m3) and kinematic viscosity (μ = 1.7894e-05 kg s/m2)
- ✓ Operating Conditions: - Pressure = 101325pa and Temperature = 288.1K
- ✓ Boundary Conditions: - Velocity Inlet (35 m/s), Pressure Outlet.
- ✓ Solver: - Pressure based solver
- ✓ Turbulence Model: - K-ω
- ✓ Solution Controls: - Pressure Velocity Coupling – COUPLE
- ✓ Momentum: - Second-Order Upwind Scheme
- ✓ Hybrid Initialization: - Inlet Values
- ✓ Force Monitors: - Lift coefficients and Drag coefficients
- ✓ Reference Values: - Inlet Values
- ✓ Convergence Limit: - 1e-06

3.3.2 Verification of ANSYS Fluent result

The result in the ANSYS fluent can be verified by using the mesh metrics value Y + value and mesh independence test.

3.3.2.1 Mesh metrics

To have a correct simulation result, the mesh quality in the fluent should be within acceptable limits. Therefore, skewness and orthogonal quality are the major criteria used to assess mesh quality. The highest value of skewness should be less than 0.95 to satisfy the fluent solver, while the average orthogonal quality should be greater than 0.5 to provide an acceptable result (Canonsburg, 2017). The highest skewness value in this analysis is 0.86, which is sufficient for the solver.

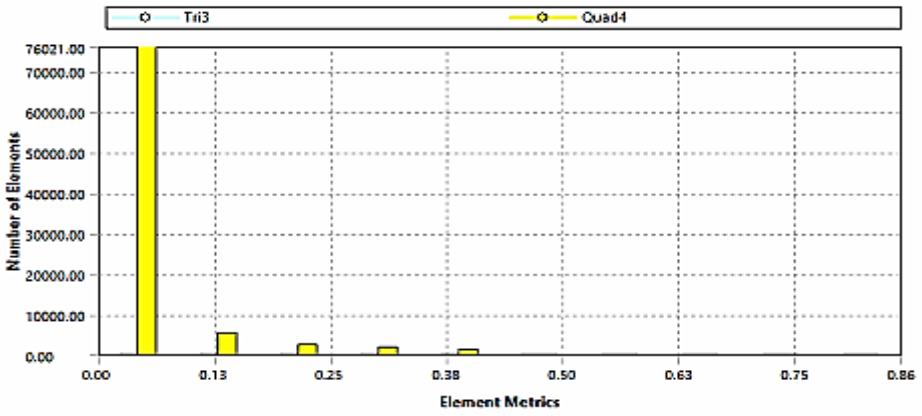

(a) skewness quality

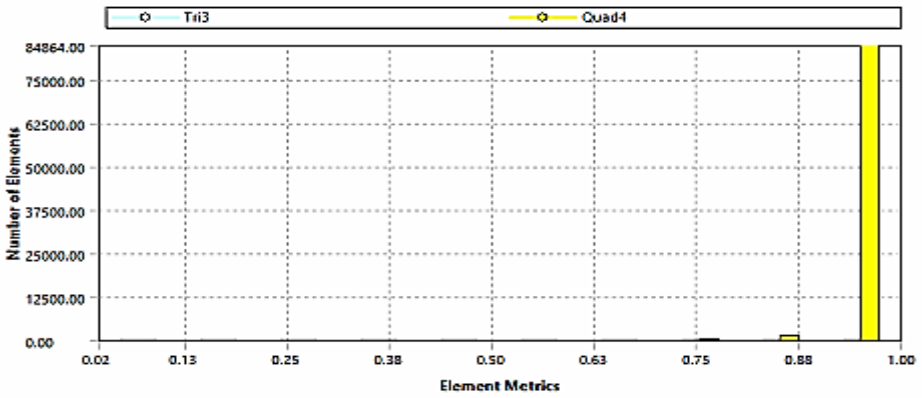

(b) orthogonal quality

Figure 11 Mesh metrics

3.3.2.2 CFD Mesh independence study

Five different element numbers were investigated to ensure that the fluent simulation results remained constant as the domain's elements were increased. Different mesh sizes and inflation are utilized to increase the mesh in the rectangular domain and make it finer near the Wing surface. The lift coefficient Vs. the number of elements and the drag coefficient Vs. Several elements are shown in Figure 16 below, with the fifth mesh element selected for further simulation.

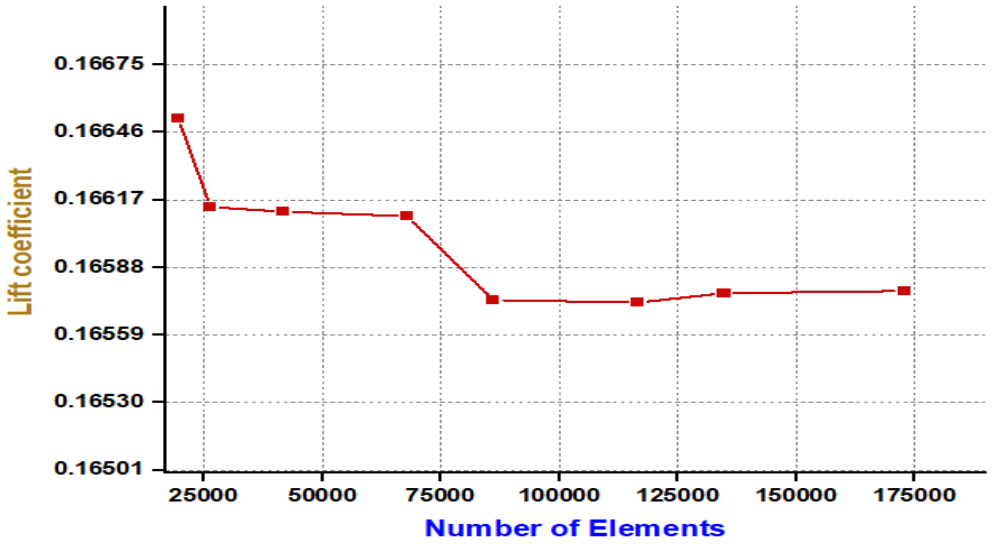

a) Lift coefficient Vs. Number of elements

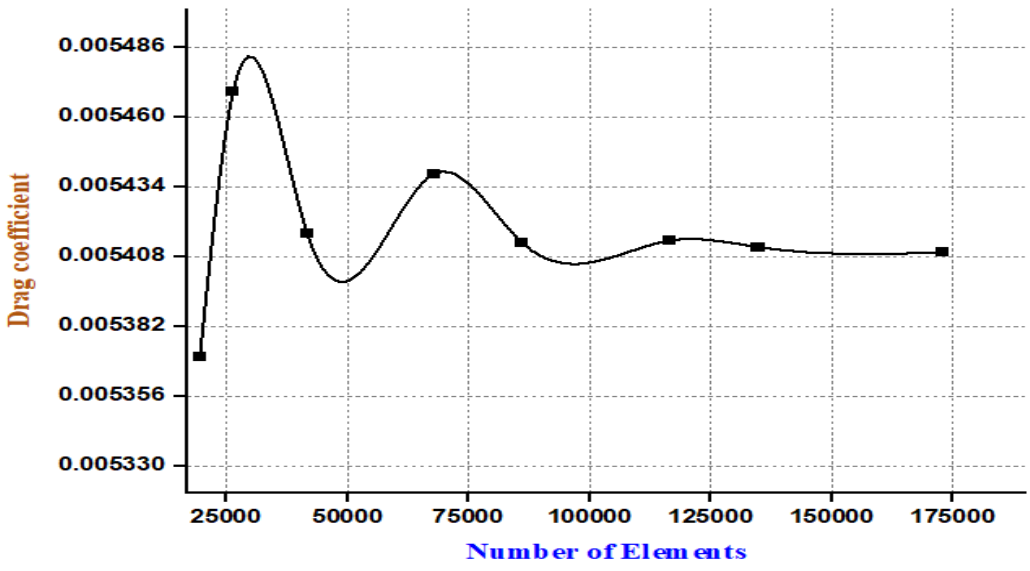

b) Drag coefficient Vs. Number of elements

Figure 12 Mesh independence study

3.3.2.3 Coefficients Vs. Number of iteration curve

The figure below shows the convergence of the lift coefficient and drag coefficient based on 259 iterations. It shows the graph is constant after some iteration which indicates the value is unchanged. The maximum lift and drag coefficient are 4.97E-01 and 8.63E-03, respectively, based on CFD Simulation.

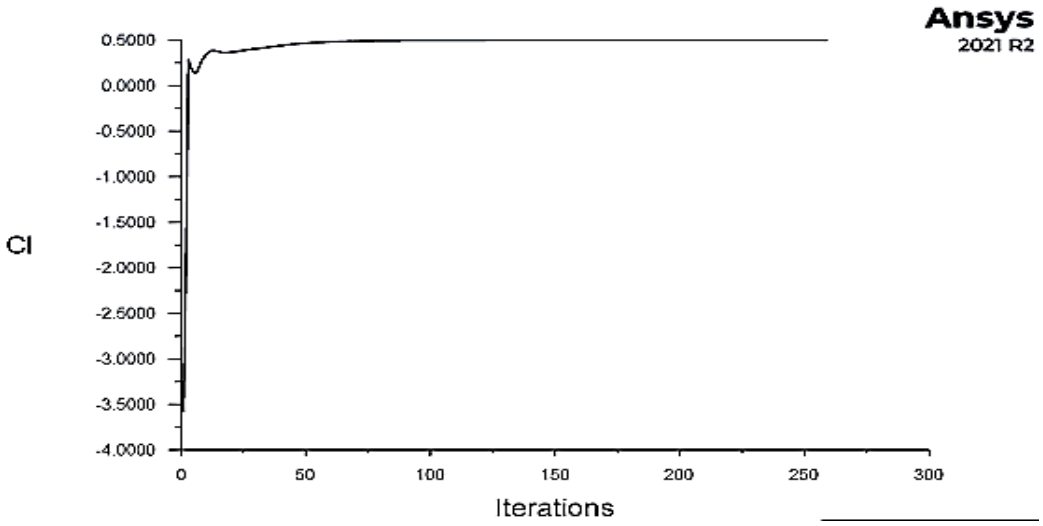

a) Lift coefficient Vs. Number of iterations

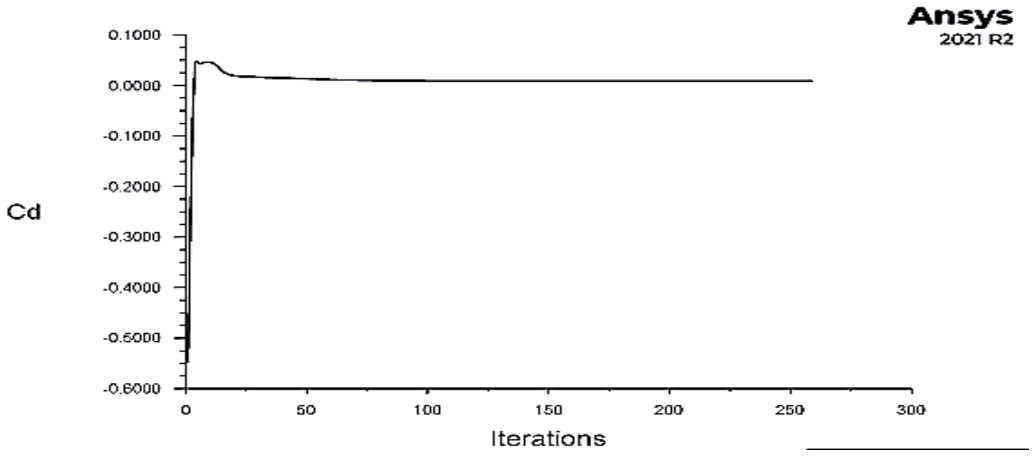

b) Drag coefficient Vs. Number of iterations

Figure 13 Coefficients Vs. Number of iteration curve

3.3.2.4 Y+ Value

The y+ number indicates the simulation result's accuracy, depending on the turbulence model utilized. For example, the color contour below shows that the y+ value in the Wing surface is within permissible limits, with a value of less than one.

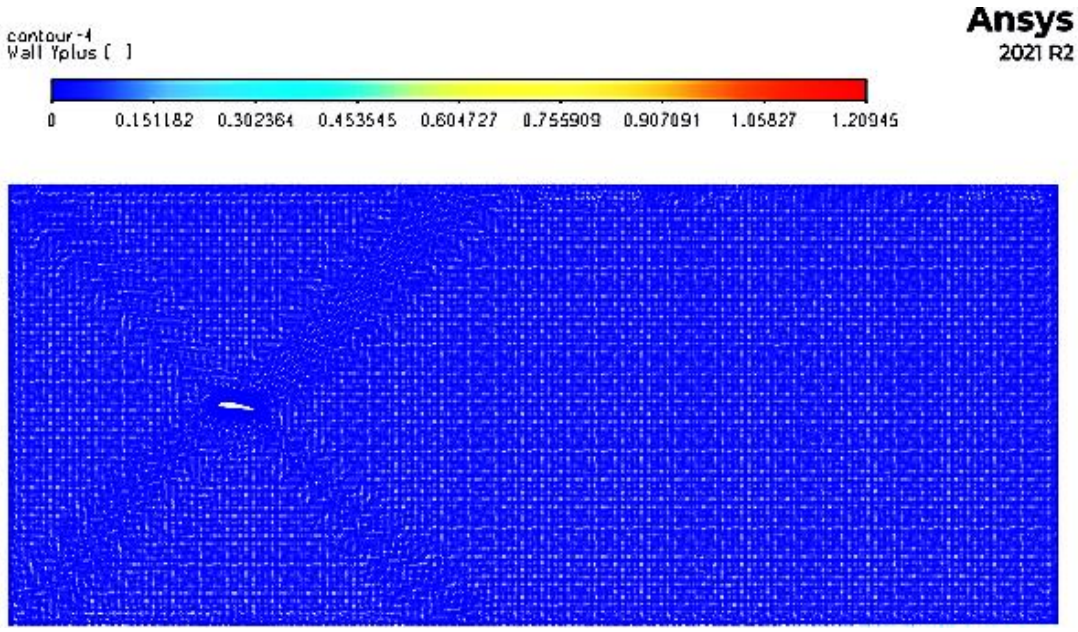

Figure 14 Y+ value

3.3.3 Design angle of attack

Under the given operating condition, the design angle of attack for the NACA 4415 airfoil Wing can be determined using the lift/ drag ratio Vs... AOA curve. The highest value in the curve indicates the required AOA for the desirable operation (Dwivedi, 2007). The following graph shows the lift Coefficient Vs. AOA, drag coefficient Vs... AOA and the ratio of Lift and drag Vs. the angle of attack.

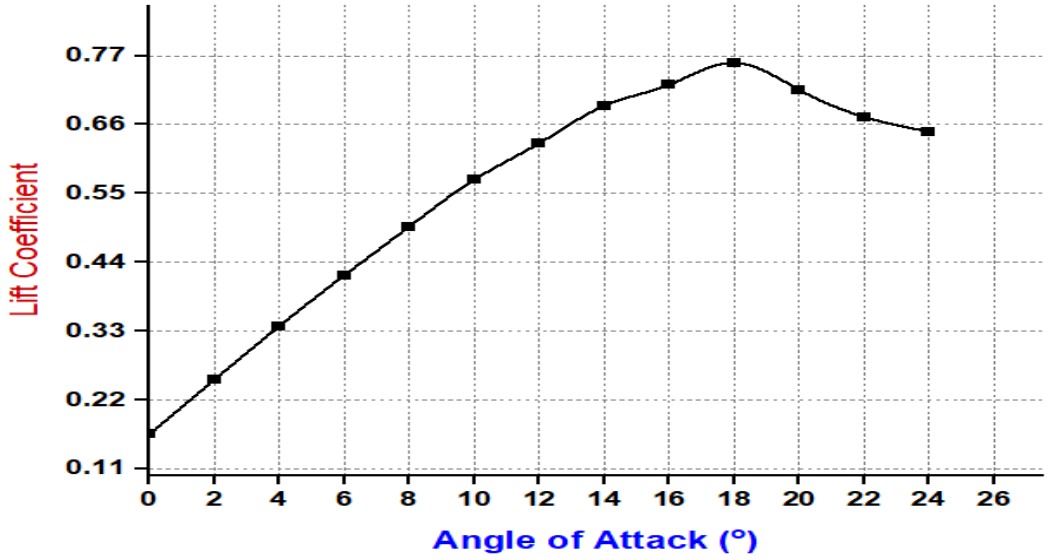

a) lift coefficient Vs. angle of attack

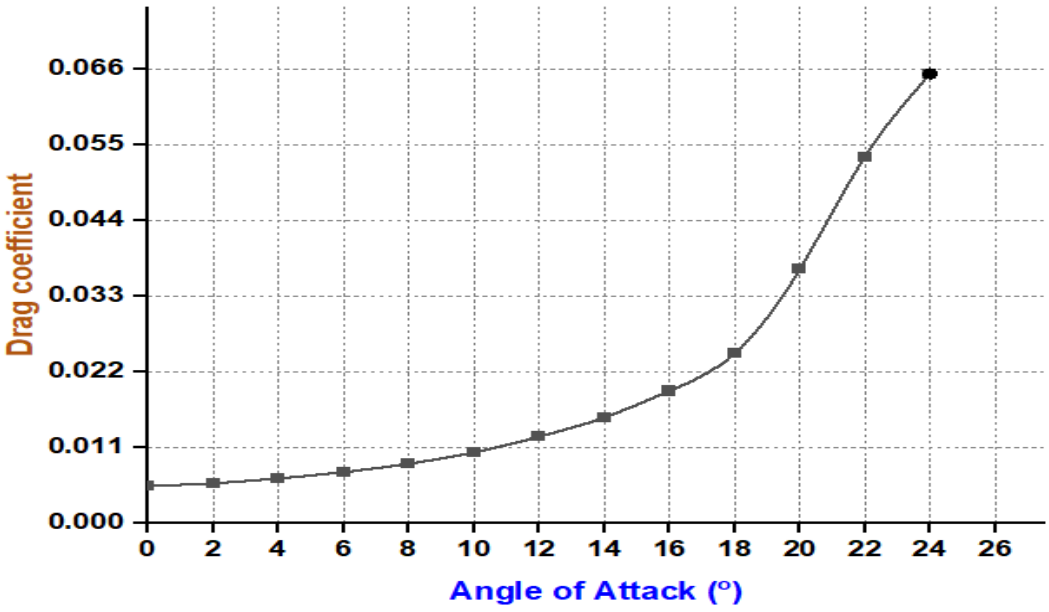

b) Drag coefficient Vs. angle of attack

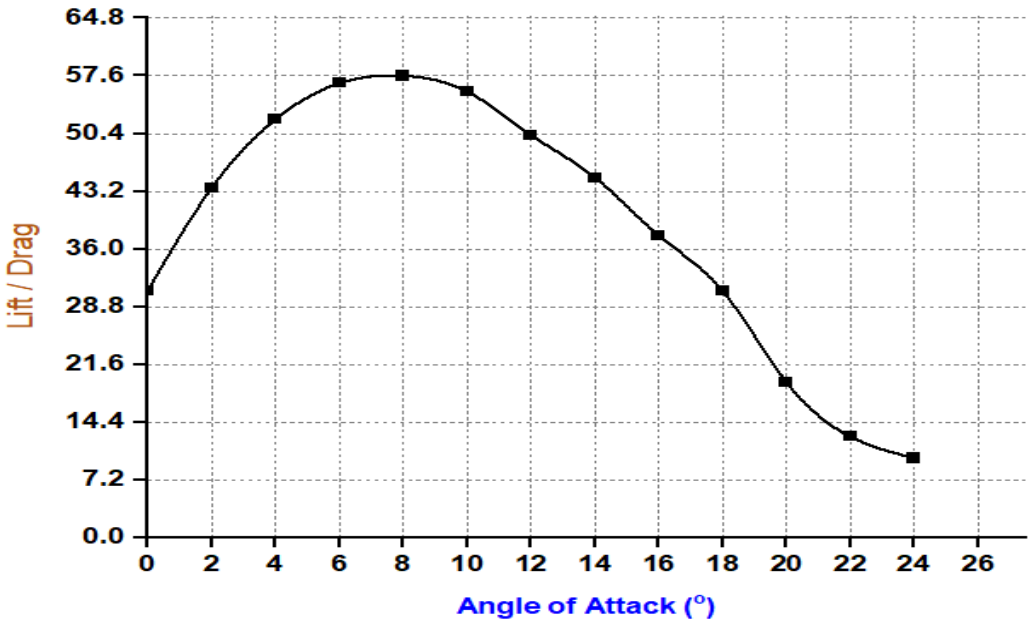

c) Lift/drag Vs. angle of attack

Figure 15 Coefficients Vs. Angle of attack

From the above graph, we can easily determine the design angle of attack as 8° and the pressure distribution around the airfoil below.

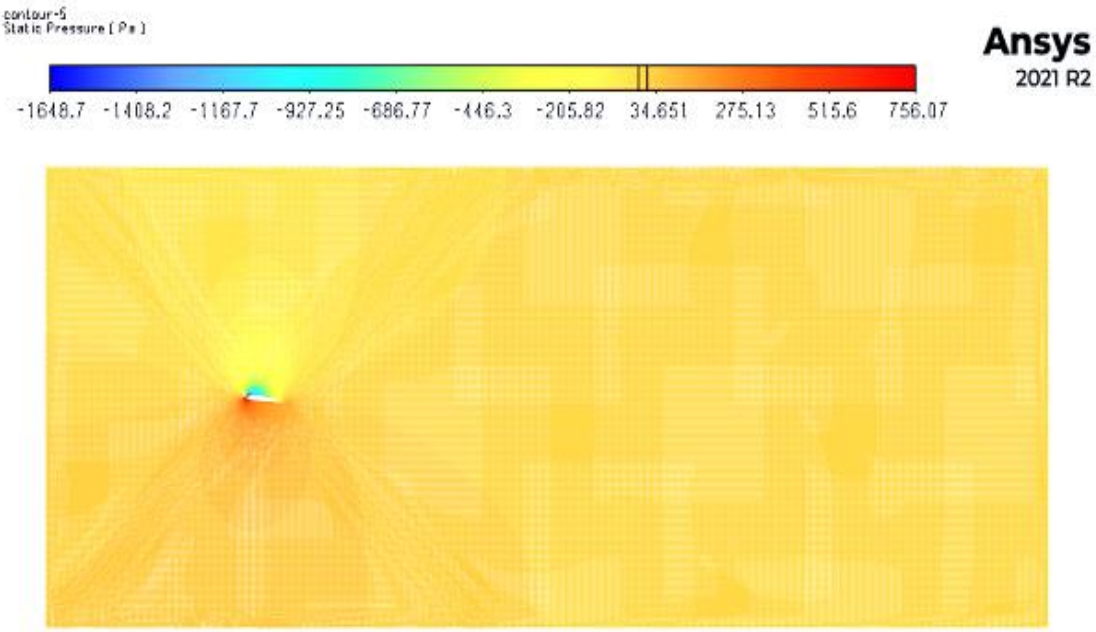

Figure 16 Aerodynamic pressure distribution around 2D airfoil

3.3.4 Aerodynamic load on the 3D wing

The solver process in the 2D airfoil is the same as in the 3D wing, while the fluid domain will have a three-dimensional enclosure to determine pressure distribution on

the Wing surface. After the design angle of attack is determined in the 2D airfoil, the final required pressure load obis trained from the 3D wing. Different mesh number numbers were used to study the mesh independence of the result.

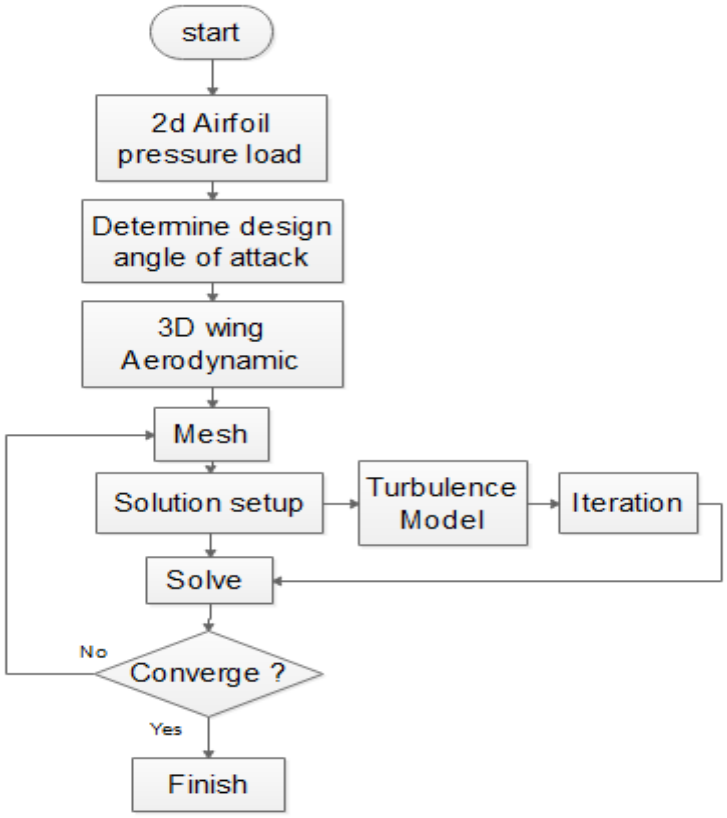

Figure 17 3D wing pressure load calculation on Fluent

The fluid domain on the 3D wing has input, output, symmetry, and boundary surface. The mesh in the fluent shown below has tetrahedron mesh elements with the maximum skewness value of 0.93 and 6178192 number of elements used for the final simulation. Therefore, the mesh independence study on the 3D fluid domain was conducted to get the most approximate result, while seven different mesh elements were used for the solution.

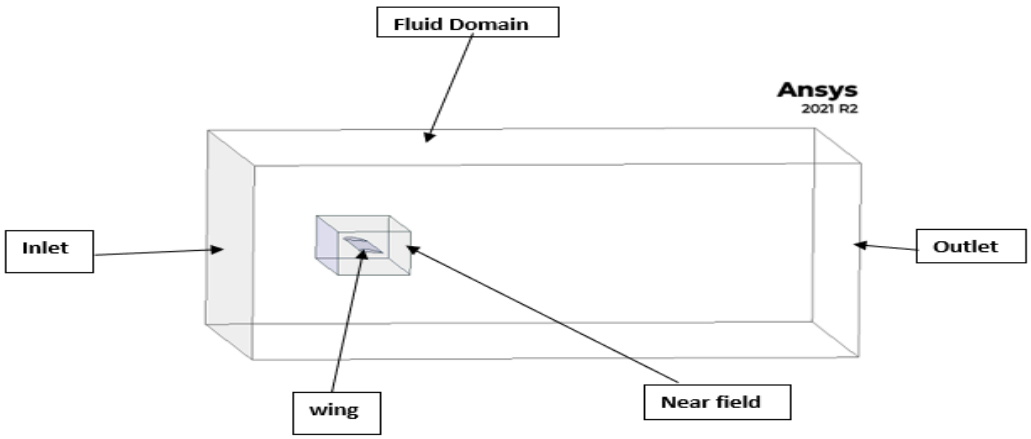

a) Fluid domain

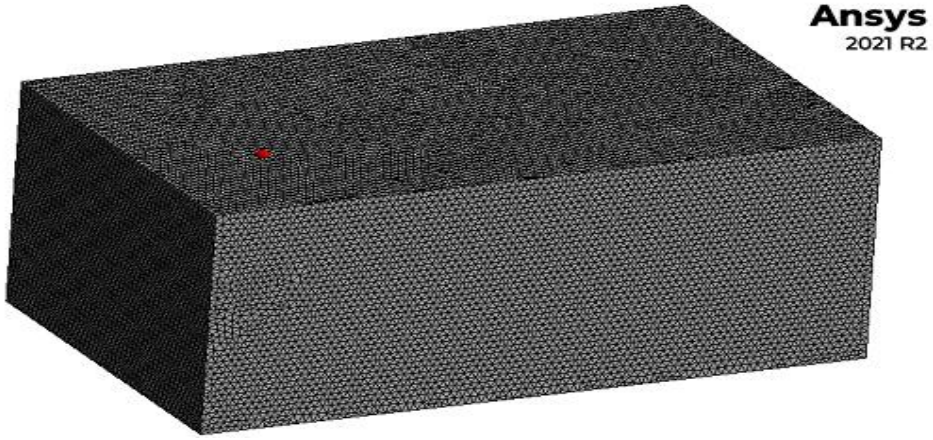

b) Mesh

Figure 18 3D Wing on fluent

The CFD simulation determined the aerodynamic pressure load distribution. The minimum and maximum pressure distributions on the wing's surface are -1420.01 Pa and 758.32 Pa, respectively. The pressure distribution is shown on the top and lower surfaces of the wing. Due to the angle of attack of the flight, the maximum pressure appears on the lower surface.

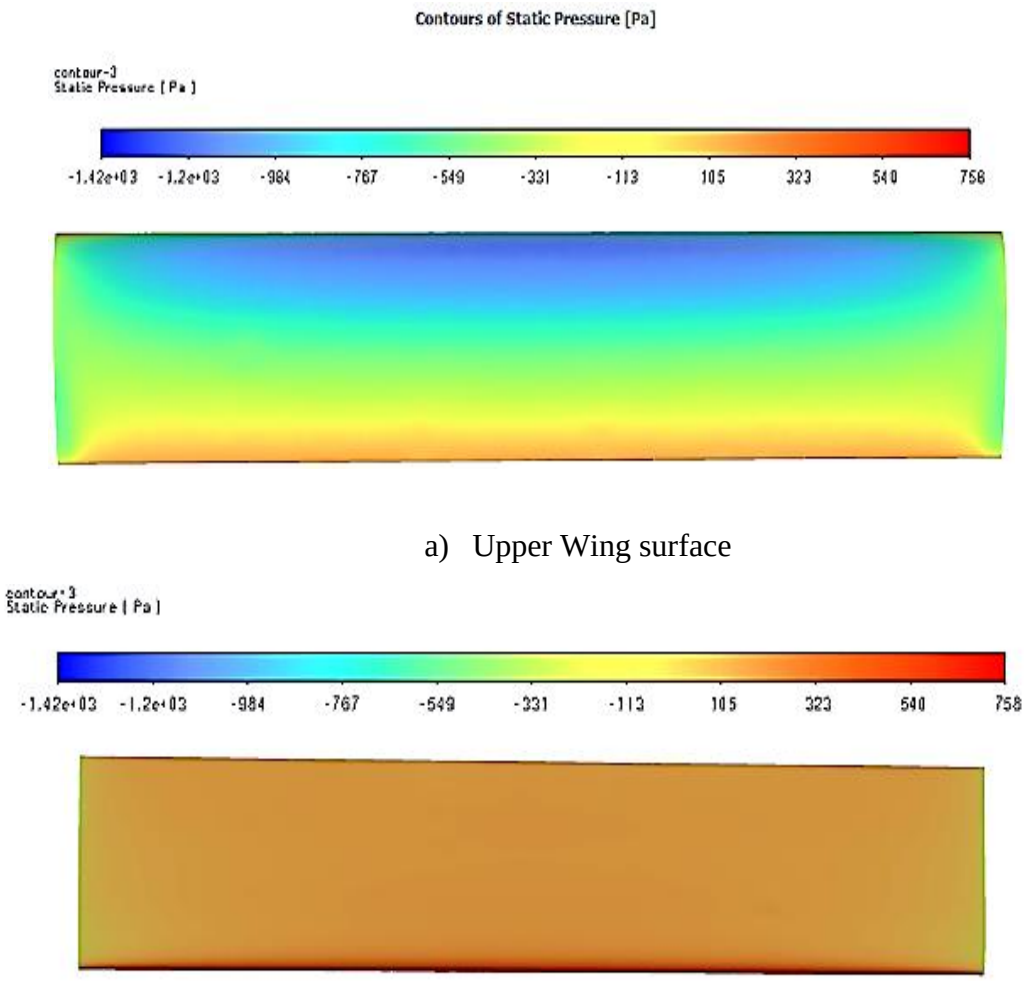

a) Upper Wing surface

b) Lower Wing surface

Figure 19 Aerodynamic load distribution on the wing

The pressure distribution on the Wing surface is symmetrical at the center of the Wing surface due to the high flow separation on the edge of the chord and the leading and trailing edge of the Wing (Dadkhah et al., 2019).

3.4 Finite Element Analysis

The ANSYS Workbench 21 R2 has been used to perform a finite element analysis of a composite UAV Wing, which included both static structural and modal analysis to evaluate the composite wing's deformation, stress, and natural frequency. Static structural analysis is used to identify the composite wing's deformation and stress; on the other hand, modal analysis is utilized to evaluate the composite wing's natural frequency and mode shape under the given aerodynamic load.

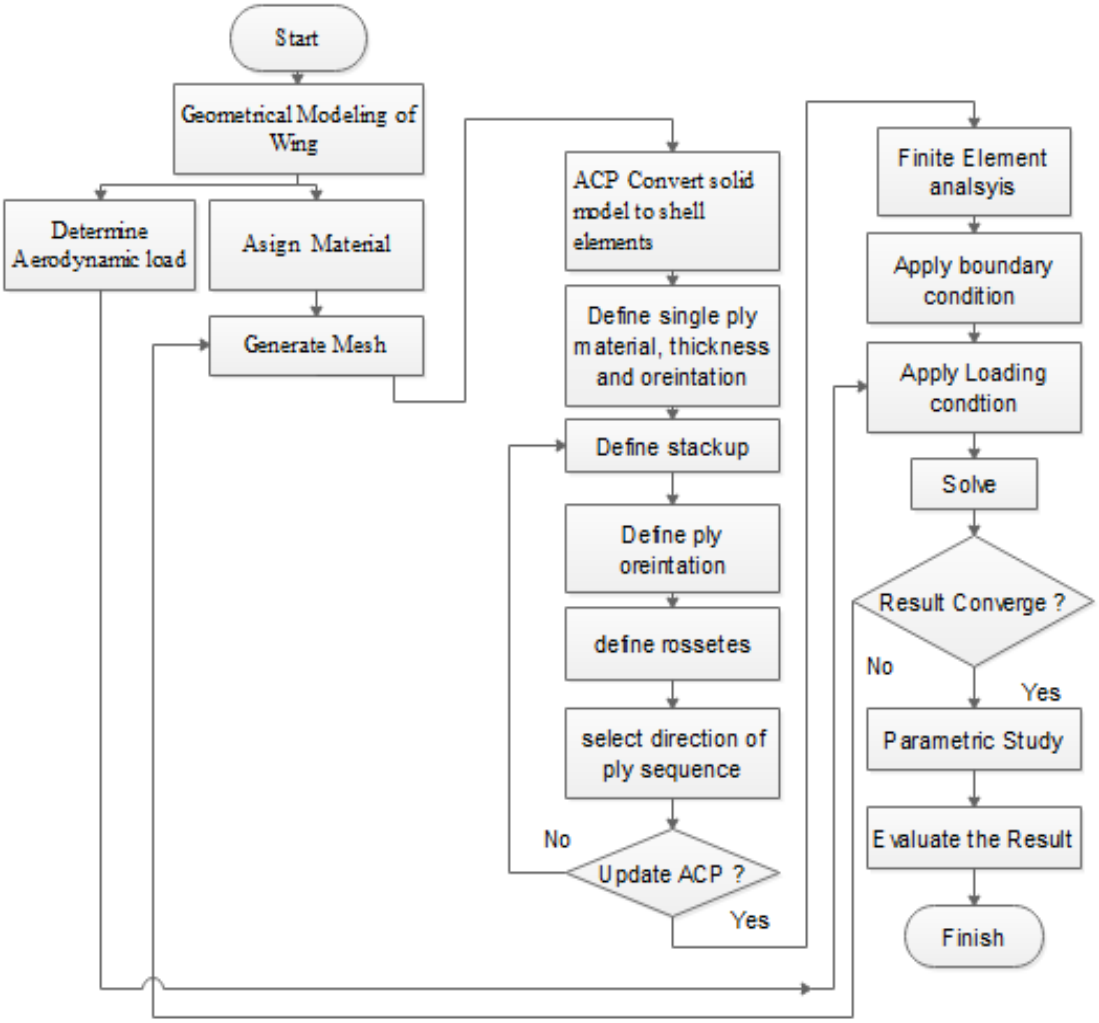

Figure 20 Finite element analysis Flow chart

3.4.1 Modeling composite layered wing

The Study used the Ansys Composite Pre-Post (ACP) module to model composite structures on ANSYS. In ACP, the solid model from Solid Works was converted into shell elements to perform finite element analysis on the composite Wing model. The thickness and ply orientation of the lamina define the type of composite material allocated to the model and the fabric in ACP, and several laminas stack together to form the composite laminate (Liang et al., 2021). Intervals of each lamina were established by the stress and strain behavior of composite laminate. Rosset's orientated selection set and modeling group should be determined suitably to construct the stack-up of the laminate material.

3.4.1.1 Assigning Material

The composite material assigned for the Wing model is Carbon Epoxy UD which has a high strength to weight ratio than other composite materials. Therefore, all parts of the wing will have the same composite material, while the elastic and strength property of the composite shown in Table 1 below.

Table 1 Elastic material property (Ramkuvar & Mankar, 2017)

Material	Density (kg/m^3)	Elastic modulus E11 (Gpa)	Elastic Modulus E22 (Gpa)	Poisson's ratio V12	Shear modulus G12(Gpa)	Ply Thickness (mm)
Carbon Epoxy UD	1490	121	8.6	0.27	4.7	0.2

3.4.1.2 Meshing composite wing

The solid model was converted into shell elements in ACP, and quadrilateral shell elements were chosen for better simulation results throughout this investigation.

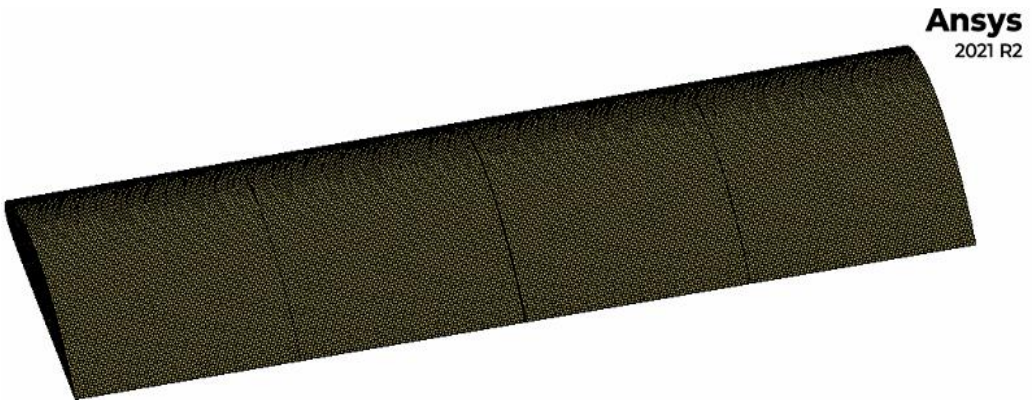

Figure 21 Mesh of the Wing

The mesh quality was assessed during the meshing process, and the mesh independence was investigated. Different mesh sizes are explored to get enough elements for the analysis. The final mesh has a quadrilateral element type and 6 mm element size, with 83013 elements and 84410 nodes. The Study reveals it has an accurate outcome with these elements.

3.4.1.3 ACP Setup for composite laminate wing

Each ply or lamina of the composite fabric has a different layout in the composite laminate wing. Therefore, each ply in the laminate stack up may have a different fabric thickness or ply angle, but the lamina can be specified with a common angle ply arrangement of (0,30,45,90.-45) to meet our model requirements. The direction of the stack up in the laminate is also determined in this module. Where all lamina is considered to be fully bonded together, and the stress and strain behavior in the laminate composite is investigated in the form of a single-ply.

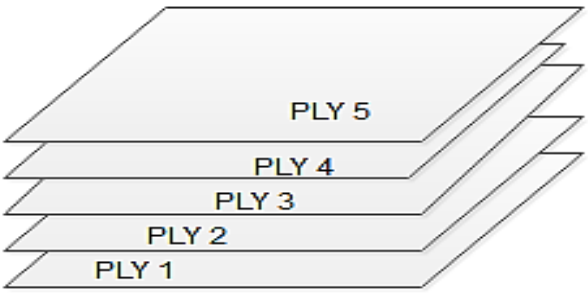

Figure 22 Stack up of ply for composite laminate

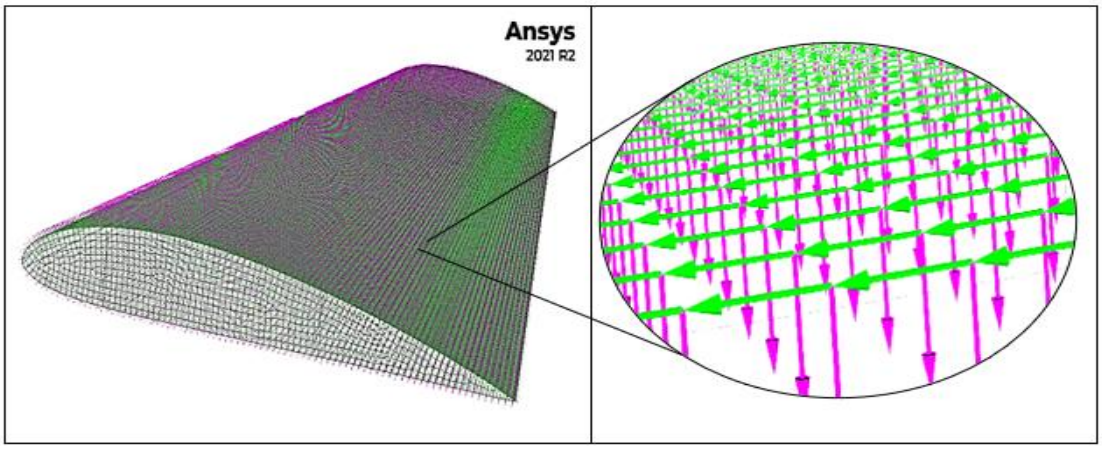

Figure 23 Composite Ply orientation and fiber direction

3.4.2 Boundary Condition

Due to the geometrical symmetry of the wing in the middle of the Wingspan, only one side of the wing is considered for analysis (Vijayanandh et al., 2018). The Wing part attached to the UAV fuselage is designated a cantilever beam since one end is fixed to the fuselage, and the other is free (Jacob Olaitan et al., 2017). The displacement and rotation at the fixed end are set to zero where UX=UY=UZ=ROTX=ROTY=ROTZ= 0 (Dwivedi, 2007). The figure below shows fixed-Wing support at the fuselage side.

Figure 24 Fixed support of the wing

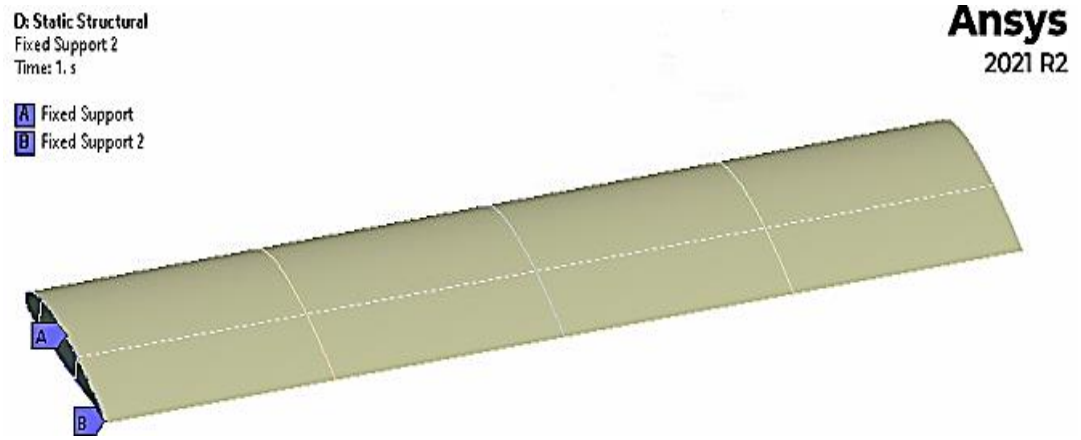

3.4.3 Loading Conditions

Aerodynamic pressure load and self-weight due to gravity are two types of loads acted on to the wing. The distributed pressure load on the top and lower surfaces of the wing was determined using Computational fluid dynamics on Fluent. As previously discussed, the maximum pressure load supplied to the bottom surface of the wing causes the UAV to generate lift force.

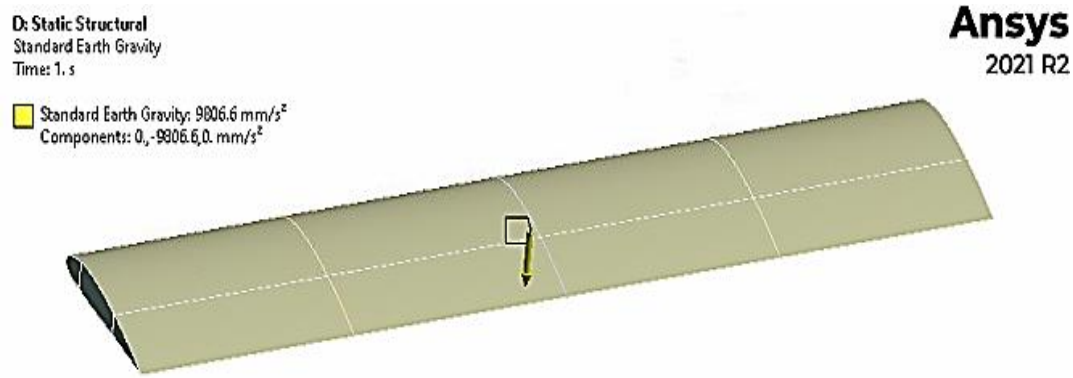

Figure 25 Gravitational load

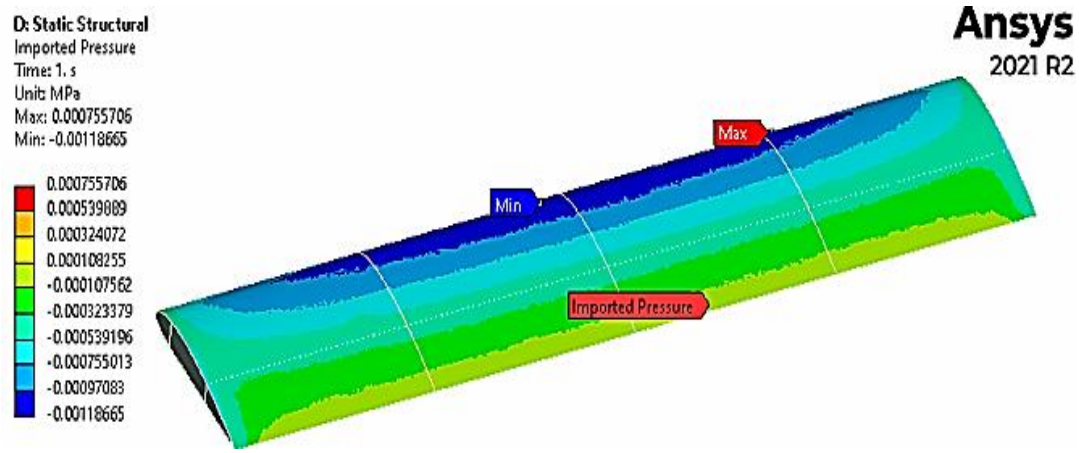

Figure 26 Aerodynamic Pressure load

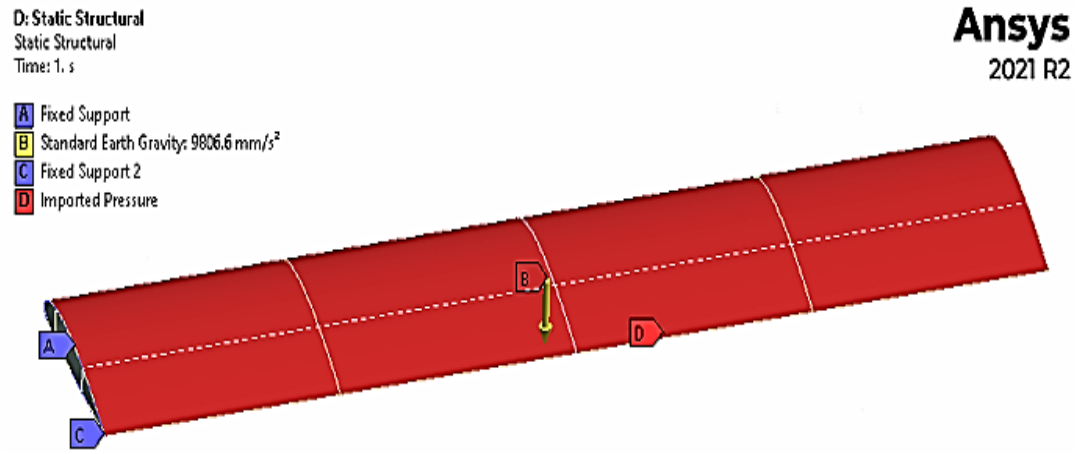

Figure 27 All boundary conditions on the wing

3.4.4 Parametric Study

This Study used two different parameters to assess the deformation, stress, and natural frequency of composite laminate UAV Wings. The first parametric Study is about the effect of spar location on composite using three different Wing models. The second parametric Study will be on the effect of ply orientation of composite laminate Wing skin on the static and modal behavior of the wing.

3.4.4.1 Parametric Study on the effect of spar location on the UAV Wing

The first parametric Study will investigate the effect of changing the spar location of the composite wing in the case of deformation, stress, and natural frequency. Three different models were used for the composite wing while the wing has the same skin thickness and symmetrical ply orientation of [0/0/0/0/0]. According to (Kanesan et al.,

2014), we can place the front spar location from 18 % to 25 % and the rear spar location from 62 % to 70 % of chord length. The composite wing with different Wing models is shown below in table (2).

Table 2 Spar location

Model	Front spar location (% chord)	Rear spar location (% chord)
1	18	62
2	22	65
3	25	65

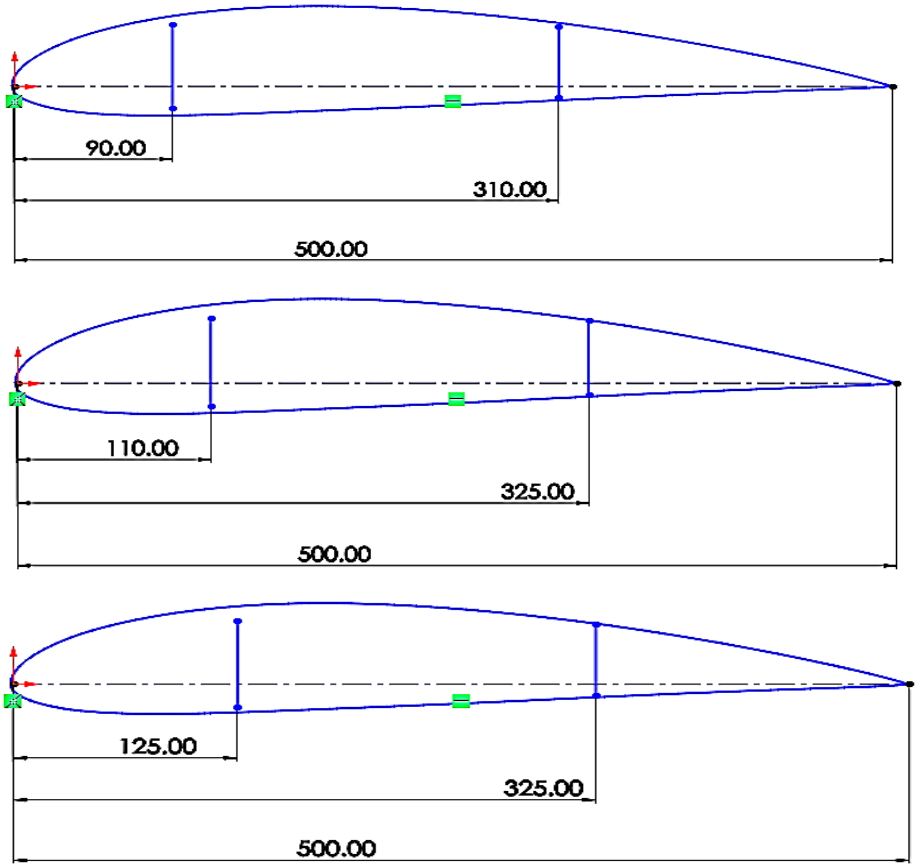

Figure 28 Chord wise spar location (All dimensions in mm)

3.4.4.2 Parametric Study on different ply angle orientation

The study will investigate the effect of variable ply orientation on a composite wing laminate with the same skin thickness and number of layers. For each model, the ply orientations of [0/30/0/30/0], [0/45/0/45/0], [-45/45/-45/45/-45], [0/60/0/60/0], and

[0/90/0/90/0] are defined, with a symmetrical stack up on the laminate wing. The ply orientation of various composite wing skin types is listed below in table (3).

Table 3 Composite Wing skin models with different ply orientations

Model	Orientation angle (^{o})	Skin thickness (mm)	Number of plies
1	[0/30/0/30/0]	1	5
2	[0/45/0/45/0]	1	5
3	[0/60/0/60/0]	1	5
4	[0/90/0/90/0]	1	5
5	[-45/45/-45/45/-45]	1	5

CHAPTER FOUR

4 RESULT AND DISCUSSION

This study conducted static structural and modal analysis on the Carbon Epoxy composite UAV Wing. The aerodynamic load calculated on the ANSYS fluent was used as a loading condition for the finite element analysis. This section will discuss different model results from two different parametric studies. All finite element analyses were verified using the first model mesh independence test, and the quality of the mesh was enough to determine the required parameters.

4.1 Mesh independence study

The study applied a different number of elements by increasing the number of elements 1.5 times from the previous element mesh to investigate the independence of a number of elements in the mesh (Alawadhi, 2010). This study used the first model to assess the remaining models with an adequate number of elements. The findings show that as the number of elements rises, the value of a result converges to the same value, as seen by the seven different mesh numbers. From the observed result, the sixth mesh number selected for further analysis is quadrilateral shell elements with 83,013 elements for the solution. As the element size decrease, the number of elements increases for the model.

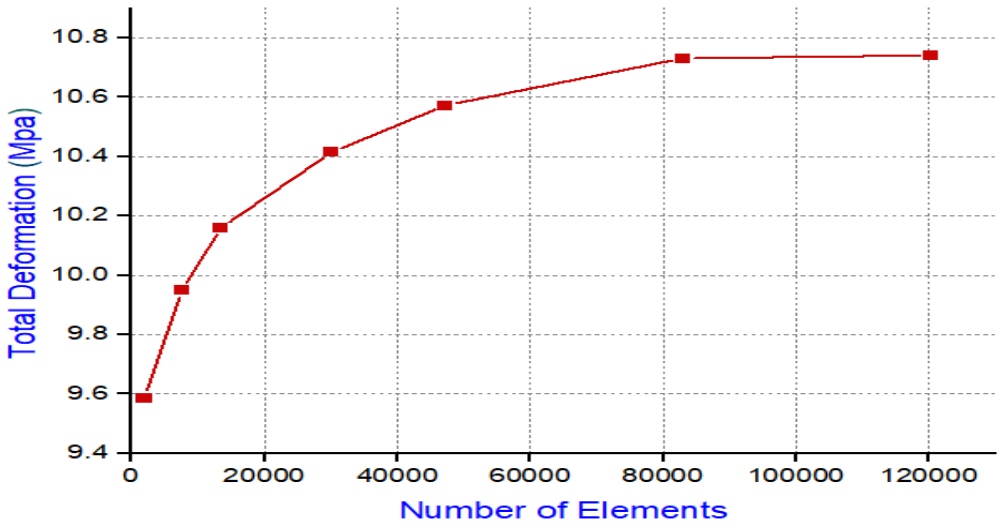

Figure 29 Total deformation Vs. number of elements

After the sixth mesh element, the result of deformation and natural frequency of the first model remains the same, indicating the mesh is enough for further simulation. The result will not depend on the element number.

4.2 Static Structural Analysis Result

The static structural analysis has an output parameter of total deformation, maximum shear, equivalent, and bending stress of different models on the wing. The result of the first parameters study (Varying spar location) and second parameter study (varying ply orientation on the skin) has discussed below.

4.2.1 Static Structural Result on the first parametric Study

The static structural analysis was conducted to get the total deformation, bending, equivalent and maximum shear stress on the three different models with varying spar locations. In all Wing models, the loading condition includes gravitational and aerodynamic loads. From observation, the maximum and minimum total deformation occur on the Wingtip and root, respectively. At the same time, the maximum and minimum shear stress occur on the wing root and tip, respectively. For example, in the first, the total deformation of the model is 63.895 mm, and the maximum shear stress value is 38.042 Mpa.

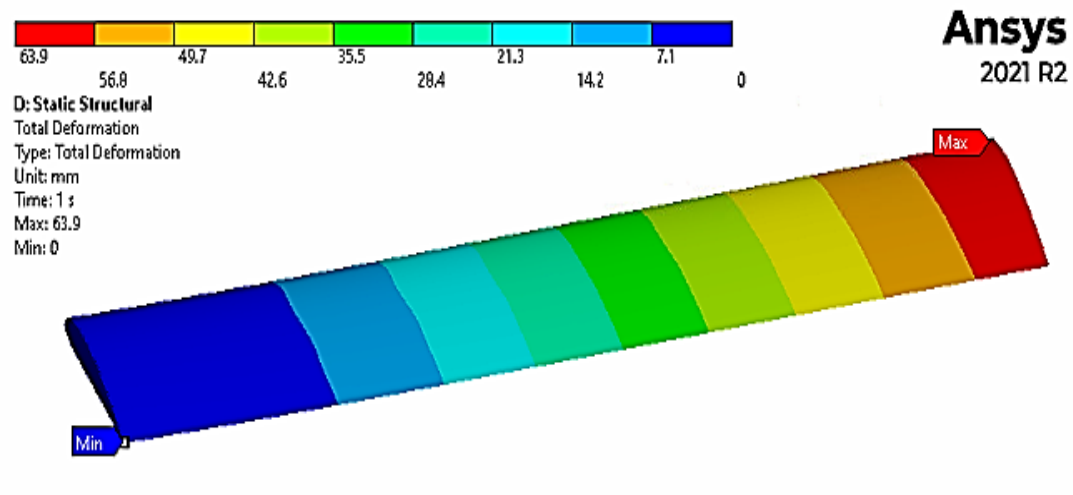

Figure 30 Total deformation of Model 1

The figure above shows the distribution of deformation from the root to the tip of the wing, and the color code shows blue indicates minimum areas and red color indicates the maximum deformation region.

The effect of Aerodynamic load has a significant influence on the deformation and shear stress of the wing. The figure below shows the response of the maximum shear stress Wing model due to aerodynamic loading conditions.

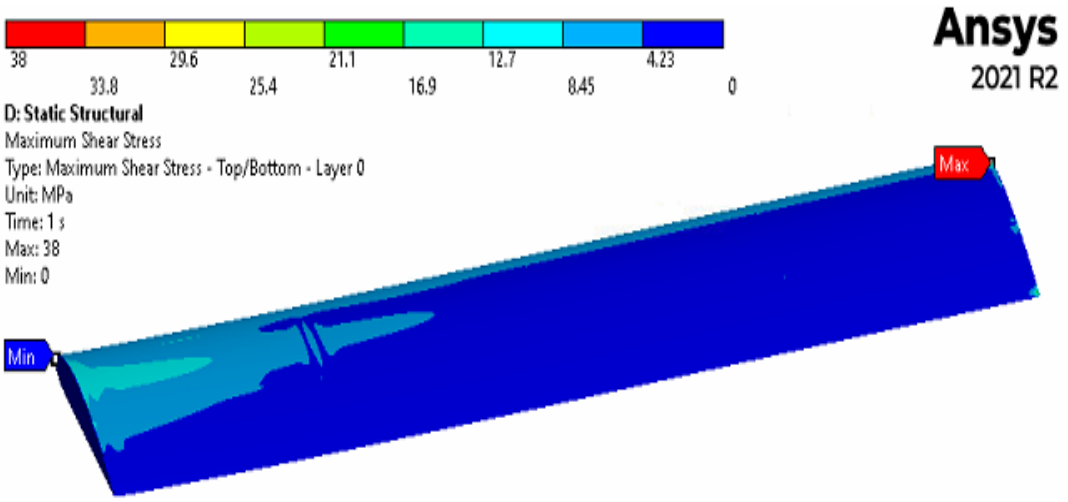

Figure 31 Maximum Shear Stress of Model 1

Previously stated, the main part of the Study is the effect of spar location for three models studied under both gravitational and aerodynamic loads. From the analysis result, the maximum deformation occurs in model 3, and the maximum shear stress occurs in model 2. On the other hand, Minimum deformation and shear stress were obtained in model 1. The difference between the highest and lowest deformation value for all three models is 34 %. The difference in shear stress for all three models is 43.4 %, indicating model 1 has better performance in the case of static structural analysis. From the analysis, the spar position when close to the leading edge will decrease the deformation and the maximum shear stress.

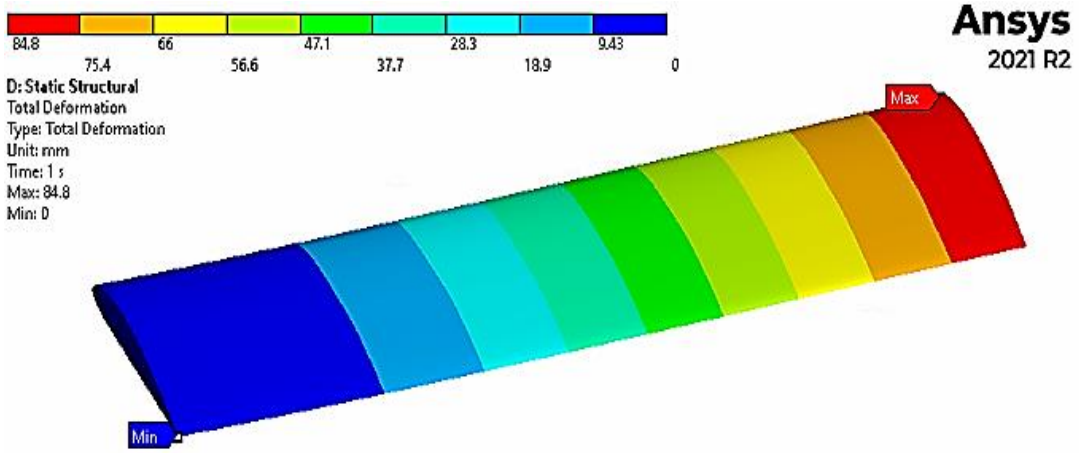

a) Model 2

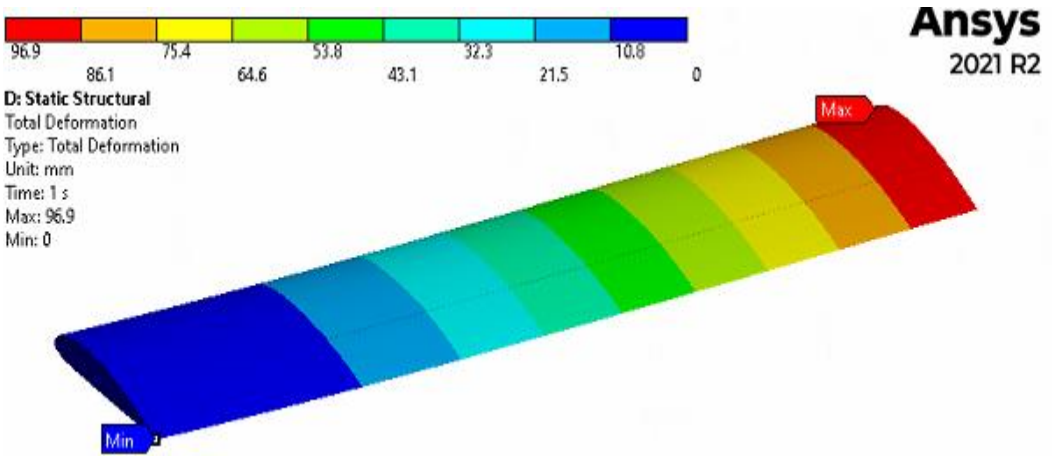

b) Model 3

Figure 32 Total deformation

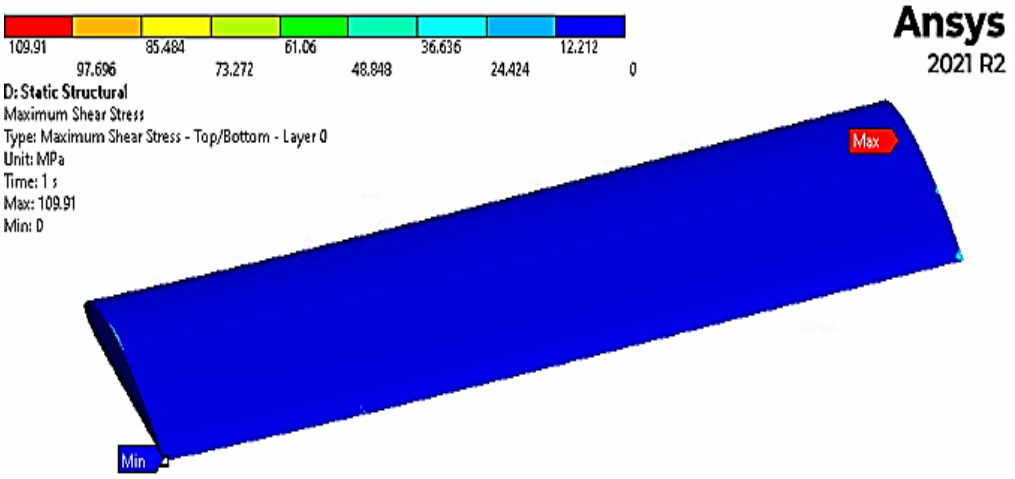

a) Model 2

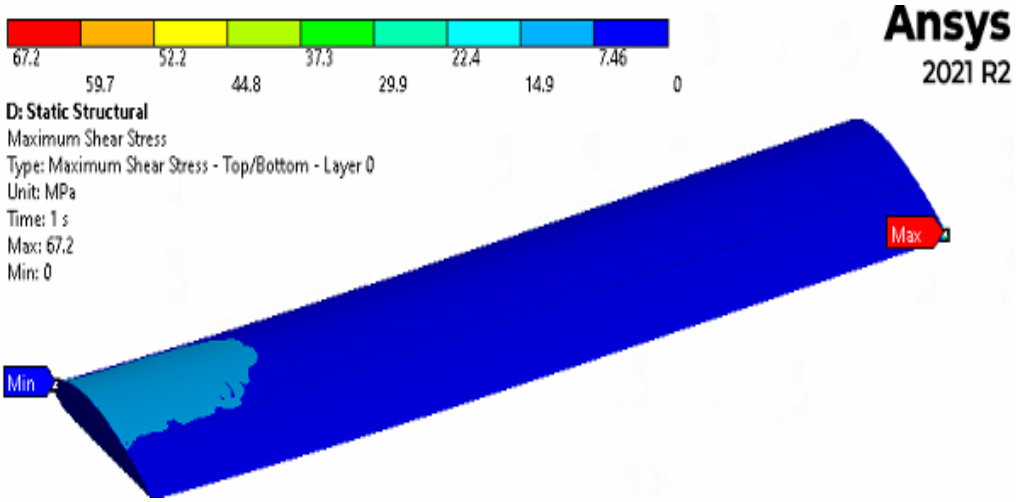

b) Model 3

Figure 33 Maximum shear stress

The comparison of the result of all models is shown below in figure (34), and according to the graph, there is a big difference in both deformations and shear stresses. From observation, model 1 has better structural performance than models 2 & 3, which indicates its more suitable for the Wing model.

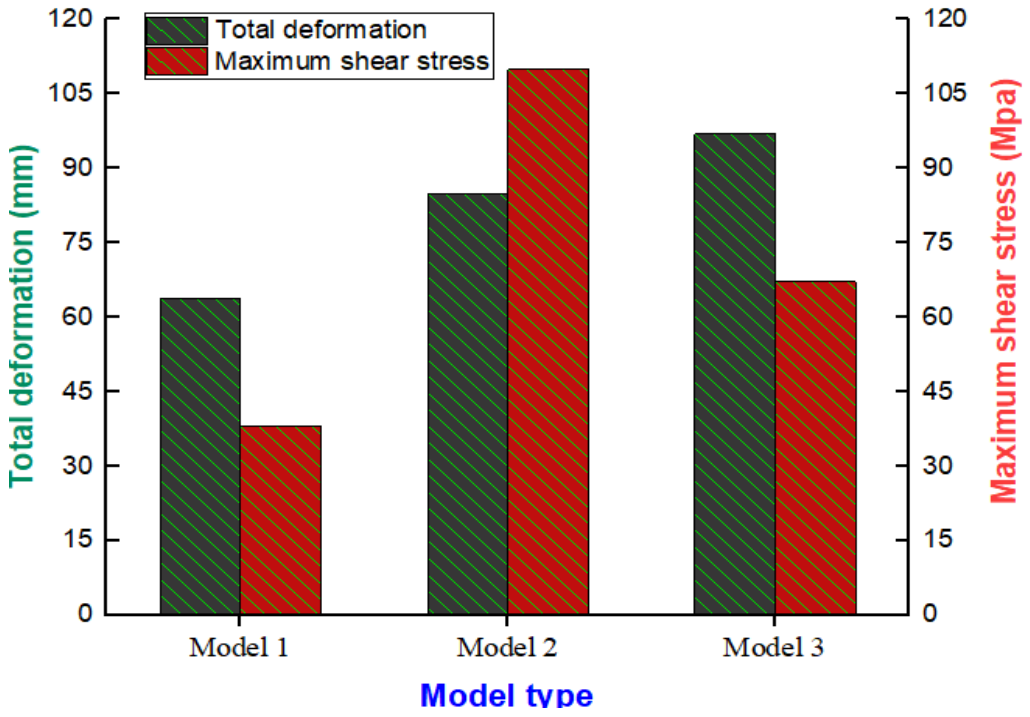

Figure 34 Comparison results of all three model

Another important output parameter is bending stress on the wing, which has a significant effect on the varying spar location of the wing. From the observed result of all models the bending stress in the X direction is higher than the Y direction where from the three models, the first model has less bending stress, whereas the second model has a high bending stress value which indicates model 1 has better structural performance than the other two. The corresponding X Bending stress value for model 1 and model 2 are 75.8 Mpa and 147.8 Mpa where Y bending stress value for model 1 and model 2 are 19.8 Mpa and 121.6 Mpa, respectively.

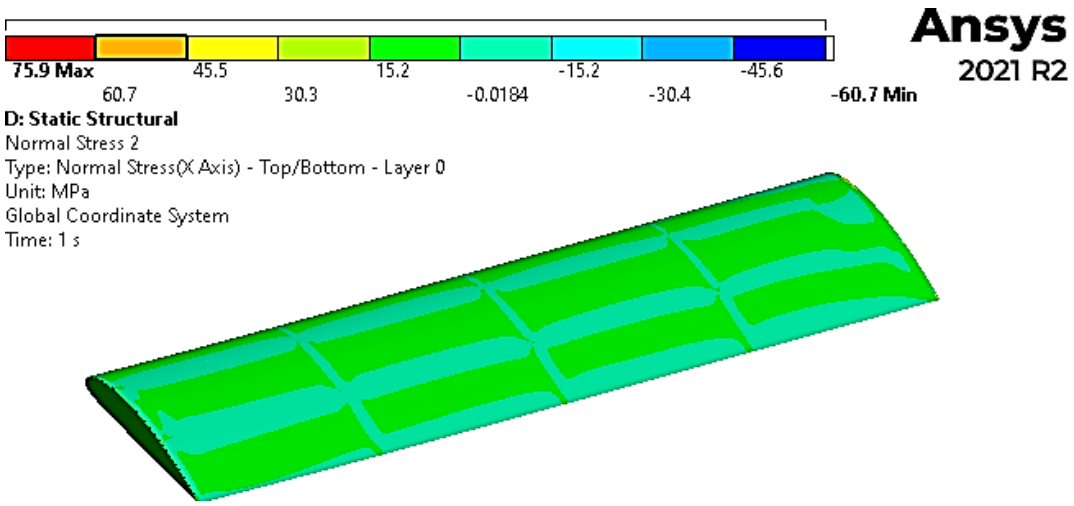

Model 1

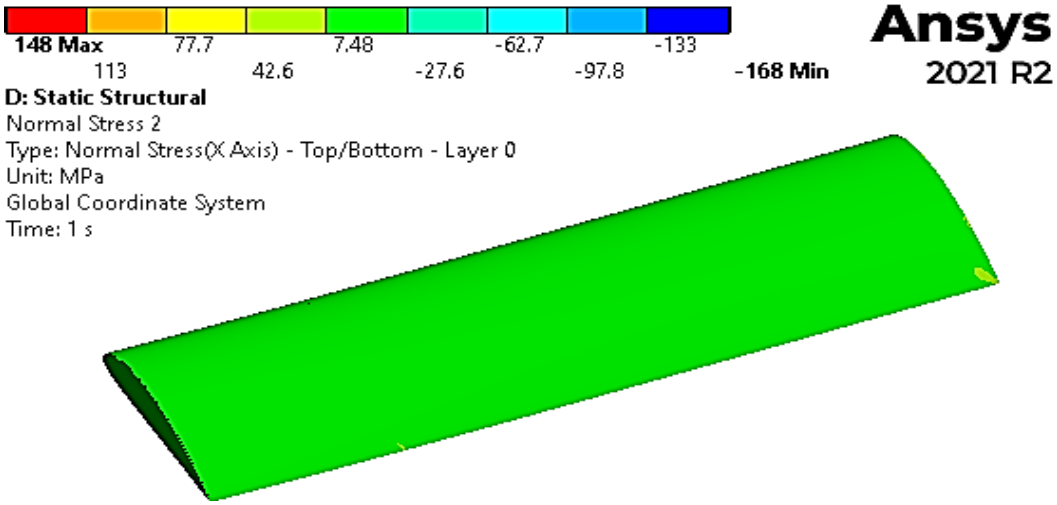

Model 2

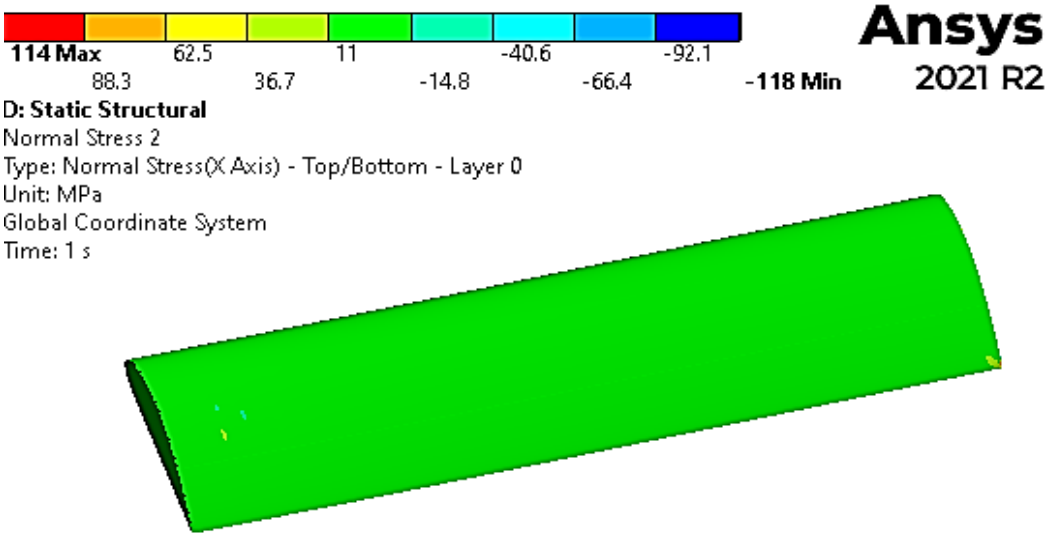

Model 3

Figure 35 Bending stress for X Direction

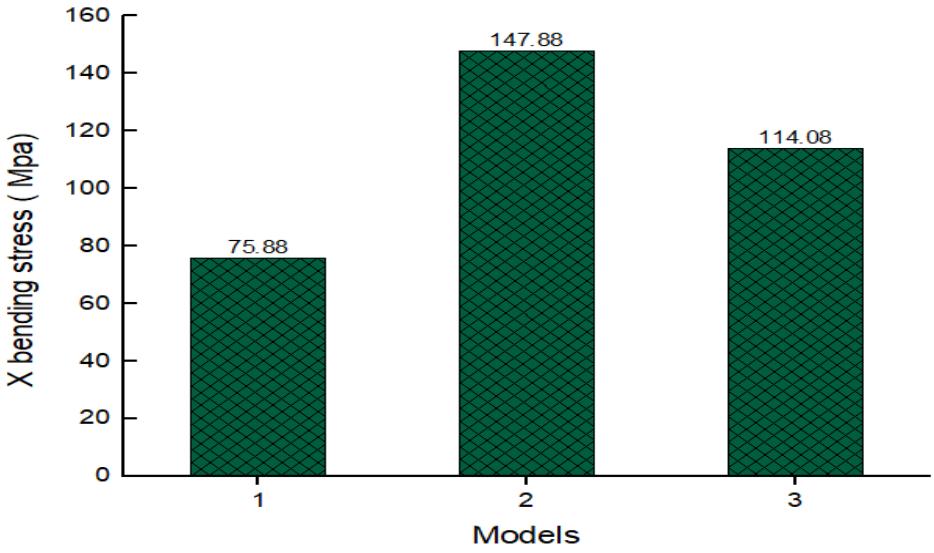

Figure 36 Comparison of bending stress results in the X direction

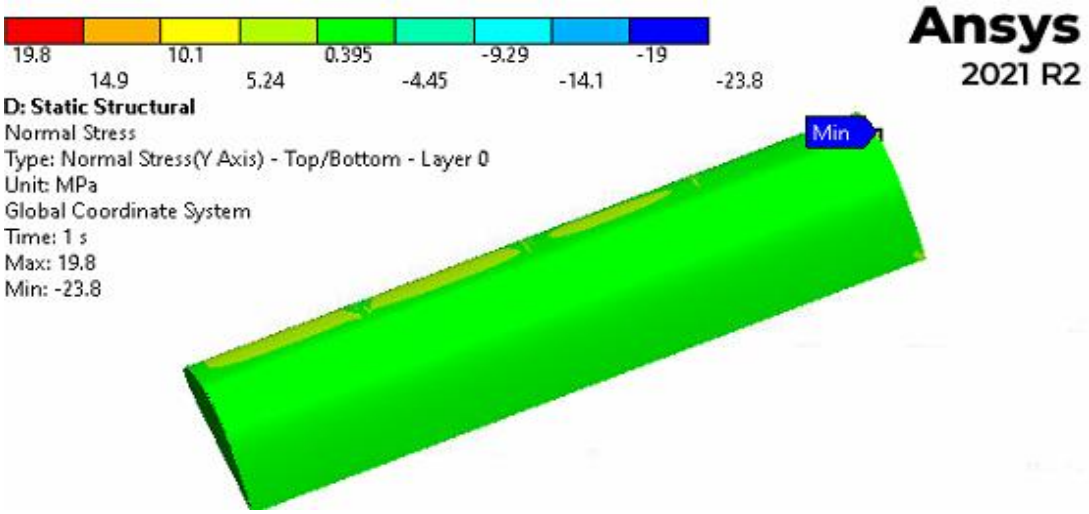

Model 1

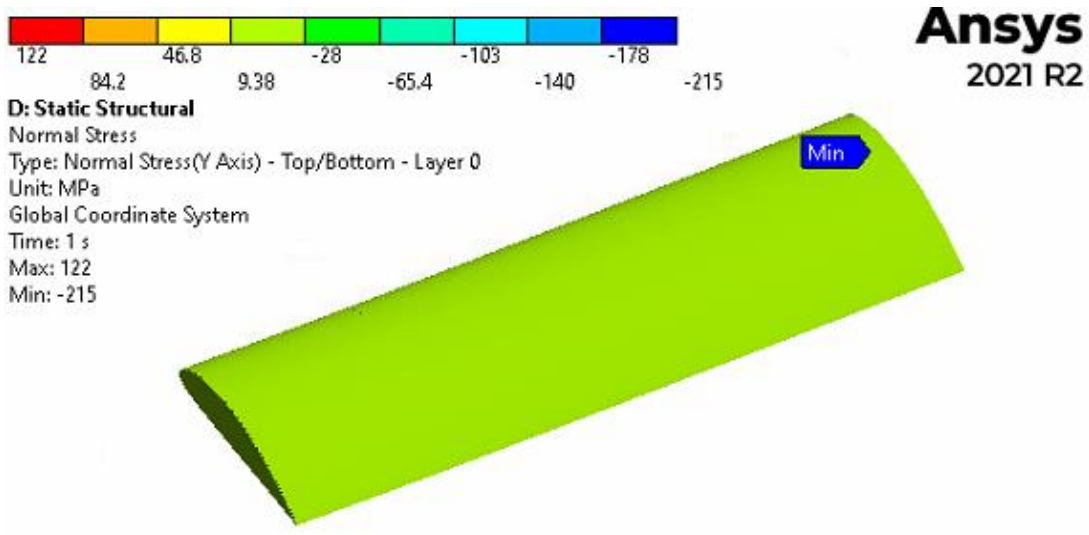

Model 2

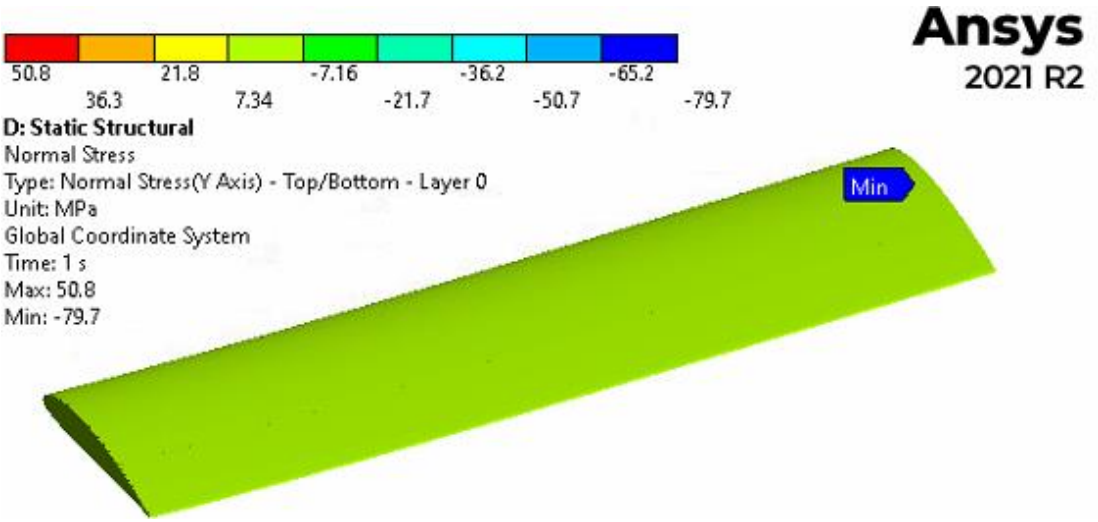

Model 3

Figure 37 Bending stress for Y Direction

The figure below compares all three models under the Y bending stress output parameter. According to the graph, the maximum and minimum values occur in model 1 and model 2, the same as the previous shear stress result.

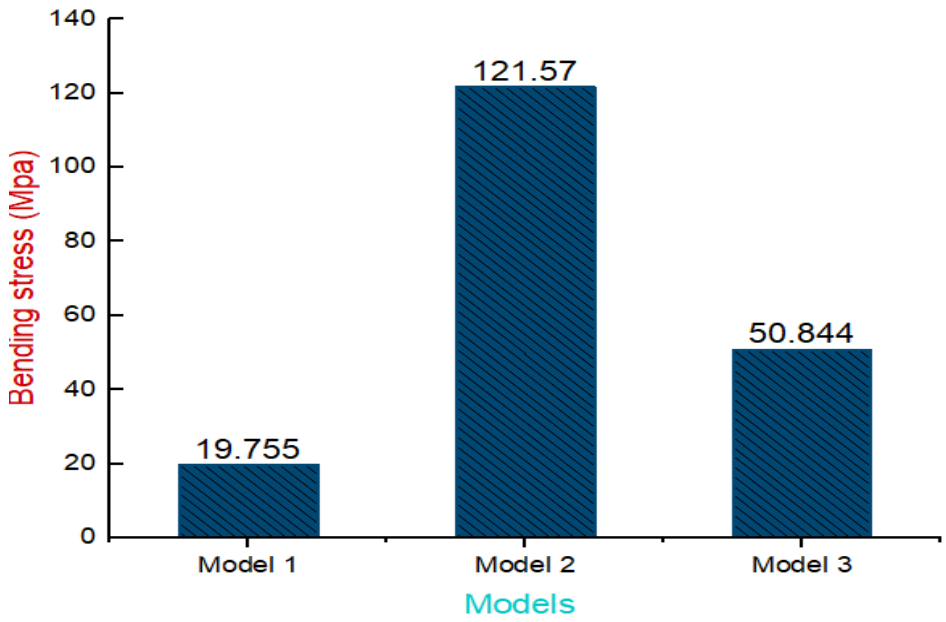

Figure 38 Comparison of bending stress results in the Y direction

In addition to shear and bending stress, the equivalent (von-mises) stress of all three models was evaluated, and the results are discussed. The maximum and minimum values of the equivalent stress were obtained at model 2 and model 1, respectively, with the corresponding values of 206.8 Mpa and 69.47 Mpa.

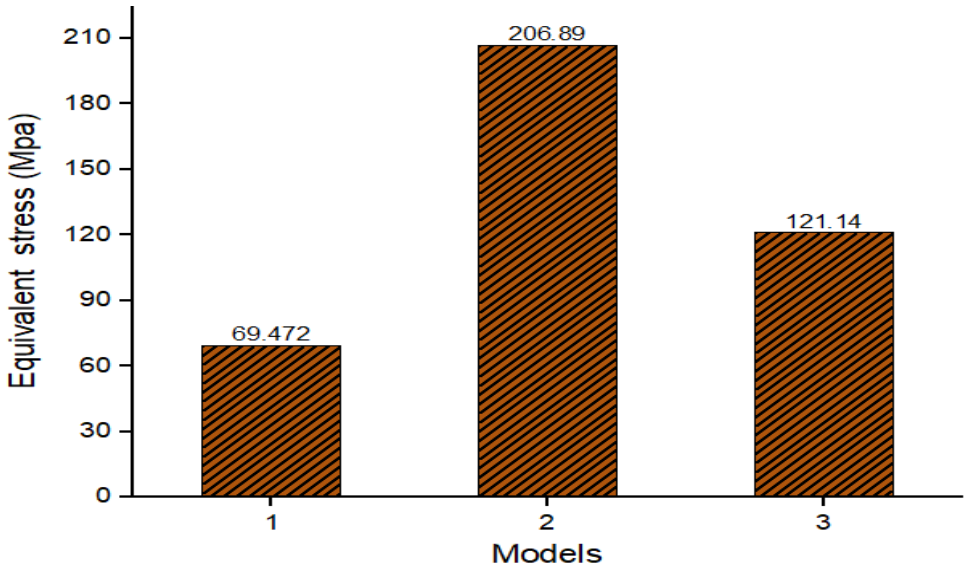

Figure 39 Comparison of equivalent stress for three models

4.2.2 Static Structural Result on the second parametric Study

This study evaluated the effect of the ply orientation of Wing skin on the total deformation, bending stress, and maximum shear stress using five different models. From the observation of varying the ply orientation on the wing, the skin has a significant change in the deformation, bending stress, and maximum shear stress of the wing. As discussed previously, deformation is maximum at the Wingtip and minimum at the wing root, while shear stress is maximum close to the Wing root and minimum around the tip of the wing. Maximum deformation occurs on the ply orientation of [0/30/0/30/0], and minimum occurs at [0/90/0/90/0]. On the other hand, shear stress is maximum on the [-45/45/-45/45/-45] and minimum at [0/90/0/90/0]. (Rajadurai et al., 2017) conduct static analysis with different ply orientations on the whole wing. Finally, its result shows that [0/90/+45/-45/90/0] has better structural performance. Another research paper (Mathai et al., 2014) also studies different orientations of Carbon fiber reinforced polymer (CFRP) composite Wings and concludes the arrangement [0/90/45] shows less deformation and von mises stress. The highest deformation value is 42.34 mm, and the lowest deformation value is 16.83 mm, while the highest shear stress is 45.43 Mpa and the lowest shear stress is 31.25 Mpa. The graph below shows the value of deformation and shear stress with the ply orientation of Wing skin.

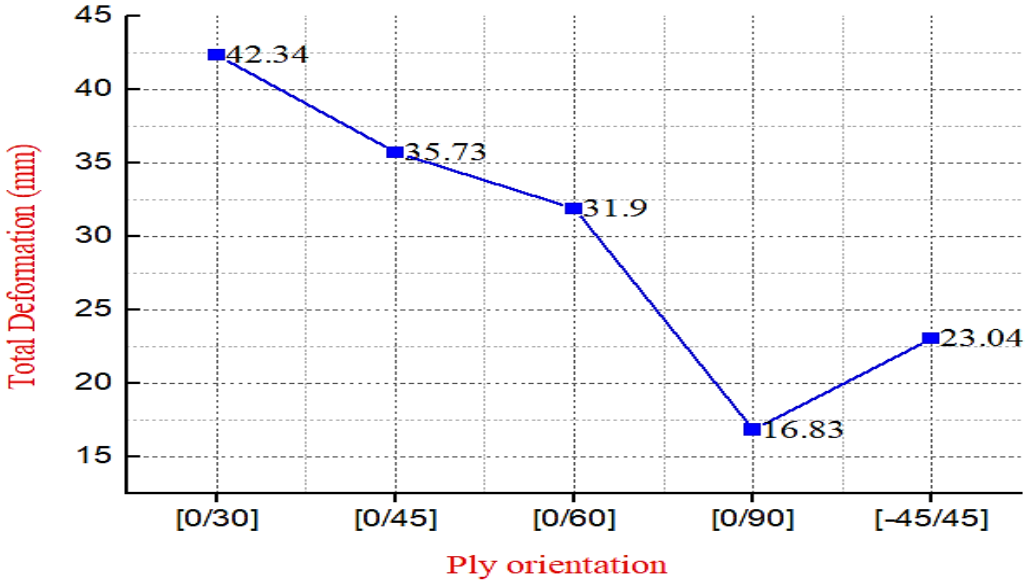

Figure 40 Deformation Vs. Ply orientation

The comparison of the deformation and shear stress for all cases of ply orientation shows there is a significant variation with 60.25 % in deformation and 31.21 % in maximum shear stress.

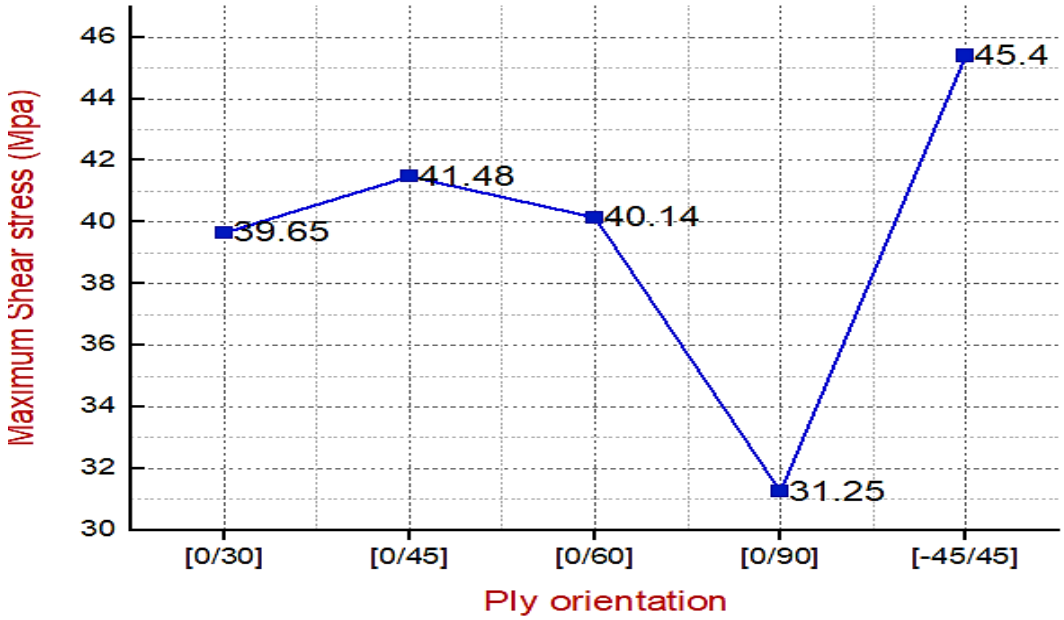

Figure 41 Maximum shear stress Vs. Ply orientation

Bending stress results in the various ply orientation of Wing skin has almost the same effect as shear stress. Minimum bending stress occurs at [0/90/0/90/0], and maximum bending stress occurs at [0/30/0/30/0], with corresponding values are 7.6 Mpa and 25.2 Mpa, respectively.

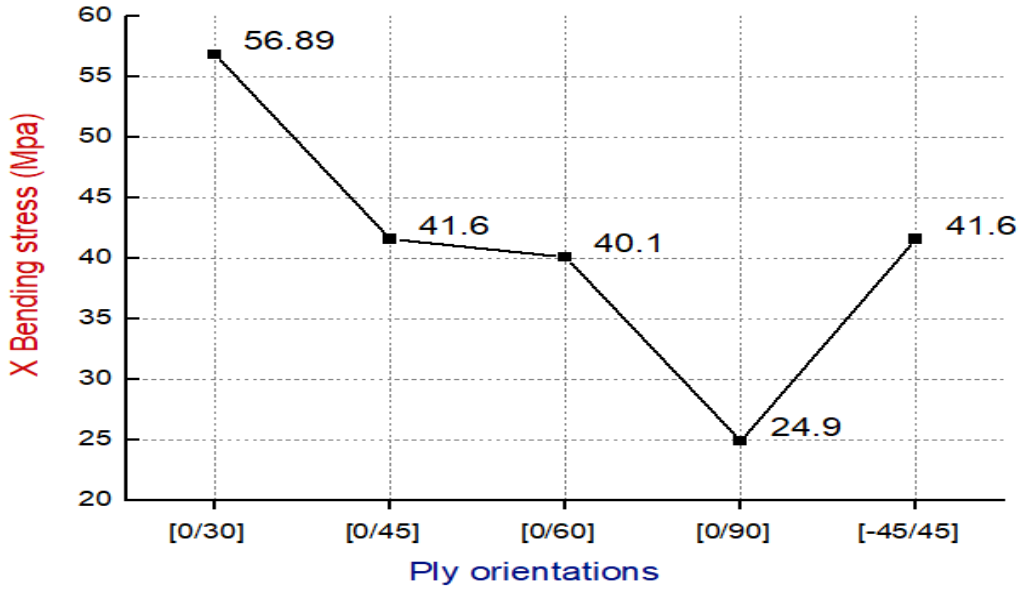

Figure 42 X Bending stress Vs. Ply orientations

Figure 43 Y Bending stress Vs. Ply orientations

The other important static structural output parameter of equivalent stress result on the wing composite ply orientation shows some variations. The maximum and minimum equivalent stress occur at the [-45/45-45/45/-45] and [0/90/0/90/0] ply orientations. At the same time, the corresponding values are 87.393 Mpa and 61.99 Mpa, respectively.

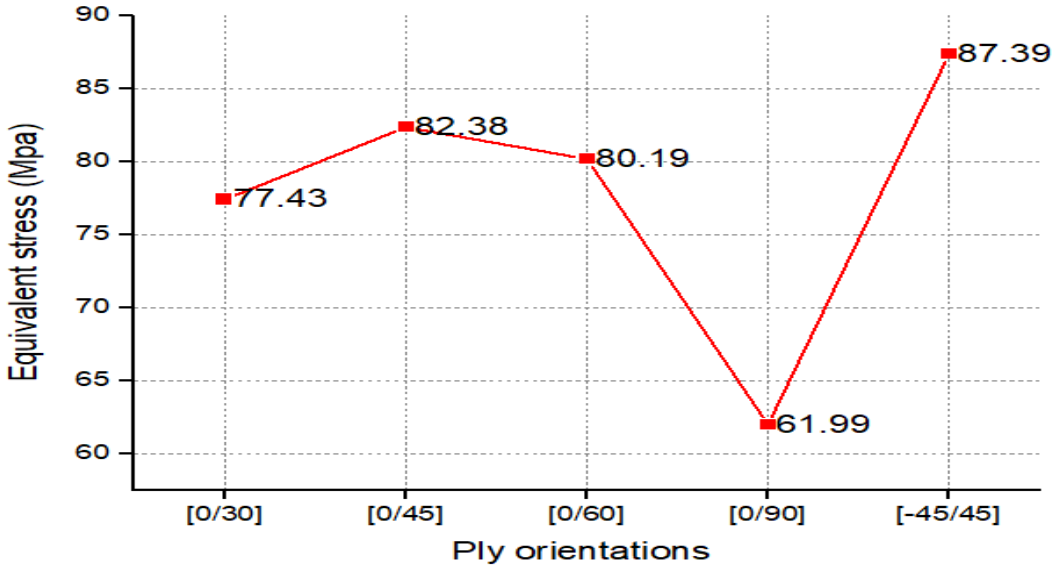

Figure 44 Equivalent stress Vs. Ply orientations

4.3 Modal analysis result

The modal analysis has an output parameter of Natura frequency and corresponding mode shape. The study evaluated two-parameter to determine the effect of spar location and ply orientation on the composite wing. This Study used Six modes for the evaluation, and from the observation, the natural frequency value increased from mode 1 to mode 6.

4.3.1 Modal analysis result on the first parametric Study

The modal analysis analyzed the wing model of six-mode natural frequency and corresponding mode shapes under gravitational loading conditions for all models. The first mode natural frequencies are 5.8738 Hz, whereas the sixth mode natural frequency is 121.03 Hz. The mode shapes have their corresponding deformation, while their direction and type depend on the model number, including bending and torsional deformations. For example, in the first three modes, the maximum deformation occurs at the tip of the wing, while the fourth-mode shape has a maximum deformation value close to the tip area. On the other hand, modes 5 and 6 have maximum deformation values near half of the Wing area due to their torsional deformation behaviors.

The following figure shows the mode shape of all the six modes for the Wing model under both loading conditions. The color contour is the same as static structural results

where the blue region indicates less deformation area and the red part higher deformation areas.

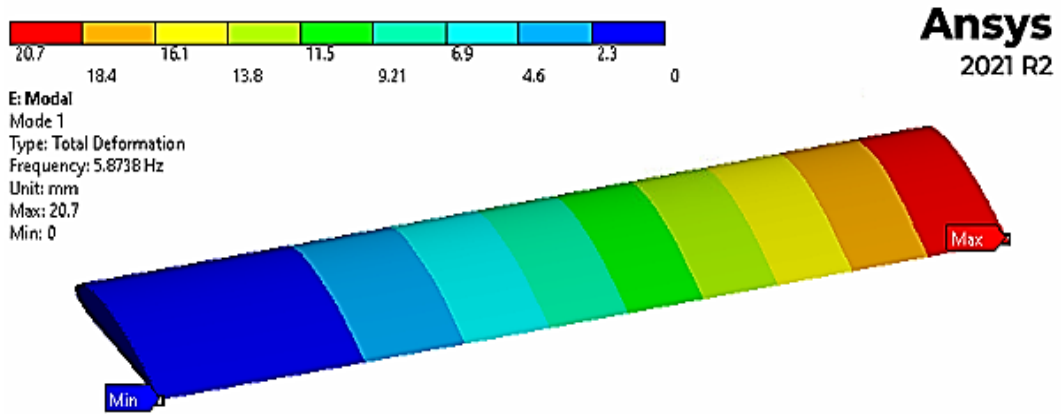

Mode 1

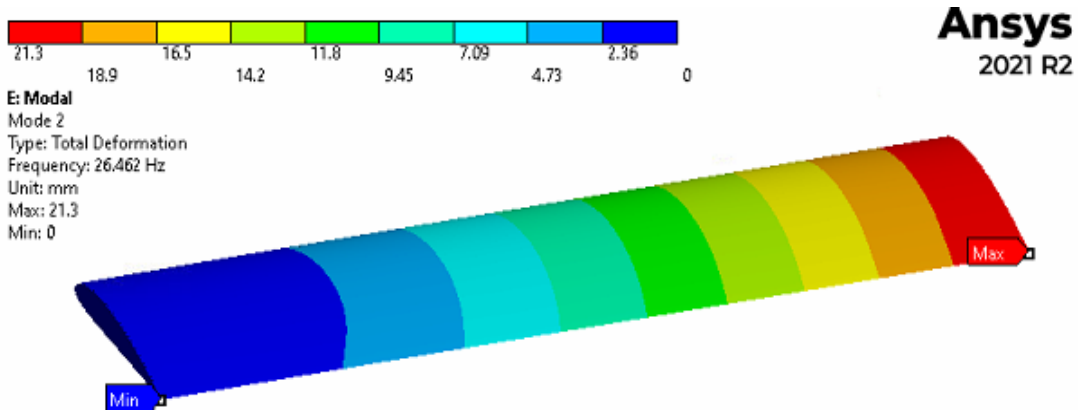

Mode 2

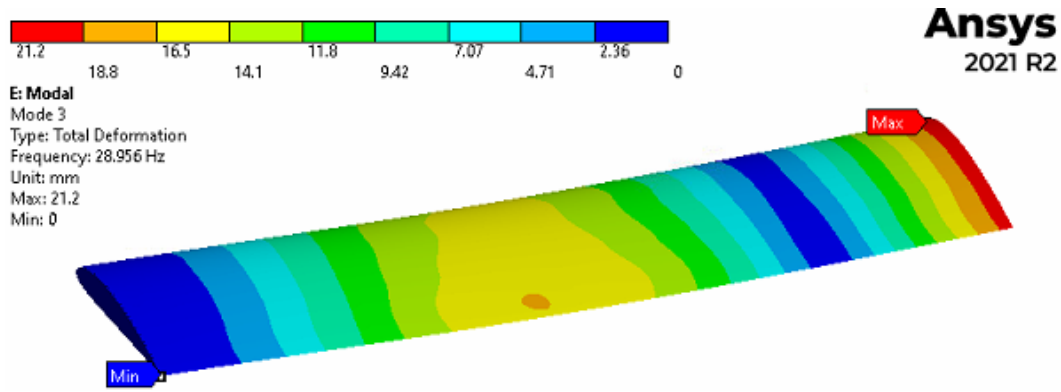

Mode 3

Figure 45 Mode shape of the wing for the first three modes

Figure (42) below shows that the last three modes have a high natural frequency, which leads to higher deformation on the wing. The last mode has a natural frequency value of 121.03 Hz with 45.6 mm deformation.

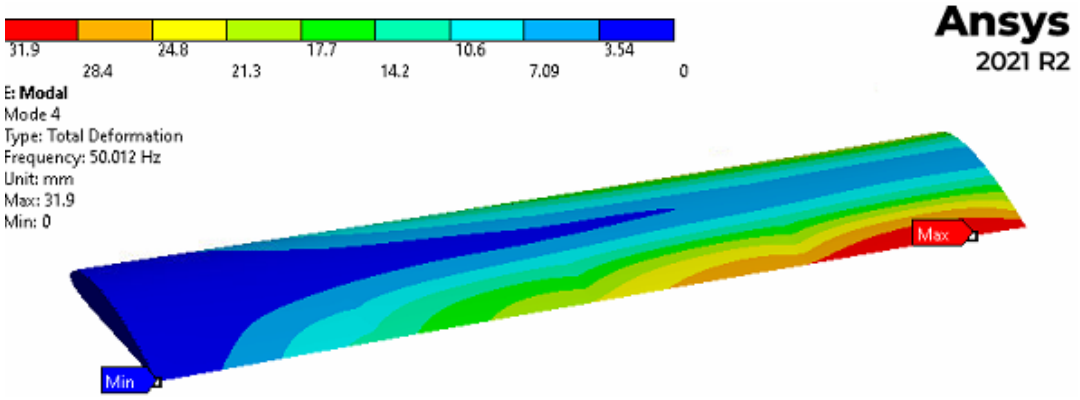

Mode 4

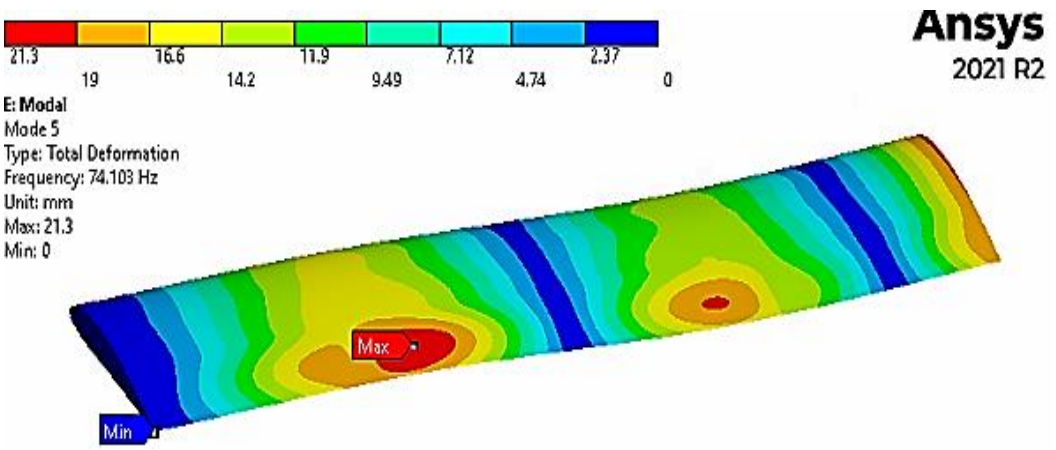

Mode 5

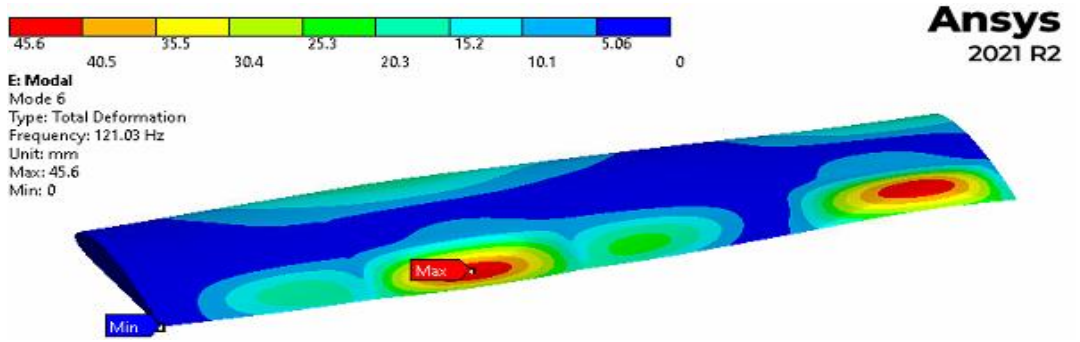

Mode 6

Figure 46 Mode shapes of the wing for the last three modes

The effect of spar location on the natural frequency of the wing has a relatively small influence on the value of all six modes. The first model has a somewhat higher natural frequency value than the other models, which indicates that as the wing's spar is away from the wing's leading edge, it will have a better vibration response. Likewise, as the two spars are close to each other, it helps the Wing experience a better vibration response. The third model has less natural frequency on all six modes. Still, when we see all numerical values, the difference in the natural frequency for all models doesn't significantly affect the composite wing.

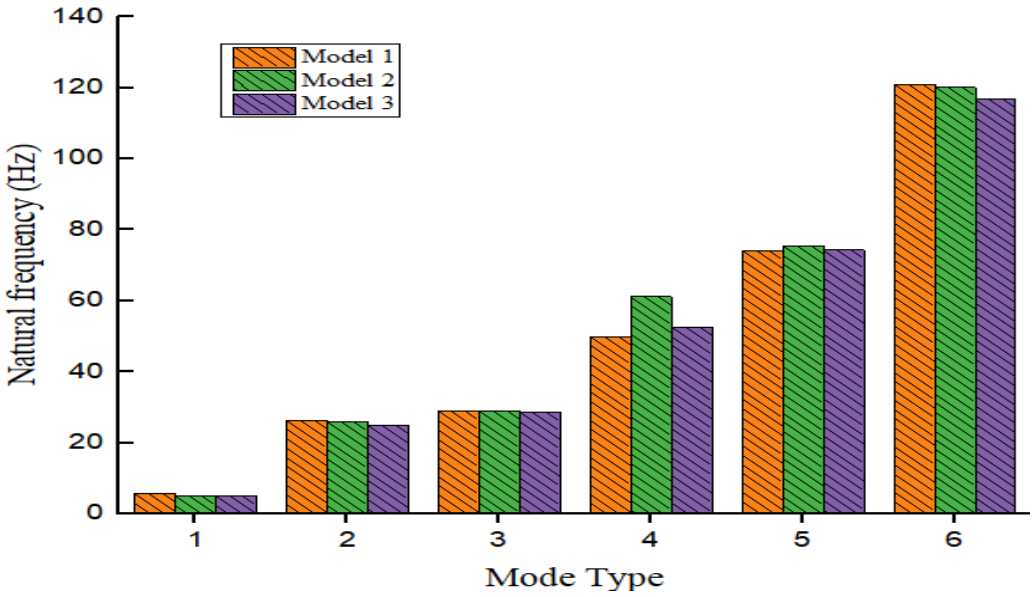

Figure 47 Comparison of Natural frequency for all models

4.3.2 Modal analysis result on the second parametric Study

Varying Ply orientation of composite material on the Wing skin has a significant effect on the natural frequency of the Wing model. In all ply orientations cases, the natural frequency increases from mode one to mode six while changing its values depends on the orientation. The maximum and minimum natural frequency of mode 1 occur at [0/90/0/90/0] and [0/30/0/30/0], respectively, and their corresponding value is 11.65 Hz and 7.15 Hz. In the case of the fourth mode, the maximum and minimum values of frequency occur at [-45/45/-45/45/-45] and [0/90/0/90/0], respectively, and the corresponding values are 92.3 Hz and 60.62 Hz. The last mode [0/90/0/90/0] ply orientation shows less value of 97.58 Hz, and [0/30/0/30/0] shows a higher natural frequency with its value of 128.58 Hz first five-mode natural frequency values are

relatively less in this ply orientation. (Zaki et al., 2019) also studied the effect of laminate orientation on the bending and torsional frequency and found that the cross-ply [90] and [-90] have a better modal response. The figure below shows the natural frequency value of all six modes Vs. Composite ply orientation.

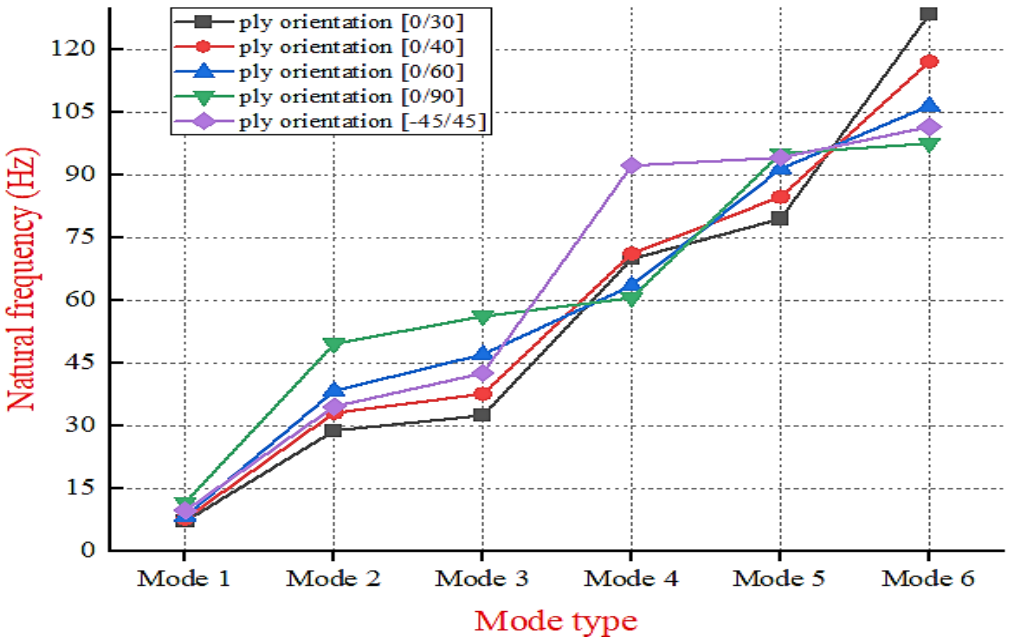

Figure 48 Wing skin ply orientation Vs. Natural frequency

From observation, the first and last mode has an inverse natural frequency effect on the ply orientation of the Wing skin. If we change the ply orientation, the natural frequency will increase in the first mode, and it will decrease in the last mode, which indicates the first and last mode has indirect relation.

CHAPTER FIVE

5 CONCLUSION AND RECOMMENDATION

5.1 Conclusion

In this study, the static structural and modal analysis of the composite UAV Wing was performed. Carbon Epoxy is the composite material used for the wing, and half of the wing is considered for analysis, with one end fixed and the other end free. Furthermore, the research conducted a parametric study on spar placement and Wing skin ply orientation. The first parametric Study analyzed three models, whereas the second parametric Study analyzed five different scenarios under gravitational and aerodynamic loading conditions.

In the case of static structural analysis, the output parameters are the total deformation, maximum shear stress, and bending stress. The effect of spar location and composite ply orientation results concludes as follow:

- The Spar location of the wing has a significant effect on the deformation, bending, equivalent and shear stress. The study shows that spar away from the wing leading edge increases the deformation, bending, equivalent and shear stress due to the high-pressure load acting near the leading edge, and it needs more reinforcement in this area.
- In the case of varying spar locations, model 1 shows better structural performance, and model 2 shows less structural performance. From the results of the two models, the value of deformation, bending, Equivalent, and maximum shear stress was maximum at model 2.
- The effect of composite ply orientation on the static structural analysis shows [0/30/0/30/0] arrangement has the highest deformation, whereas [0/90/0/90/0] has lower deformation. On the other hand, maximum shear stress was high at [-45/45/-45/45/-45] and low at [0/90/0/90/0]. Moreover, bending and equivalent stress is maximum at [0/30/0/30/0] and minimum at [0/90/0/90/0], which indicates the cross-ply [0/90/0/90/0] arrangement shows better structural performance.

In the case of modal analysis, the output parameters are natural frequency and mode shape for the first six modes. The effect of spar location and skin ply orientation on the natural frequency and mode shapes is summarized as follow:

- The natural frequency of all models shows an increase from mode 1 to mode 6.
- From the result of the three models, it was observed the model with a spar away from the leading-edge shows better modal response, and when the two spars are close to each other, it will have a better modal response with less natural frequency results.
- The Wing skin ply orientation impacts the natural frequency value as the angle ply increases its first three and the fifth mode increases during the fourth and sixth decrease. From observation, the [0/0/0/0/0] ply angle has fewer natural frequency values in the first five modes, while [0/90/0/90/0] has a less natural frequency in the last sixth mode.

5.2 Recommendation

This research should consider the following suggestions to get the best structural performance on composite UAV Wing models.

- The Wing spar located near the leading edge has better performance and can withstand the high aerodynamic pressure load.
- The front and rear spars should be as close as possible to one other to reduce total Wing deformation.
- [0/90/0/90/0] ply orientation can reduce the total deformation, bending, Equivalent and maximum shear stress.
- By employing [0/0/0/0/0] orientation for the first modes, it can reduce the natural frequency of the Wing model, and the last mode [0/90/0/90/0] has a better response.

5.3 Future work

Currently, the UAV technology is generating interest in research domains, and future studies could include the following suggestion: -

- It may also take into account varying loading circumstances for different flight scenarios.
- The Study can include different thicknesses for internal structures like Wing skin, spars, and ribs in the composite model to see the effect of deformations and the structure natural frequency.
- The different composite materials could be considered for the Wing model

REFERENCE

Aliywy, a. M. (2017). Design and analysis of NACA 0016 wing rib and stringers by using al-7075 and kevlar. International journal of engineering and advanced technology (IJEAT), 6(5), 31–36.

Anderson, k. et al. (2015). Vibration analysis of an embedded actuator-based UAV. Journal of vibration analysis, measurement, and control, 3(3), 174–193. Https://doi.org/10.7726/jvamc.2015.1010

Arif, m., Asif, m., & Ahmed, d. (2017). Advanced composite material for aerospace application-a review. International journal of engineering and manufacturing science, 7(2), 393–409.

Basri et al. (2019). Using Schrenk's approximation, UAV naca4415 Wing structural performance analysis subjected to external aerodynamic load. Journal of advanced research in fluid mechanics and thermal sciences, 60(2), 178–190.

Basri, e. I., et al. (2019). Performance analysis of composite ply orientation in the aeronautical application of unmanned aerial vehicle (UAV) naca4415 wing. Journal of materials research and technology, 8(5), 3822–3834. Https://doi.org/10.1016/j.jmrt.2019.06.044

Bayraktar, m.,& Ali, d. (2019). Free vibration analysis of an aircraft wing by considering a cantilever beam. Selcuk university journal of engineering, science, and technology, 7(1), 12–21. Https://doi.org/10.15317/scitech.2019.178

Canonsburg, a. D. (2017). Ansys fluent tutorial guide. January.

Choudhury, a., Mondal, s. C., & sarkar, s. (2019). Failure analysis of laminated composite plate under hydro-thermomechanical load and optimization. International journal of applied mechanics and engineering, 24(3), 509–526. Https://doi.org/10.2478/ijame-2019-0032

Dwivedi, b. (2007). Theory of flight (first edition). Https://doi.org/10.2307/j.ctt5vkh8r.6

Eftekhari, s., & al-obaidi, a. S. M. (2019). Investigation of a naca0012 finite Wing aerodynamics at low Reynolds s numbers and 0 ° to 90 ° angle of attack. J. Aerosp. Technol. Manag, 11(1519), 1–11. Https://doi.org/10.5028/jatm.v11.1023

Fairuz, z. et al. (2016). Effect of Wing deformation on the aerodynamic performance of flapping wings: fluid-structure interaction approach. Journal of aerospace engineering, 29(4), 04016006. Https://doi.org/10.1061/(ASCE)as.1943-5525.0000548

Gloria, a., montanari, r., richetta, m., & varone, a. (2019). Alloys for aeronautic applications: state of the art and perspectives. Metals, 9(662), 1–26. Https://doi.org/doi:10.3390/met9060662

Hallad, s. et al. (2018). Kevlar reinforced polymer matrix composite for structural application. IOP conference series: materials science and engineering, 376(1). Https://doi.org/10.1088/1757-899x/376/1/012074

Hasan, m. S., svorcan, j., & simonovic, a. M. (2019). Cfd analysis of a high-altitude long-endurance UAV wing. 7th international congress of Serbian society of mechanicsKarlovic, June. Https://www.researchgate.net/publication/334083646

Jacob olaitan, a., nnaemeka, j.-a., & danladi king, g. (2017). Graphite-epoxy composite design for aircraft wing spar using computational techniques – part i. American journal of mechanical engineering, 5(4), 117–127. Https://doi.org/10.12691/ajme-5-4-2

Jain, r., jain, s., & bajpai, l. (2016). Aerodynamics of winglet: a computational fluid dynamics study using fluent. International research journal of engineering and technology (IRJET), 03(06), 250–254.

Kanesan, g., mansor, s., & abdul-latif, a. (2014a). Validation of UAV Wing structural model for finite element analysis. Jurnal Teknologi, 71(2), 1–5. Https://doi.org/10.11113/jt.v71.3710

Kathiravan, t., A, m. H., Parthiban, k., & university-Chennai, a. (2018). Structural and modal analysis of subsonic aircraft wing using Ansys workbench. International research journal of engineering and technology (IRJET), 05(10), 823–827.

Kaushik, y. (2017). A review on the use of aluminum alloys in aircraft components. i-manager's journal o vol. Material science, 3(3). Https://www.researchgate.net/publication/319456144

Kavya, g., & reddy, b. C. R. (2015). Design and finite element analysis of aircraft wing using ribs and spars. International journal and magazine of engineering, technology, management and research, 2(11), 1443–1455.

Khchine, y. E. L., & Sriti, m. (2017). Boundary layer and mesh refinement effects on aerodynamic performances of horizontal axis wind turbine (hawt). International journal of mechanical engineering, 2, 119–125.

Körpe, s. (2019). The aerodynamic optimization of a UAV wing is subject to weight, geometric, root bending moment, and performance constraints. International journal of aerospace engineering, Hindawi, 2019. Https://doi.org/10.1155/2019/3050824

Krishna et al. (2016). Vibration and CFD analysis of composite aircraft wing in subsonic airflow. International advanced research journal in science, engineering, and technology (IARJSET), 3(12), 66–73. Https://doi.org/10.17148/iarjset.2016.31214

Kumar, a. R., Balakrishnan, s. R., & Balaji, s. (2013). Design of an aircraft wing structure for static analysis and fatigue life prediction. International journal of engineering research & technology (IJERT), 2(5), 1154–1158.

Kumar das, s., & Roy, s. (2018). Finite element analysis of aircraft wing using carbon fiber reinforced polymer and glass fiber reinforced polymer. IOP conference series: materials science and engineering, 402(1). Https://doi.org/10.1088/1757-899x/402/1/012077

Kurtulus, d. F. (2017). Effect of Wing deformation on aerodynamic loads at supersonic speeds. 9th Ankara international aerospace conference, September. Https://www.researchgate.net/publication/319980254

Liang, y., chin, p., sun, y., & wang, m. (2021). Design and manufacture of composite landing gear for an alight unmanned aerial vehicle. Appl. Sci., 11(509). Https://doi.org/https://doi.org/10.3390/app11020509

Liu et al. (2019). Study on the flight performance of propeller-driven UAVs. International journal of aerospace engineering, 2019. Https://doi.org/10.1155/2019/6282451

M., t. (2014). 3-d cad modeling and modal analysis of light aircraft wing. International scientific journal "machines. Technologies. Materials, 53(3), 51–53.

Maksimović stevan, et al. (2013). Structural analysis and static strength testing of a tactical unmanned aerial vehicle. Scientific, technical review, 63(2), 58–62.

Mangalgiri, p. D. (1999). Composite materials for aerospace applications. Bulletin of materials science, 22(3), 657–664. Https://doi.org/10.1007/bf02749982

Maria, m. (2013). Advanced composite materials of the future in the aerospace industry. Incas bulletin, 5(3), 139–150. Https://doi.org/10.13111/2066-8201.2013.5.3.14

Mathai, a., kurian, a. P., jacob, b., k, n. M., & baby, t. R. (2014). Linear static analysis of CFRP aircraft wing. Int. Journal of engineering research and applications, 4(4), 199–202.

Mosaad, a., & abdelmonaem, a. (2019). Aerodynamic CFD simulation study of a commercial aircraft model. 4thiugrcinternational undergraduate research conference, august 4–11. Https://www.researchgate.net/publication/334882915

Nikhil a. Khadse, & prof. S. R. Zaweri. (2015). Modal analysis of aircraft wing using Ansys workbench software package. International journal of engineering research & technology (IJERT), v4(07), 225–230. Https://doi.org/10.17577/ijertv4is070291

Pugazhenthi, v., gopalakannan, s., & rajappan, r. (2018). Finite element analysis of composite shell structure of aircraft wing using composite structure. 2018 IEEE international conference on a system, computation, automation, and networking, ICSCA 2018, 74–80. Https://doi.org/10.1109/icscan.2018.8541192

Rajak, d. K., Pagar, d. D., menezes, p. L., & linul, e. (2019). Fiber-reinforced polymer composites polymers, 11.

Ramkumar, n. V, & Mankar, r. L. (2017). Weight optimization of windmill shaft by composite material using FEA. 1045(4), 138–145.

Rao et al. (2011). Effect of composition of fibers on properties of hybrid composites. International Journal of macromolecular science, 1(1), 9–14.

R. Jones. (1975). Mechanics of composite materials.

Sadraey, m. (2017). Unmanned aircraft design. Morgan & Claypool publishers series. Https://doi.org/10.2200/s00789ed1v01y201707mec004 a

Saran, v., et al. (2017). Analysis of natural frequency for an aircraft wing structure under pre-stress conditions. International journal of mechanical engineering and technology, 8(8), 1118–1123.

Saripalli, b., pandu, r., & john, v. (2015). Vibration and CFD analysis of hybrid composite wing. International journal of novel research in electrical and mechanical engineering, 2(3), 105–116.

Sawadi, a. L. I. S. (2017). Analysis of composite material for a wing of aircraft. International journal of mechanical engineering (IJME), 6(3), 19–26.

Sureka, k., & satya meher, r. (2015). Modeling and structural analysis on a300 flight wing by using Ansys. Int. J. Mech. Eng., 4(2), 123–130.

Valavanis, k. P., & Vachtsevanos, g. J. (2015). Handbook of unmanned aerial vehicles. In the handbook of unmanned aerial vehicles. Https://doi.org/10.1007/978-90-481-9707-1

Verma et al. (2018). Challenge and advantage of materials in design and fabrication of composite UAV challenge and materials in design and fabrication of composite UAV. IOP conference series: materials science and engineering paper. Https://doi.org/10.1088/1757-899x/455/1/012005

Vijayanandh, et al. (2018). Material optimization of a high-speed micro aerial vehicle using FSI simulation. Procedia computer science, 133, 2–9. Https://doi.org/10.1016/j.procs.2018.07.002

Yashas Gowda et al. (2018). Polymer matrix-natural fiber composites: an overview. Cogent Engineering, 5(1), 1–13. Https://doi.org/10.1080/23311916.2018.1446667

Yayli et al. (2017). Design optimization of a fixed-wing aircraft. Advances in aircraft and spacecraft science, 4(1), 65–80. Https://doi.org/10.12989/aas.2017.4.1.065

Yu, j. (2018). Design and optimization of wing structure for a fixed-wing unmanned aerial vehicle (UAV). Modern mechanical engineering, 08(04), 249–263. Https://doi.org/10.4236/mme.2018.84017

Zhang, y., Xiong, F., & Yang, s. (2011). Numerical simulation for composite Wing structure design optimization of a mini-type unmanned aerial vehicle. Open mechanical engineering journal, 5(1), 11–18. Https://doi.org/10.2174/1874155x01105010011

APPENDIX

1. NACA 4415 Coordinate

Key Point	X	Y	Key Point	X	Y
1	1	0	50	0.00107	-0.00566
2	0.99893	0.00039	51	0.00428	-0.01102
3	0.99572	0.00156	52	0.00961	-0.0159
4	0.99039	0.00349	53	0.01704	-0.02061
5	0.98296	0.0061	54	0.02653	-0.02502
6	0.97347	0.00932	55	0.03806	-0.02915
7	0.96194	0.01303	56	0.05156	-0.03281
8	0.94844	0.01716	57	0.06699	-0.03582
9	0.93301	0.02166	58	0.08427	-0.03817
10	0.91573	0.02652	59	0.10332	-0.03991
11	0.89668	0.03171	60	0.12408	-0.04106
12	0.87592	0.03717	61	0.14645	-0.04166
13	0.85355	0.04283	62	0.17033	-0.04177
14	0.82967	0.04863	63	0.19562	-0.04147
15	0.80438	0.05453	64	0.22221	-0.04078
16	0.77779	0.06048	65	0.25	-0.03974
17	0.75	0.06642	66	0.27886	-0.03845
18	0.72114	0.07227	67	0.30866	-0.037
19	0.69134	0.07795	68	0.33928	-0.03547
20	0.66072	0.08341	69	0.37059	-0.0339
21	0.62941	0.08858	70	0.40245	-0.03229
22	0.59755	0.09341	71	0.43474	-0.03063
23	0.56526	0.09785	72	0.4673	-0.02891
24	0.5327	0.10185	73	0.5	-0.02713
25	0.5	0.10538	74	0.5327	-0.02529
26	0.4673	0.10837	75	0.56526	-0.0234
27	0.43474	0.11076	76	0.59755	-0.02149

28	0.40245	0.11248	77	0.62941	-0.01958
29	0.37059	0.11345	78	0.66072	-0.01772
30	0.33928	0.11361	79	0.69134	-0.01596
31	0.30866	0.11294	80	0.72114	-0.0143
32	0.27886	0.11141	81	0.75	-0.01277
33	0.25	0.10903	82	0.77779	-0.01136
34	0.22221	0.10584	83	0.80438	-0.01006
35	0.19562	0.1019	84	0.82967	-0.00886
36	0.17033	0.09726	85	0.85355	-0.00775
37	0.14645	0.09195	86	0.87592	-0.00674
38	0.12408	0.08607	87	0.89668	-0.00583
39	0.10332	0.0797	88	0.91573	-0.00502
40	0.08427	0.07283	89	0.93301	-0.00431
41	0.06699	0.06541	90	0.94844	-0.00364
42	0.05156	0.05753	91	0.96194	-0.00297
43	0.03806	0.04937	92	0.97347	-0.00227
44	0.02653	0.04118	93	0.98296	-0.00156
45	0.01704	0.03303	94	0.99039	-0.00092
46	0.00961	0.02489	95	0.99572	-0.00042
47	0.00428	0.01654	96	0.99893	-0.00011
48	0.00107	0.00825	97	1	0
49	0	0.00075			

2. Parametric study result

2.1 First Parametric study result

Static analysis result

Model 1

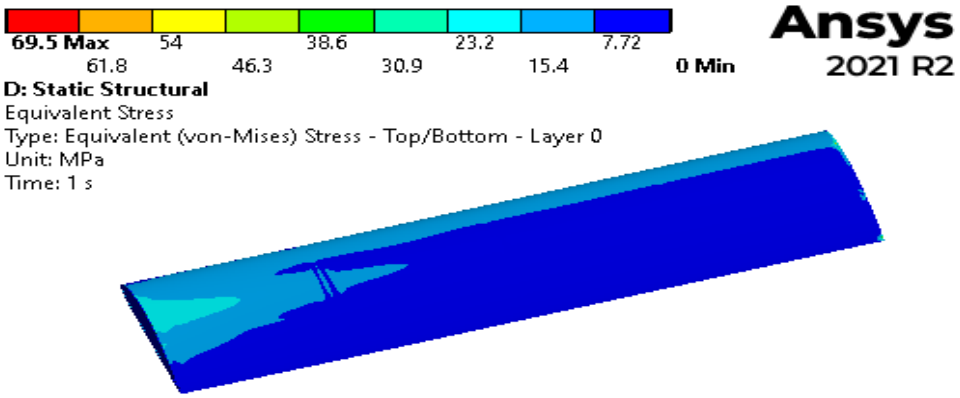

Model 2

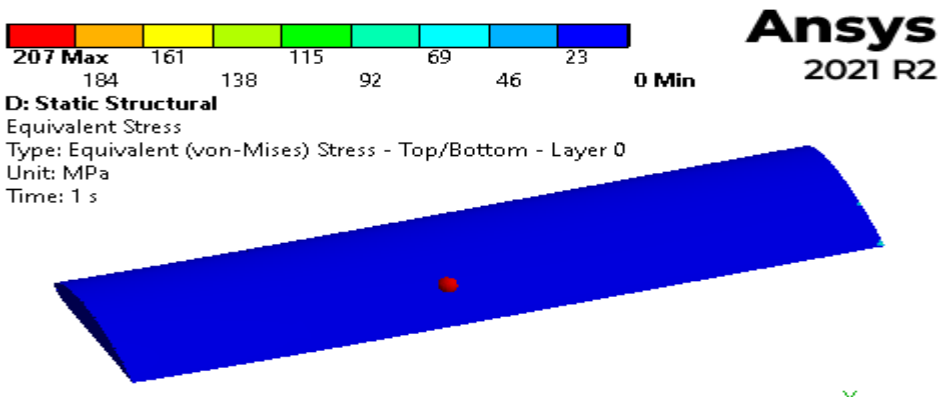

Model 3

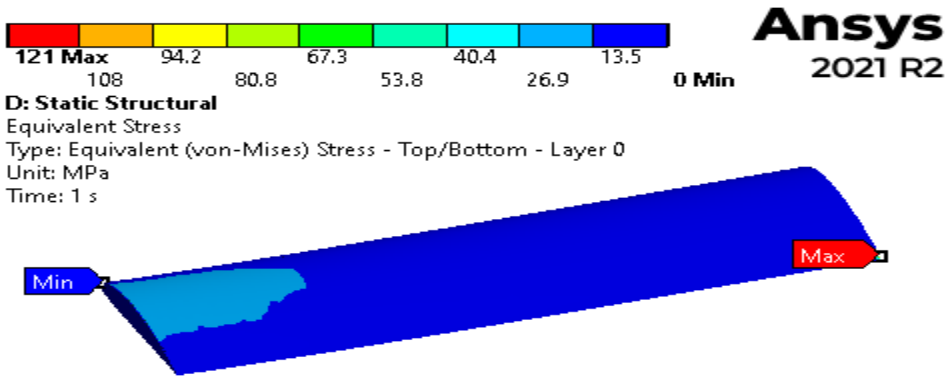

Modal analysis result

Model 2

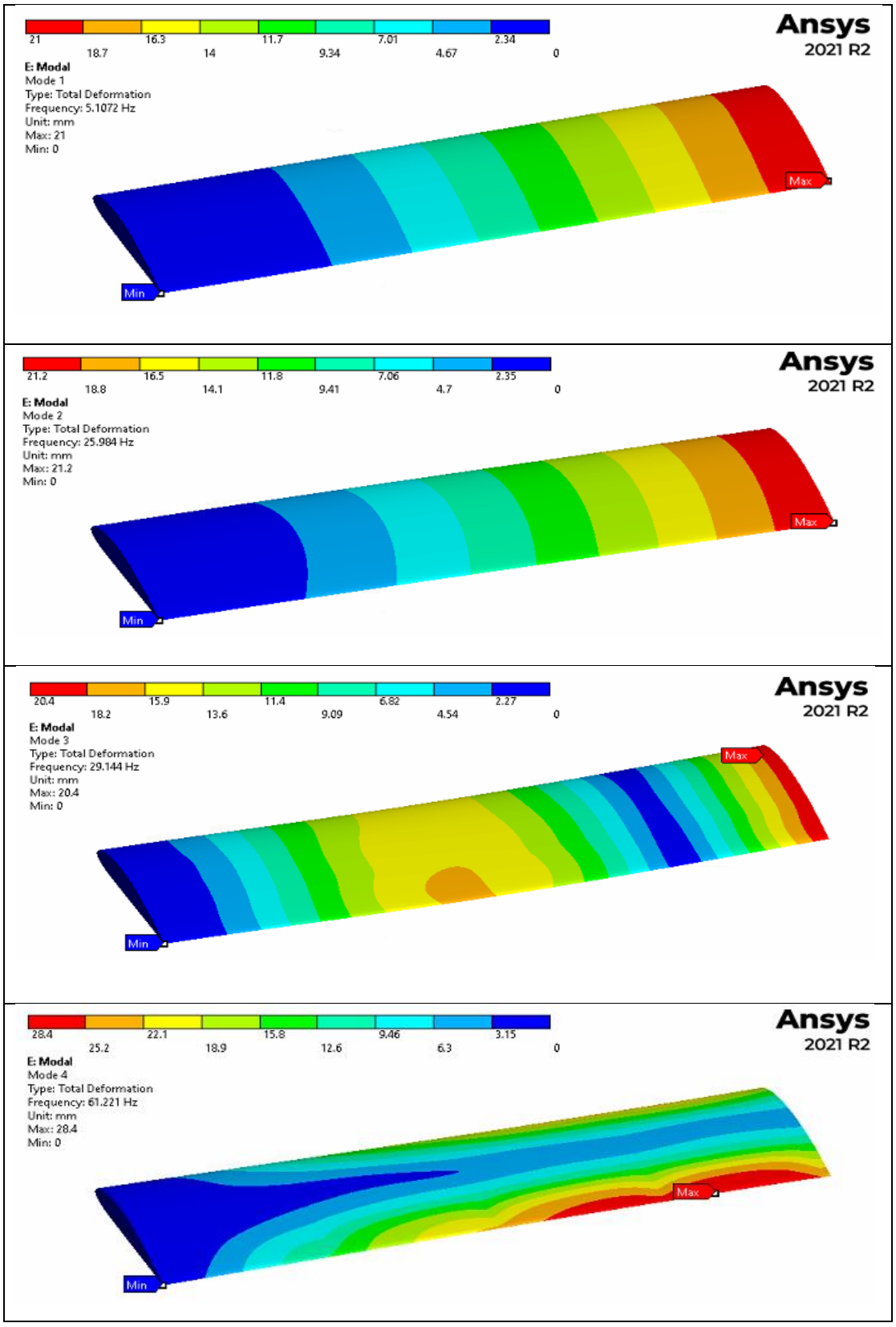

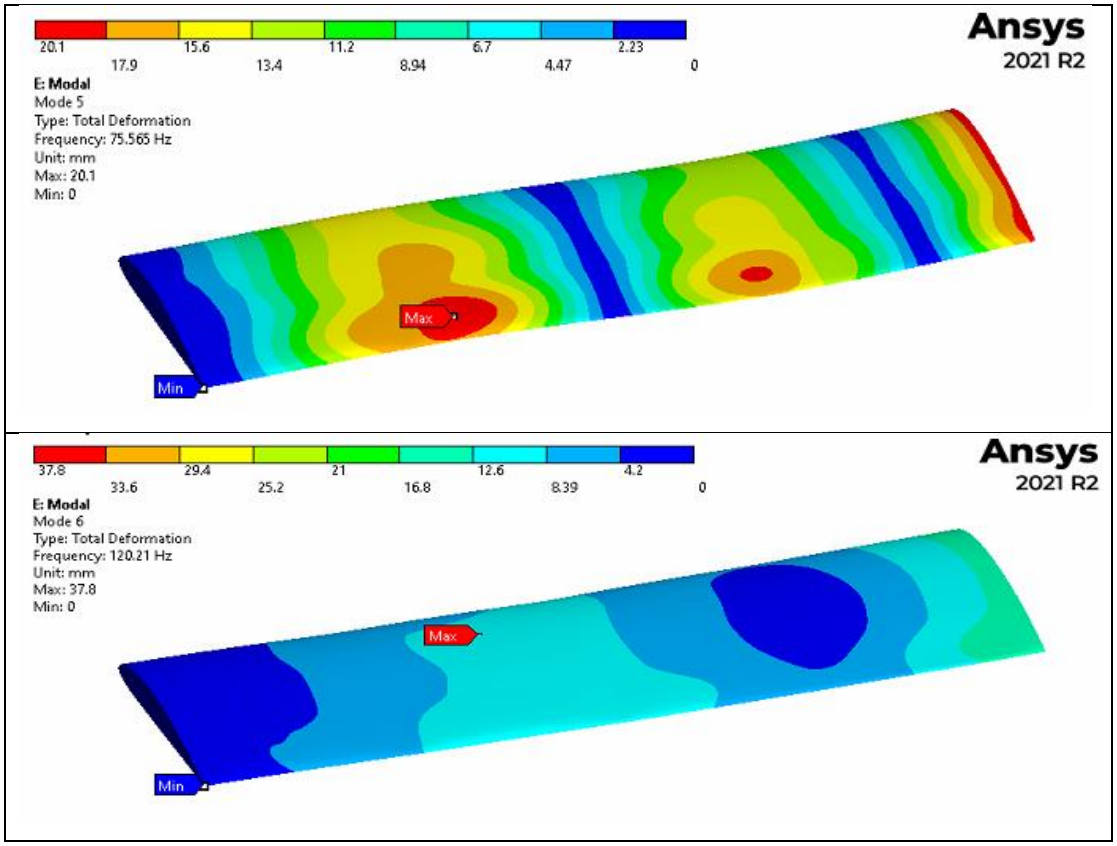
20.1
17.9
15.6
13.4
11.2
8.94
6.7
4.47
2.23
0
Ansys
2021 R2
E: Modal
Mode 5
Type: Total Deformation
Frequency: 75.565 Hz
Unit: mm
Max: 20.1
Min: 0
Max
Min
37.8
33.6
29.4
25.2
21
16.8
12.6
8.39
4.2
0
Ansys
2021 R2
E: Modal
Mode 6
Type: Total Deformation
Frequency: 120.21 Hz
Unit: mm
Max: 37.8
Min: 0
Max
Min

Model 3

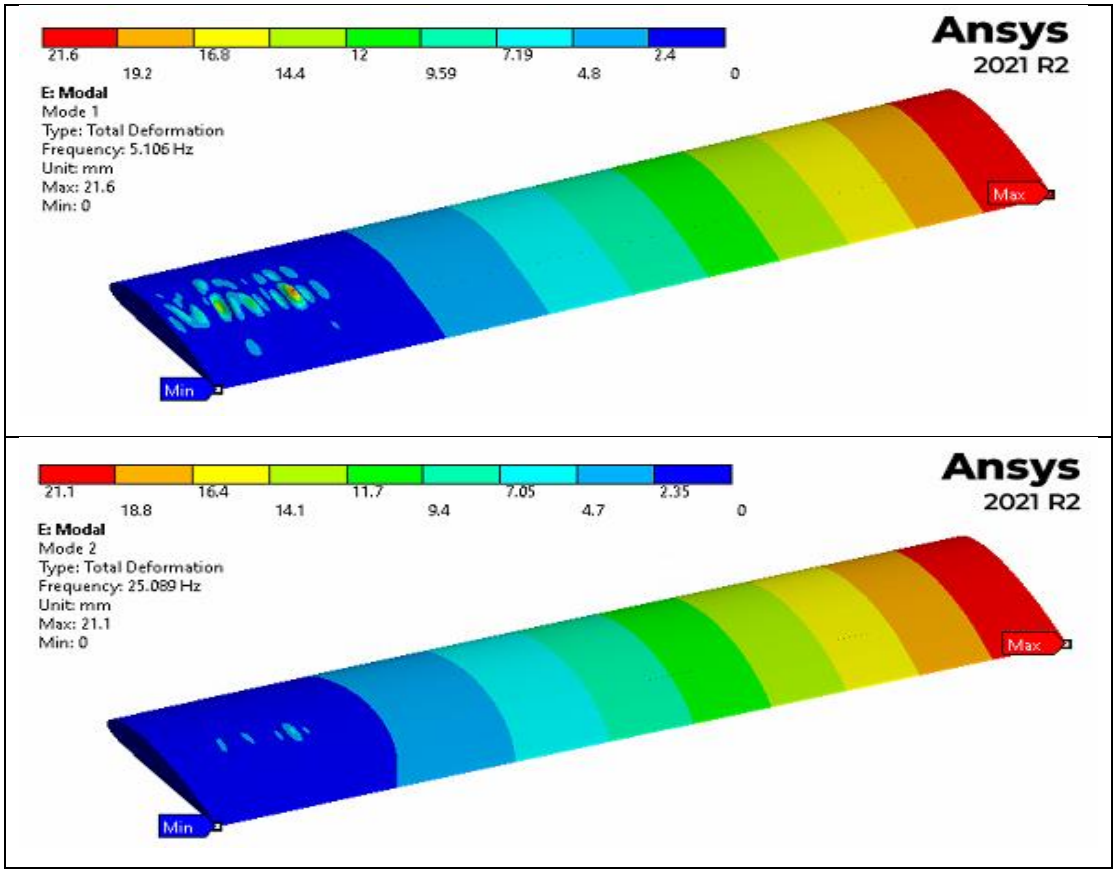
21.6
19.2
16.8
14.4
12
9.59
7.19
4.8
2.4
0
Ansys
2021 R2
E: Modal
Mode 1
Type: Total Deformation
Frequency: 5.106 Hz
Unit: mm
Max: 21.6
Min: 0
Max
Min
21.1
18.8
16.4
14.1
11.7
9.4
7.05
4.7
2.35
0
Ansys
2021 R2
E: Modal
Mode 2
Type: Total Deformation
Frequency: 25.089 Hz
Unit: mm
Max: 21.1
Min: 0
Max
Min

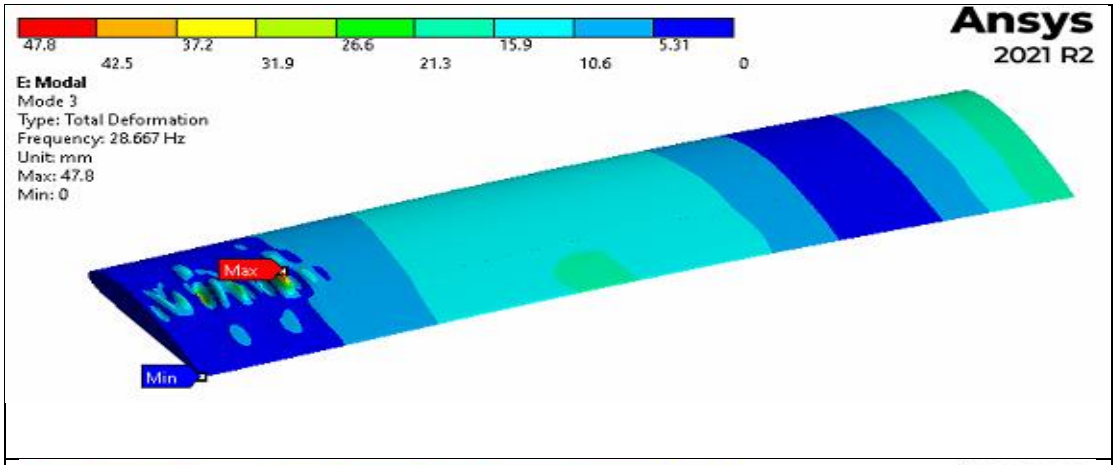
47.8
42.5
37.2
31.9
26.6
21.3
15.9
10.6
5.31
0
E: Modal
Mode 3
Type: Total Deformation
Frequency: 28.667 Hz
Unit: mm
Max: 47.8
Min: 0
Max
Min
Ansys
2021 R2

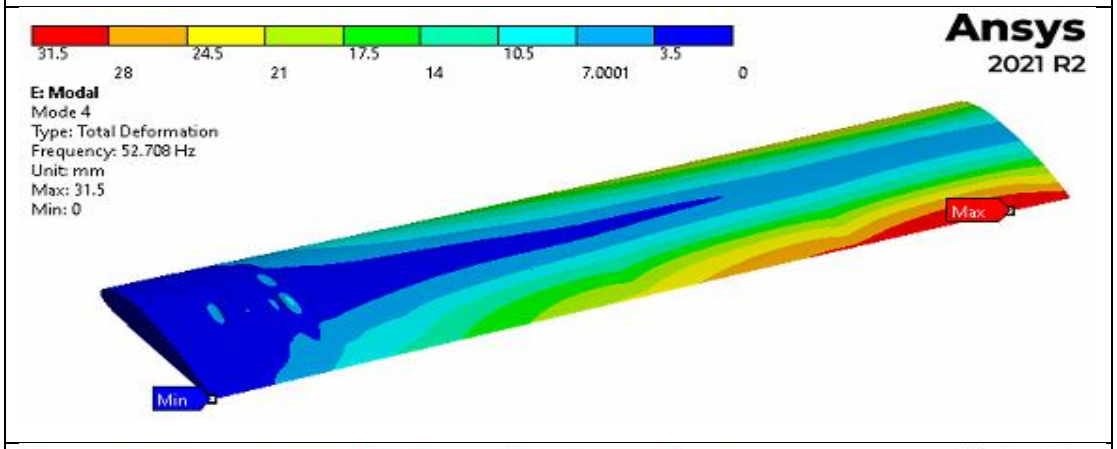
31.5
28
24.5
21
17.5
14
10.5
7.0001
3.5
0
E: Modal
Mode 4
Type: Total Deformation
Frequency: 52.708 Hz
Unit: mm
Max: 31.5
Min: 0
Max
Min
Ansys
2021 R2

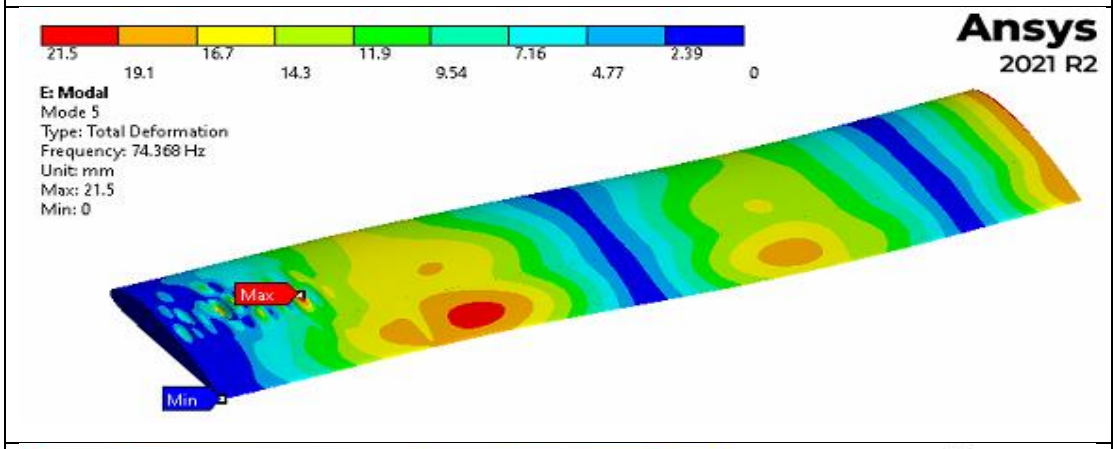
21.5
19.1
16.7
14.3
11.9
9.54
7.16
4.77
2.39
0
E: Modal
Mode 5
Type: Total Deformation
Frequency: 74.368 Hz
Unit: mm
Max: 21.5
Min: 0
Max
Min
Ansys
2021 R2

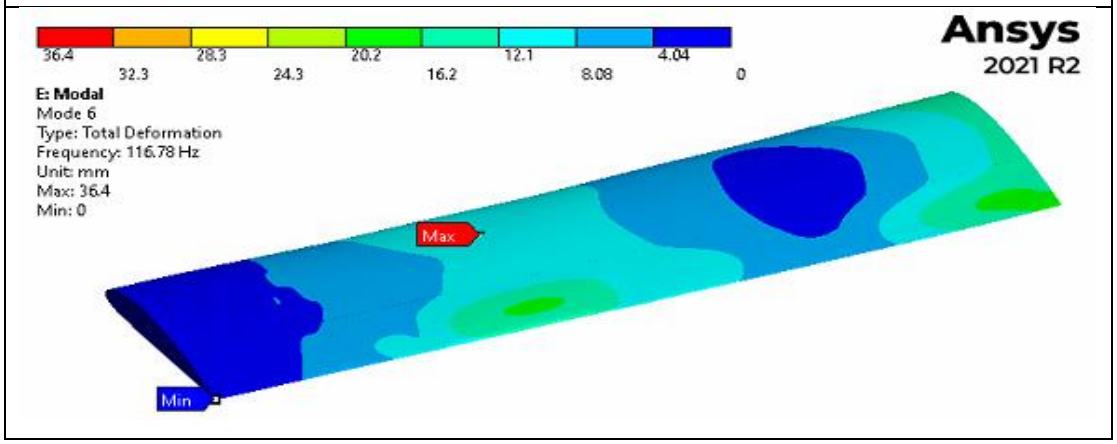
36.4
32.3
28.3
24.3
20.2
16.2
12.1
8.08
4.04
0
E: Modal
Mode 6
Type: Total Deformation
Frequency: 116.78 Hz
Unit: mm
Max: 36.4
Min: 0
Max
Min
Ansys
2021 R2

2.2 Second parametric study result

The static structural analysis result

Case 1

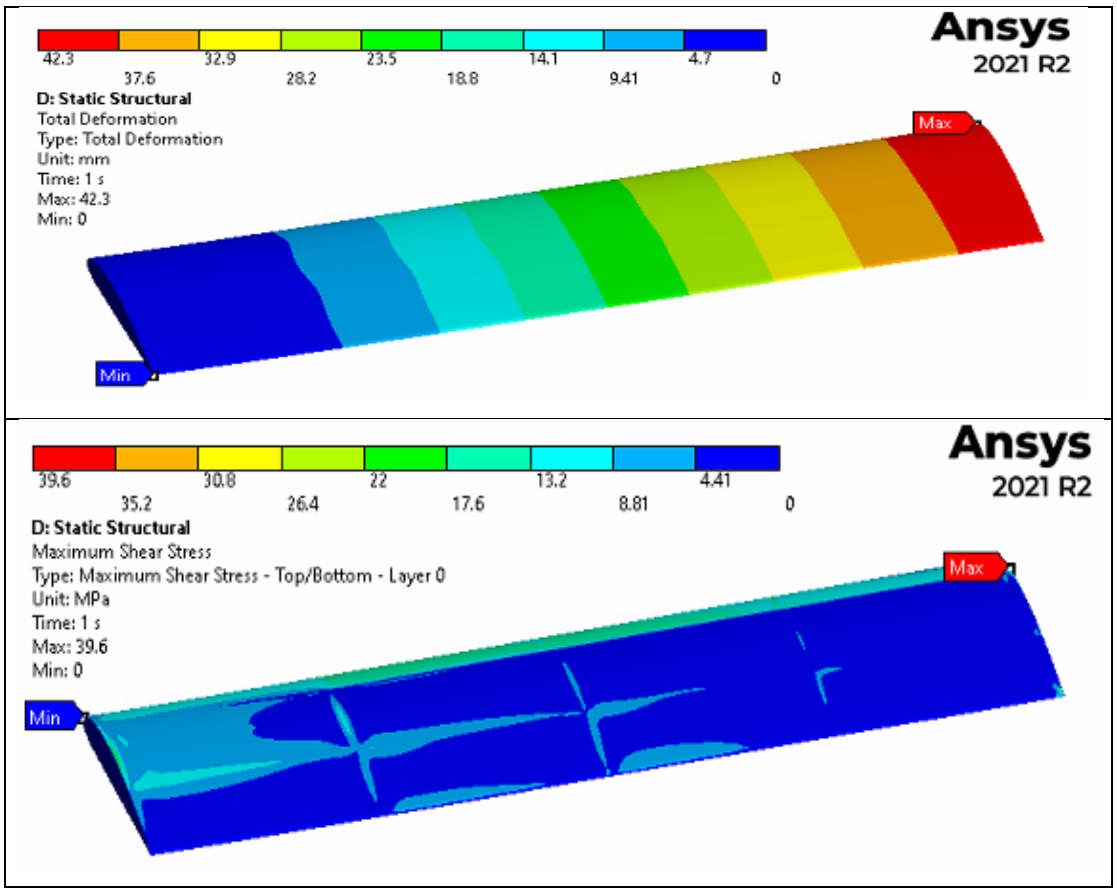

Case 2

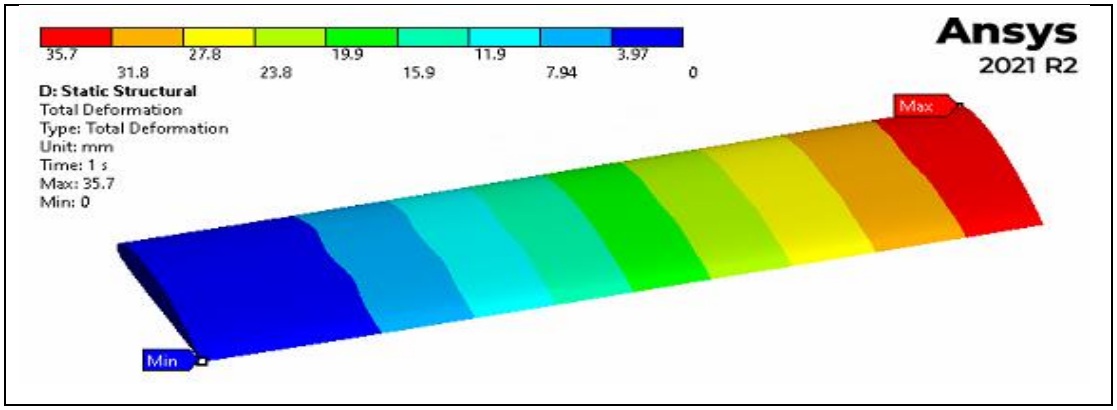

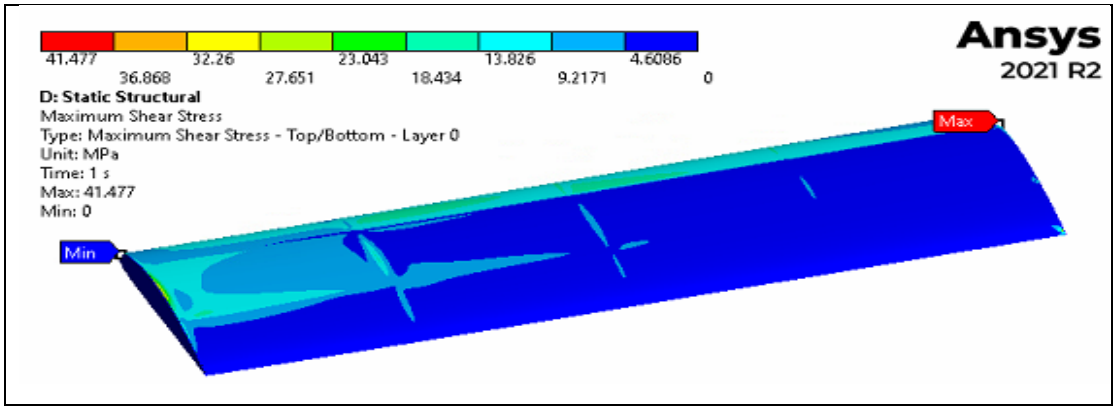
41.477
36.868
32.26
27.651
23.043
18.434
13.826
9.2171
4.6086
0
Ansys
2021 R2
D: Static Structural
Maximum Shear Stress
Type: Maximum Shear Stress - Top/Bottom - Layer 0
Unit: MPa
Time: 1 s
Max: 41.477
Min: 0
Max
Min

Case 3

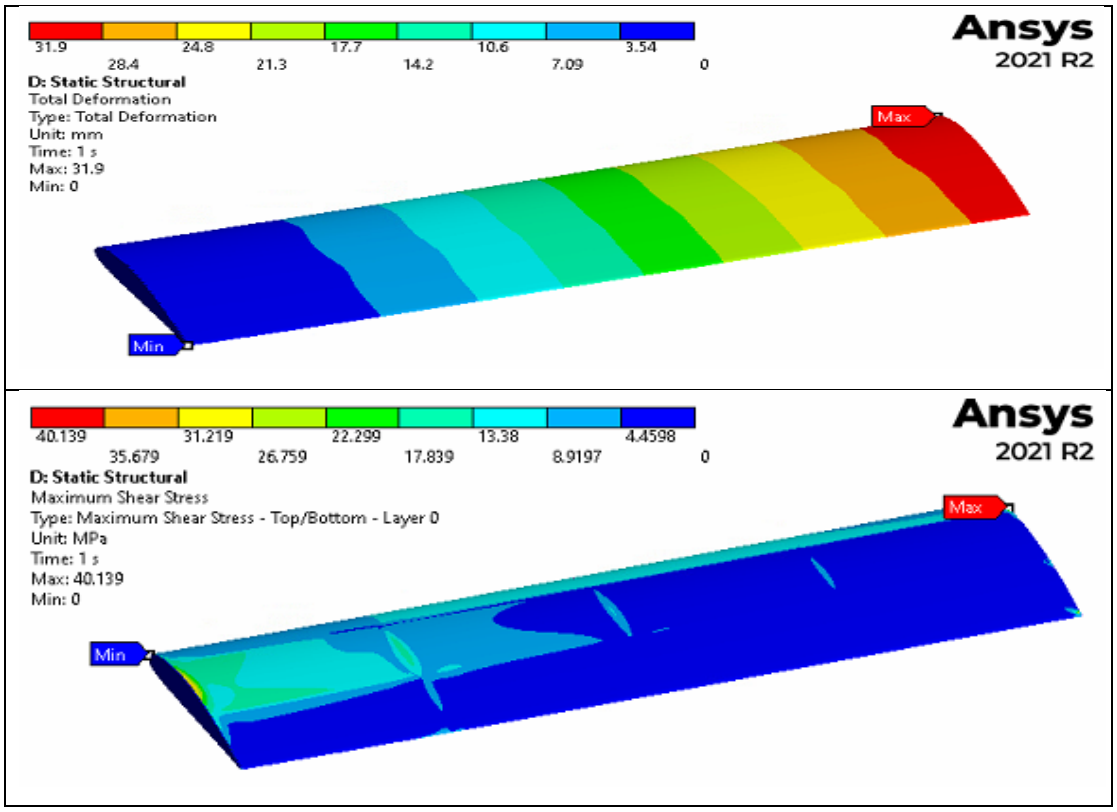
31.9
28.4
24.8
21.3
17.7
14.2
10.6
7.09
3.54
0
Ansys
2021 R2
D: Static Structural
Total Deformation
Type: Total Deformation
Unit: mm
Time: 1 s
Max: 31.9
Min: 0
Max
Min
40.139
35.679
31.219
26.759
22.299
17.839
13.38
8.9197
4.4598
0
Ansys
2021 R2
D: Static Structural
Maximum Shear Stress
Type: Maximum Shear Stress - Top/Bottom - Layer 0
Unit: MPa
Time: 1 s
Max: 40.139
Min: 0
Max
Min

Case 4

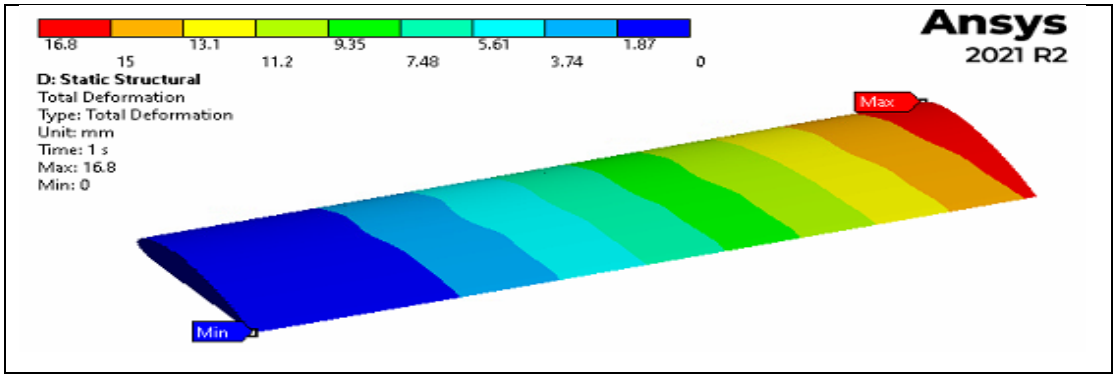
16.8
15
13.1
11.2
9.35
7.48
5.61
3.74
1.87
0
Ansys
2021 R2
D: Static Structural
Total Deformation
Type: Total Deformation
Unit: mm
Time: 1 s
Max: 16.8
Min: 0
Max
Min

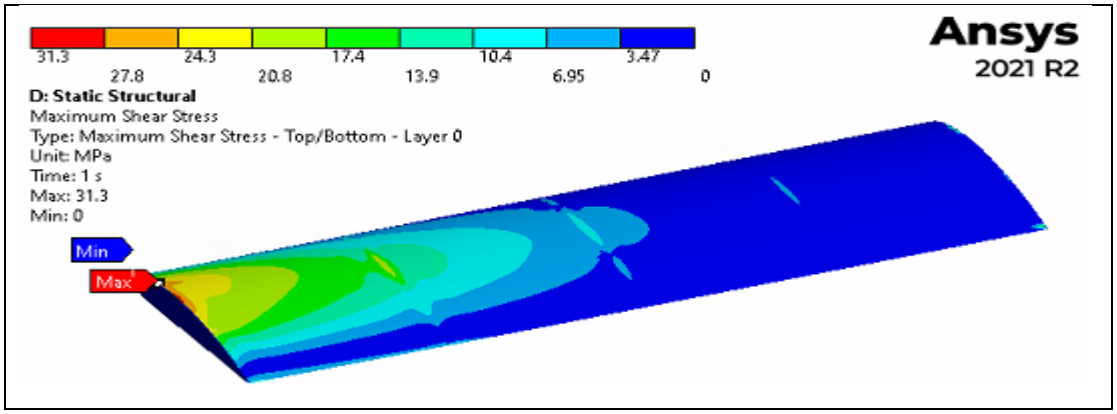

Case 5

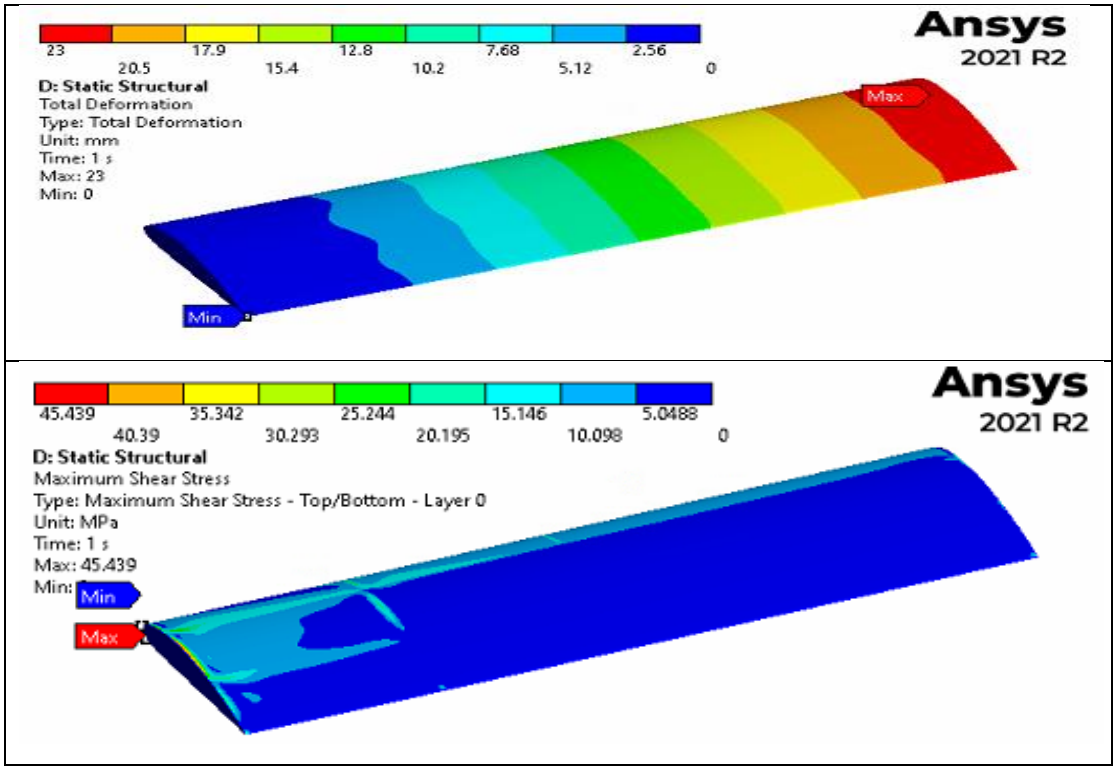

Modal analysis result

Case 1

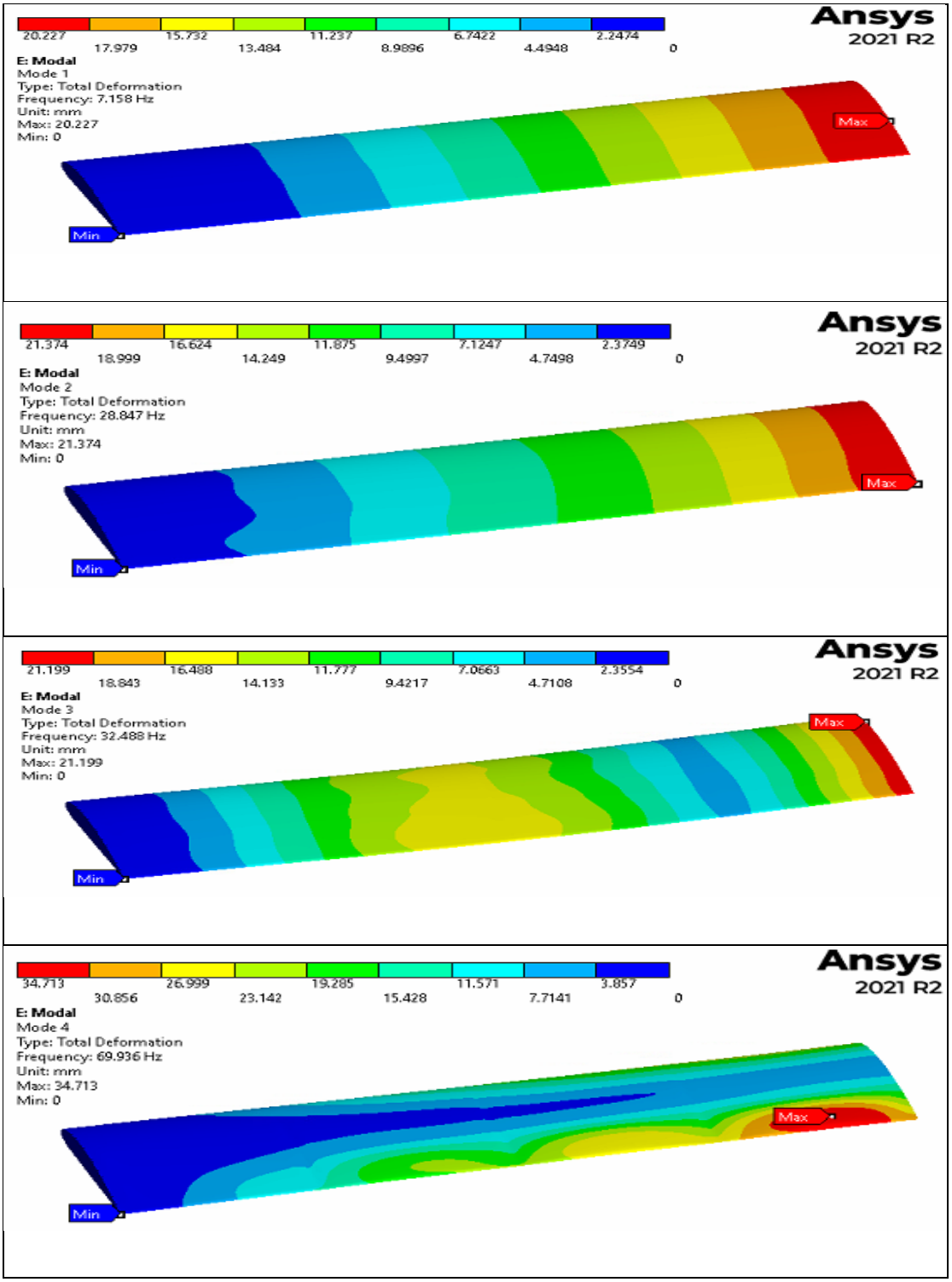
Ansys
2021 R2
20.227
17.979
15.732
13.484
11.237
8.9896
6.7422
4.4948
2.2474
0
E: Modal
Mode 1
Type: Total Deformation
Frequency: 7.158 Hz
Unit: mm
Max: 20.227
Min: 0
Max
Min
Ansys
2021 R2
21.374
18.999
16.624
14.249
11.875
9.4997
7.1247
4.7498
2.3749
0
E: Modal
Mode 2
Type: Total Deformation
Frequency: 28.847 Hz
Unit: mm
Max: 21.374
Min: 0
Max
Min
Ansys
2021 R2
21.199
18.843
16.488
14.133
11.777
9.4217
7.0663
4.7108
2.3554
0
E: Modal
Mode 3
Type: Total Deformation
Frequency: 32.488 Hz
Unit: mm
Max: 21.199
Min: 0
Max
Min
Ansys
2021 R2
34.713
30.856
26.999
23.142
19.285
15.428
11.571
7.7141
3.857
0
E: Modal
Mode 4
Type: Total Deformation
Frequency: 69.936 Hz
Unit: mm
Max: 34.713
Min: 0
Max
Min

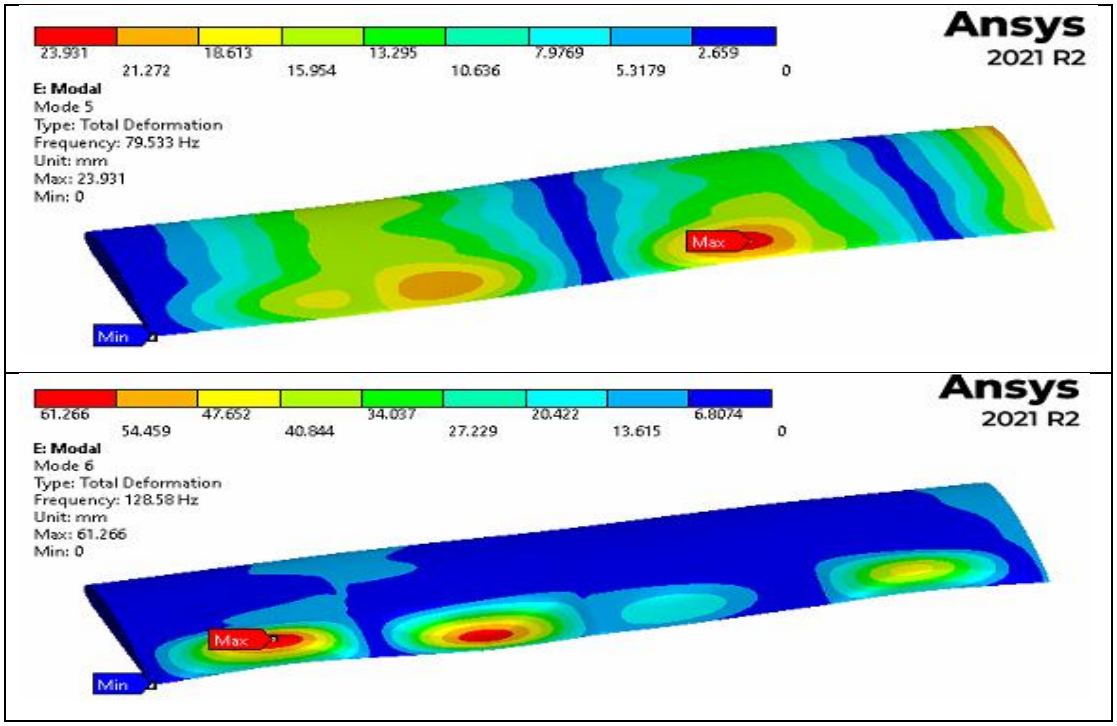
Ansys
2021 R2
23.931
21.272
18.613
15.954
13.295
10.636
7.9769
5.3179
2.659
0
E: Modal
Mode 5
Type: Total Deformation
Frequency: 79.533 Hz
Unit: mm
Max: 23.931
Min: 0
Max
Min
Ansys
2021 R2
61.266
54.459
47.652
40.844
34.037
27.229
20.422
13.615
6.8074
0
E: Modal
Mode 6
Type: Total Deformation
Frequency: 128.58 Hz
Unit: mm
Max: 61.266
Min: 0
Max
Min

Case 2

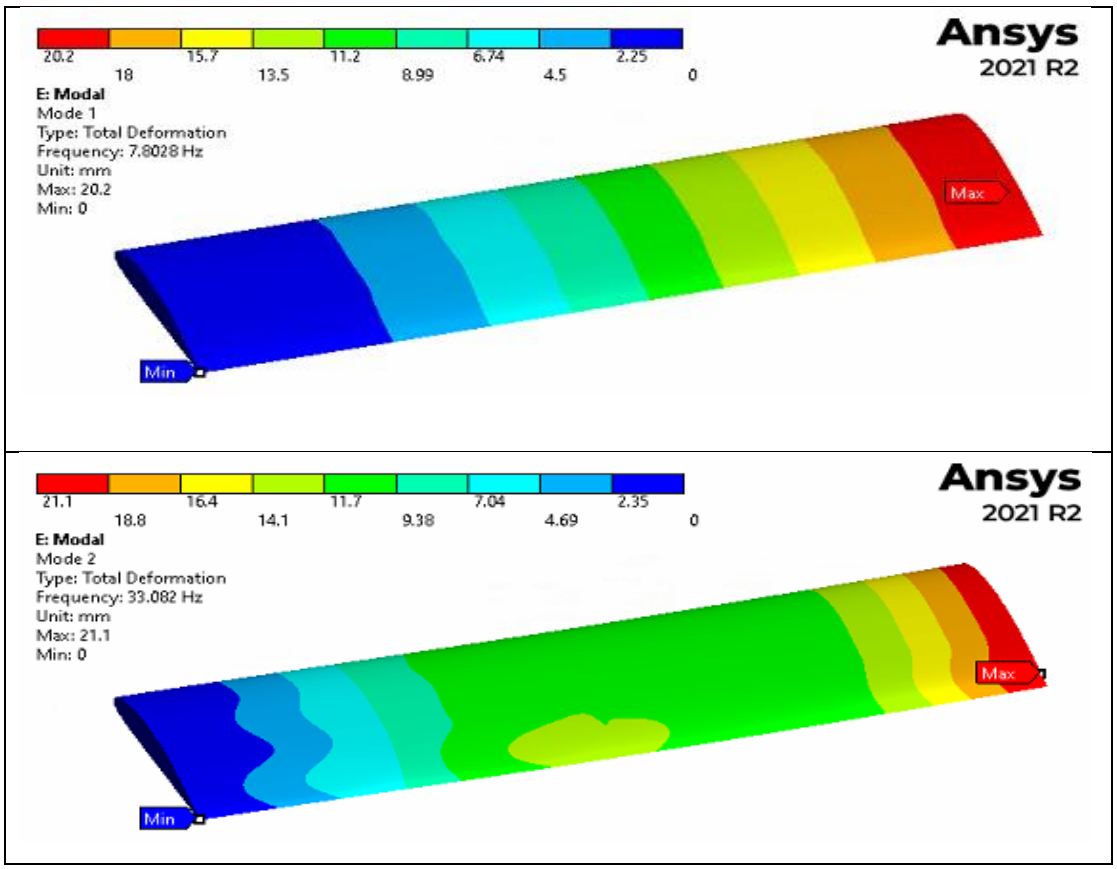
Ansys
2021 R2
20.2
18
15.7
13.5
11.2
8.99
6.74
4.5
2.25
0
E: Modal
Mode 1
Type: Total Deformation
Frequency: 7.8028 Hz
Unit: mm
Max: 20.2
Min: 0
Max
Min
Ansys
2021 R2
21.1
18.8
16.4
14.1
11.7
9.38
7.04
4.69
2.35
0
E: Modal
Mode 2
Type: Total Deformation
Frequency: 33.082 Hz
Unit: mm
Max: 21.1
Min: 0
Max
Min

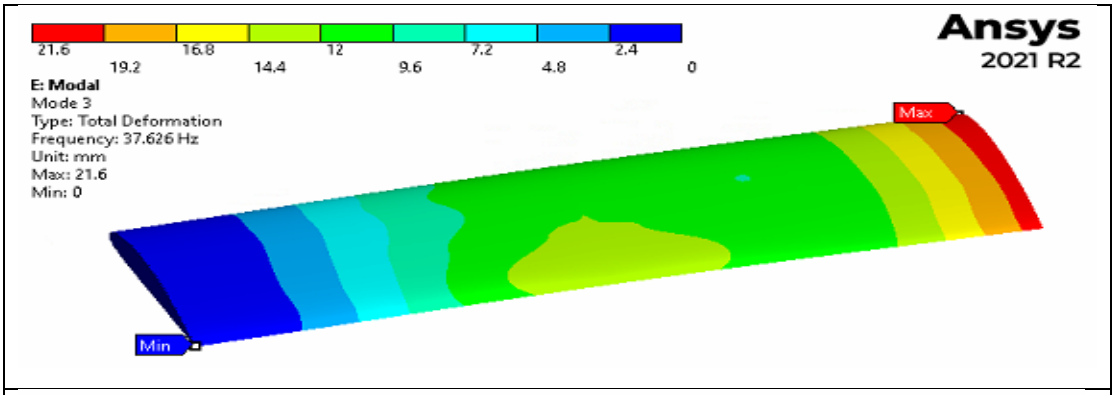
21.6
19.2
16.8
14.4
12
9.6
7.2
4.8
2.4
0
E: Modal
Mode 3
Type: Total Deformation
Frequency: 37.626 Hz
Unit: mm
Max: 21.6
Min: 0
Max
Min
Ansys
2021 R2

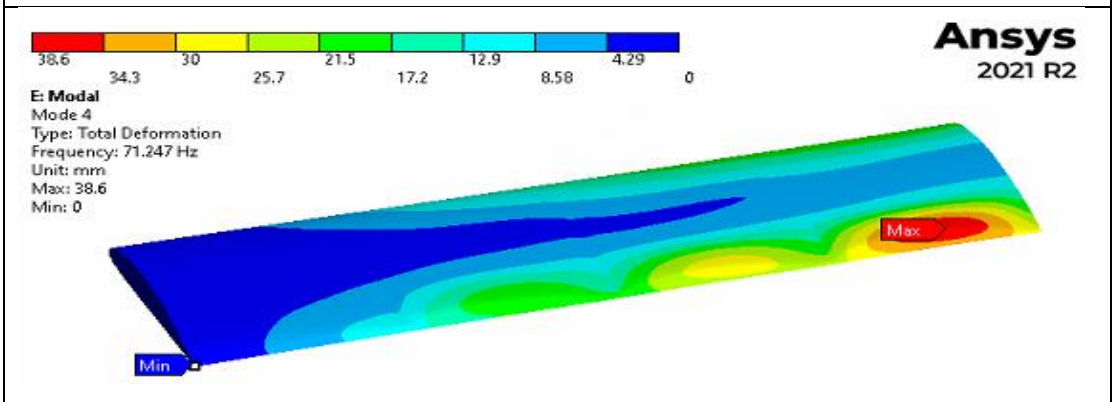
38.6
34.3
30
25.7
21.5
17.2
12.9
8.58
4.29
0
E: Modal
Mode 4
Type: Total Deformation
Frequency: 71.247 Hz
Unit: mm
Max: 38.6
Min: 0
Max
Min
Ansys
2021 R2

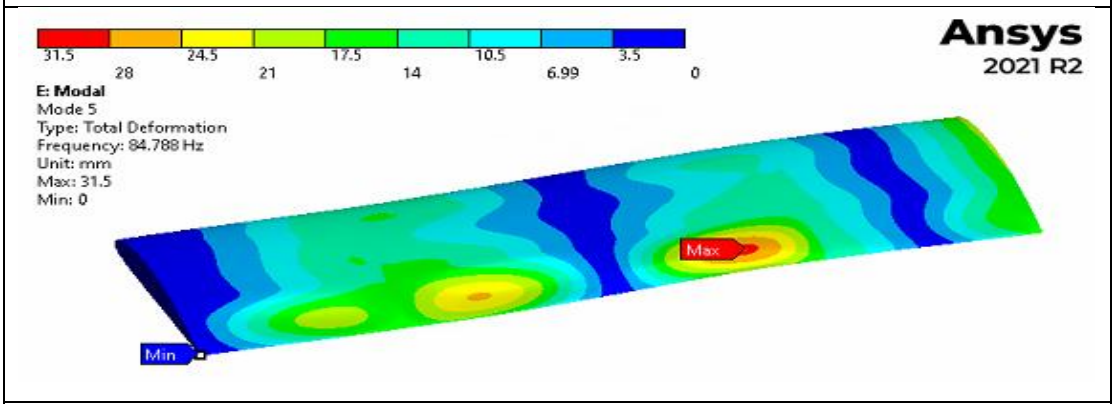
31.5
28
24.5
21
17.5
14
10.5
6.99
3.5
0
E: Modal
Mode 5
Type: Total Deformation
Frequency: 84.788 Hz
Unit: mm
Max: 31.5
Min: 0
Max
Min
Ansys
2021 R2

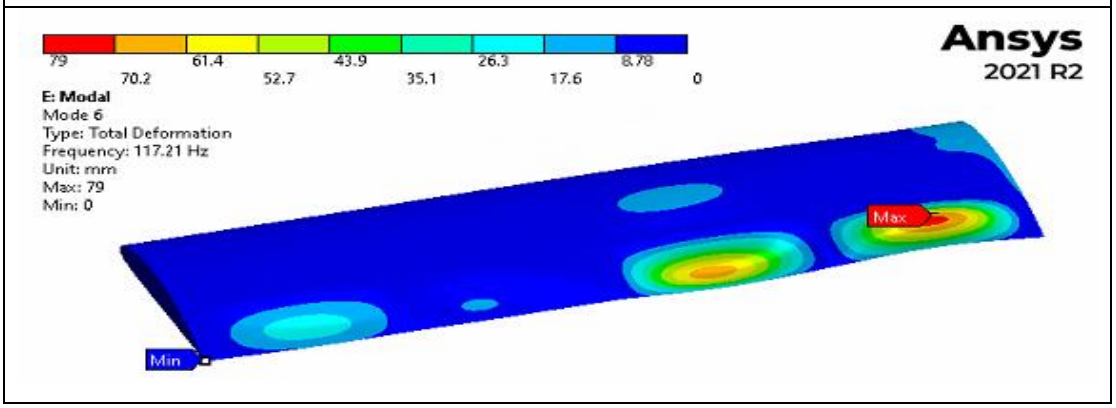
79
70.2
61.4
52.7
43.9
35.1
26.3
17.6
8.78
0
E: Modal
Mode 6
Type: Total Deformation
Frequency: 117.21 Hz
Unit: mm
Max: 79
Min: 0
Max
Min
Ansys
2021 R2

Case 3

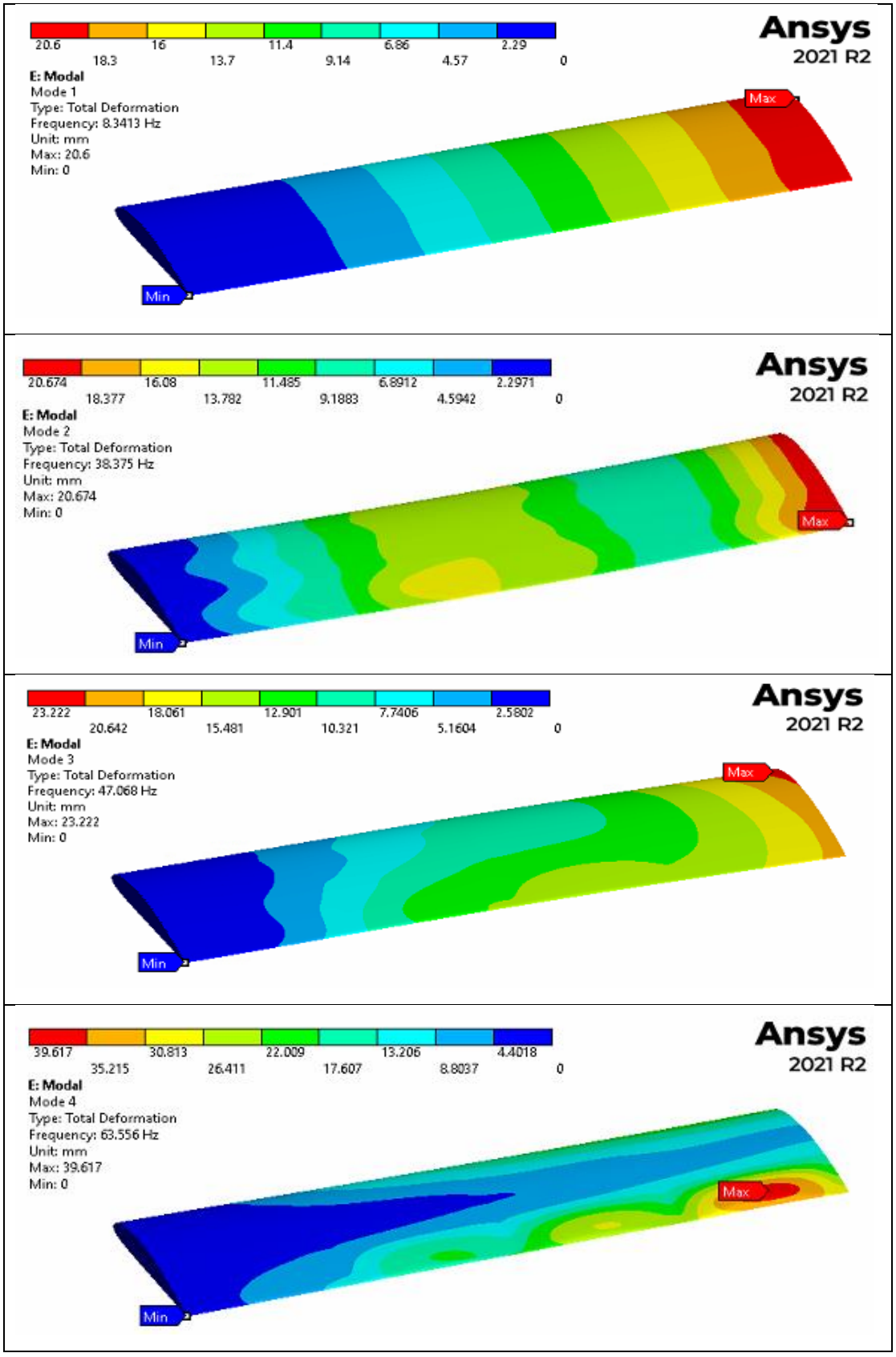
20.6
18.3
16
13.7
11.4
9.14
6.86
4.57
2.29
0
E: Modal
Mode 1
Type: Total Deformation
Frequency: 8.3413 Hz
Unit: mm
Max: 20.6
Min: 0
Max
Min
Ansys
2021 R2
20.674
18.377
16.08
13.782
11.485
9.1883
6.8912
4.5942
2.2971
0
E: Modal
Mode 2
Type: Total Deformation
Frequency: 38.375 Hz
Unit: mm
Max: 20.674
Min: 0
Max
Min
Ansys
2021 R2
23.222
20.642
18.061
15.481
12.901
10.321
7.7406
5.1604
2.5802
0
E: Modal
Mode 3
Type: Total Deformation
Frequency: 47.068 Hz
Unit: mm
Max: 23.222
Min: 0
Max
Min
Ansys
2021 R2
39.617
35.215
30.813
26.411
22.009
17.607
13.206
8.8037
4.4018
0
E: Modal
Mode 4
Type: Total Deformation
Frequency: 63.556 Hz
Unit: mm
Max: 39.617
Min: 0
Max
Min

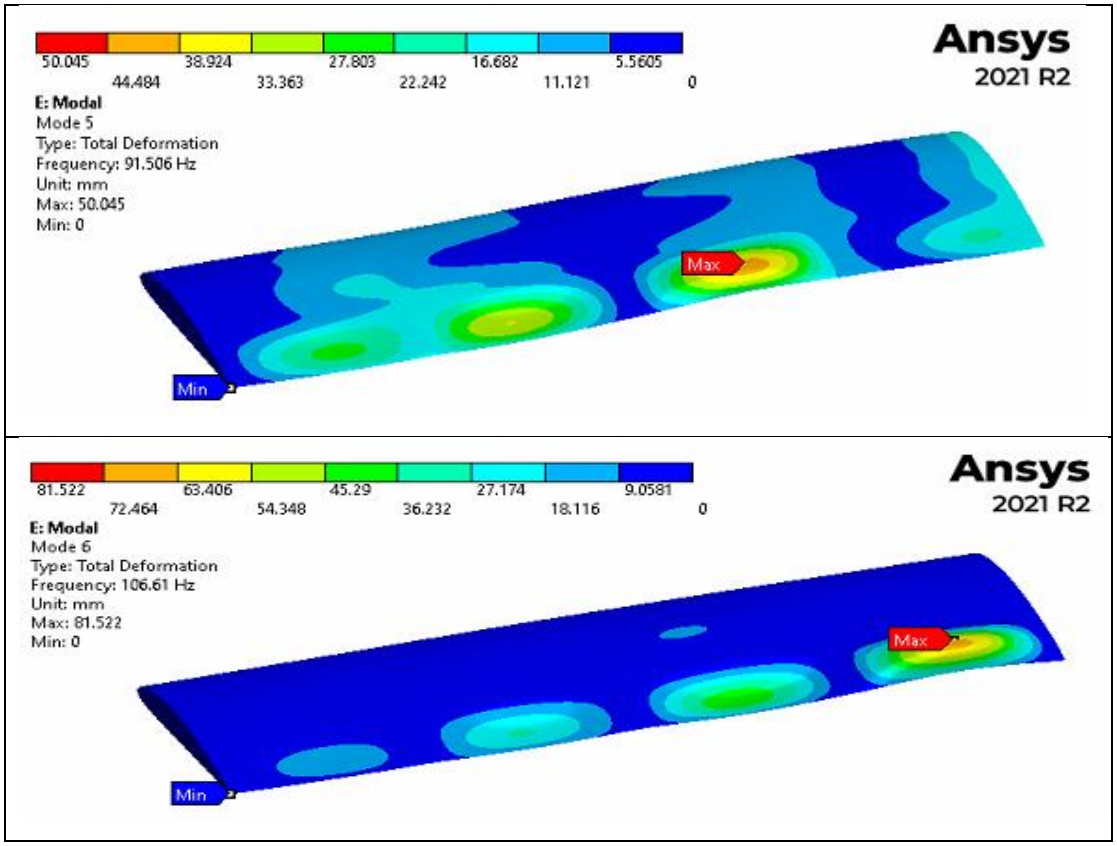
50.045
44.484
38.924
33.363
27.803
22.242
16.682
11.121
5.5605
0
Ansys
2021 R2
E: Modal
Mode 5
Type: Total Deformation
Frequency: 91.506 Hz
Unit: mm
Max: 50.045
Min: 0
Max
Min
81.522
72.464
63.406
54.348
45.29
36.232
27.174
18.116
9.0581
0
Ansys
2021 R2
E: Modal
Mode 6
Type: Total Deformation
Frequency: 106.61 Hz
Unit: mm
Max: 81.522
Min: 0
Max
Min

Case 4

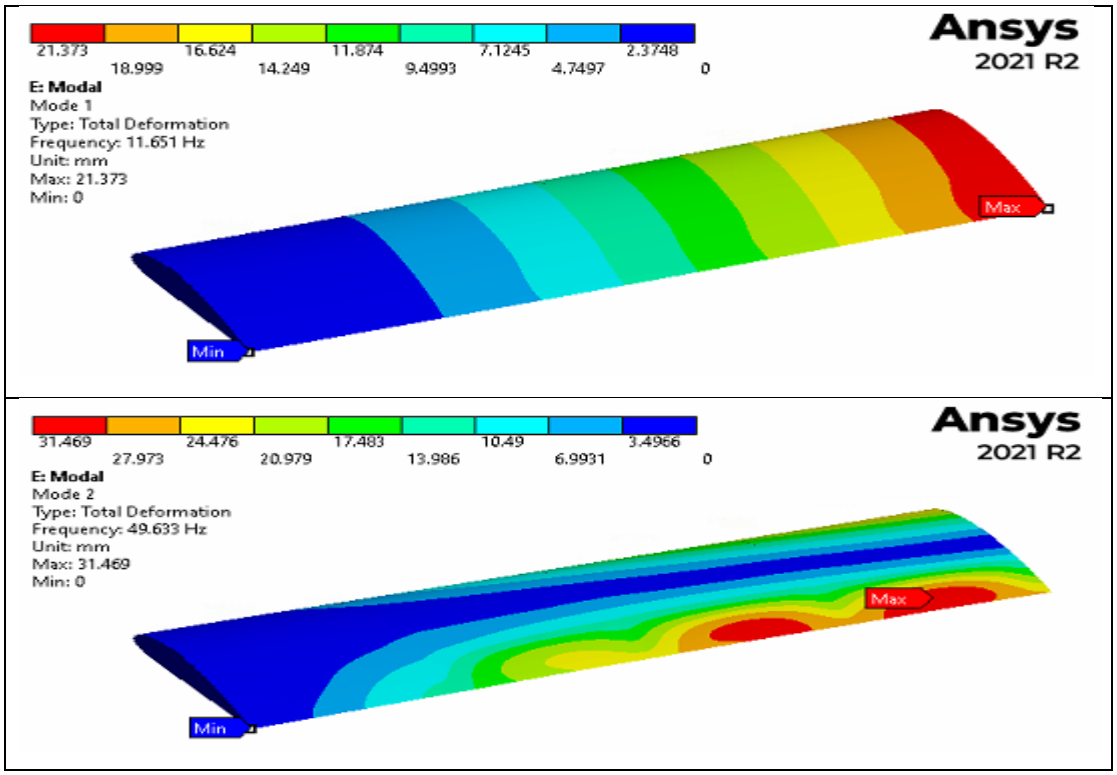
21.373
18.999
16.624
14.249
11.874
9.4993
7.1245
4.7497
2.3748
0
Ansys
2021 R2
E: Modal
Mode 1
Type: Total Deformation
Frequency: 11.651 Hz
Unit: mm
Max: 21.373
Min: 0
Max
Min
31.469
27.973
24.476
20.979
17.483
13.986
10.49
6.9931
3.4966
0
Ansys
2021 R2
E: Modal
Mode 2
Type: Total Deformation
Frequency: 49.633 Hz
Unit: mm
Max: 31.469
Min: 0
Max
Min

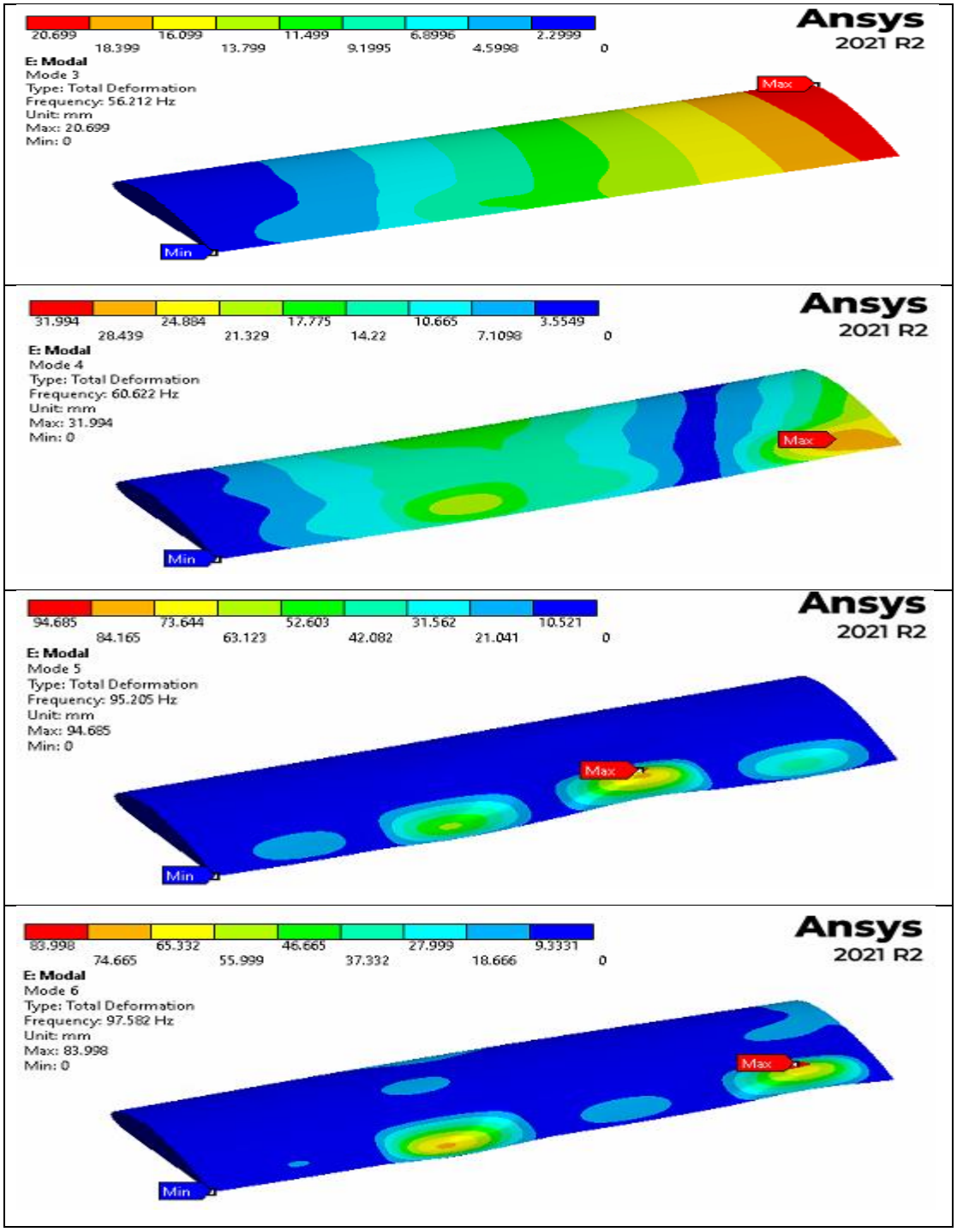
20.699
18.399
16.099
13.799
11.499
9.1995
6.8996
4.5998
2.2999
0
E: Modal
Mode 3
Type: Total Deformation
Frequency: 56.212 Hz
Unit: mm
Max: 20.699
Min: 0
Max
Min
Ansys
2021 R2
31.994
28.439
24.884
21.329
17.775
14.22
10.665
7.1098
3.5549
0
E: Modal
Mode 4
Type: Total Deformation
Frequency: 60.622 Hz
Unit: mm
Max: 31.994
Min: 0
Max
Min
Ansys
2021 R2
94.685
84.165
73.644
63.123
52.603
42.082
31.562
21.041
10.521
0
E: Modal
Mode 5
Type: Total Deformation
Frequency: 95.205 Hz
Unit: mm
Max: 94.685
Min: 0
Max
Min
Ansys
2021 R2
83.998
74.665
65.332
55.999
46.665
37.332
27.999
18.666
9.3331
0
E: Modal
Mode 6
Type: Total Deformation
Frequency: 97.582 Hz
Unit: mm
Max: 83.998
Min: 0
Max
Min
Ansys
2021 R2

Case 5

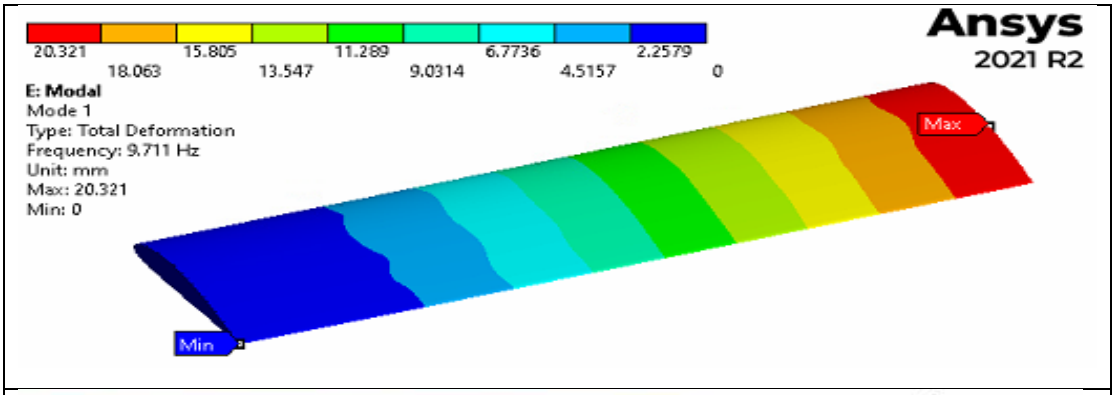
Ansys
2021 R2
20.321
18.063
15.805
13.547
11.289
9.0314
6.7736
4.5157
2.2579
0
E: Modal
Mode 1
Type: Total Deformation
Frequency: 9.711 Hz
Unit: mm
Max: 20.321
Min: 0
Max
Min

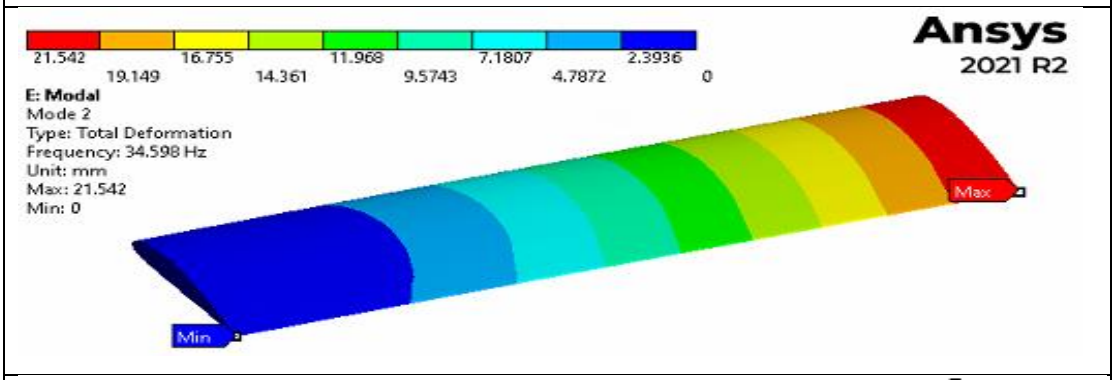
Ansys
2021 R2
21.542
19.149
16.755
14.361
11.968
9.5743
7.1807
4.7872
2.3936
0
E: Modal
Mode 2
Type: Total Deformation
Frequency: 34.598 Hz
Unit: mm
Max: 21.542
Min: 0
Max
Min

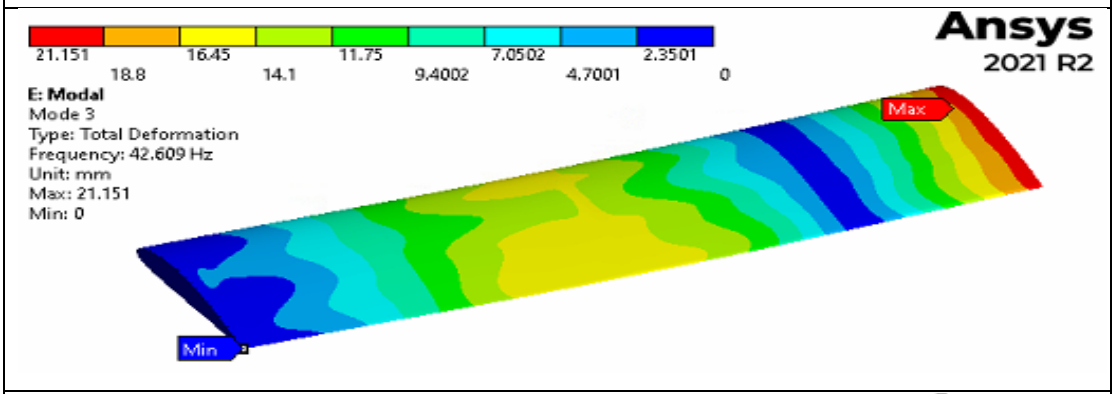
Ansys
2021 R2
21.151
18.8
16.45
14.1
11.75
9.4002
7.0502
4.7001
2.3501
0
E: Modal
Mode 3
Type: Total Deformation
Frequency: 42.609 Hz
Unit: mm
Max: 21.151
Min: 0
Max
Min

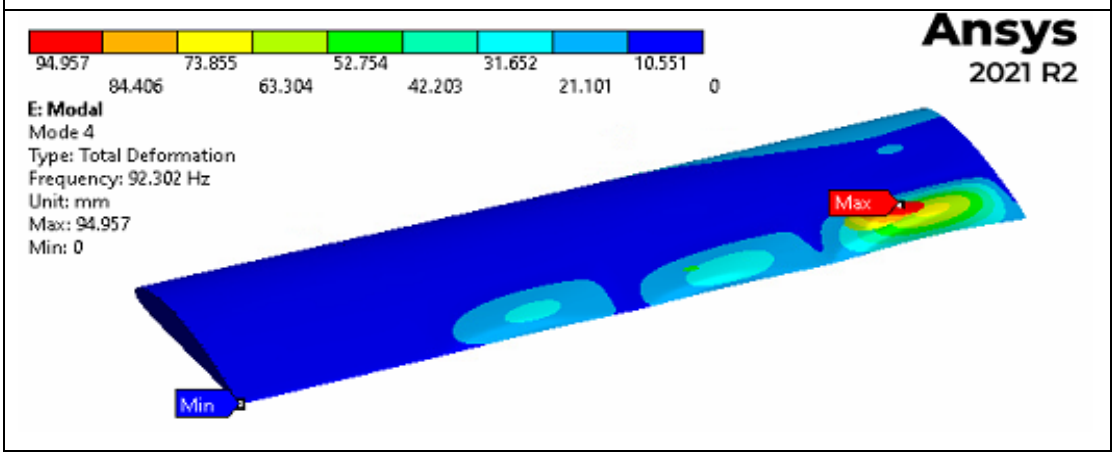
Ansys
2021 R2
94.957
84.406
73.855
63.304
52.754
42.203
31.652
21.101
10.551
0
E: Modal
Mode 4
Type: Total Deformation
Frequency: 92.302 Hz
Unit: mm
Max: 94.957
Min: 0
Max
Min

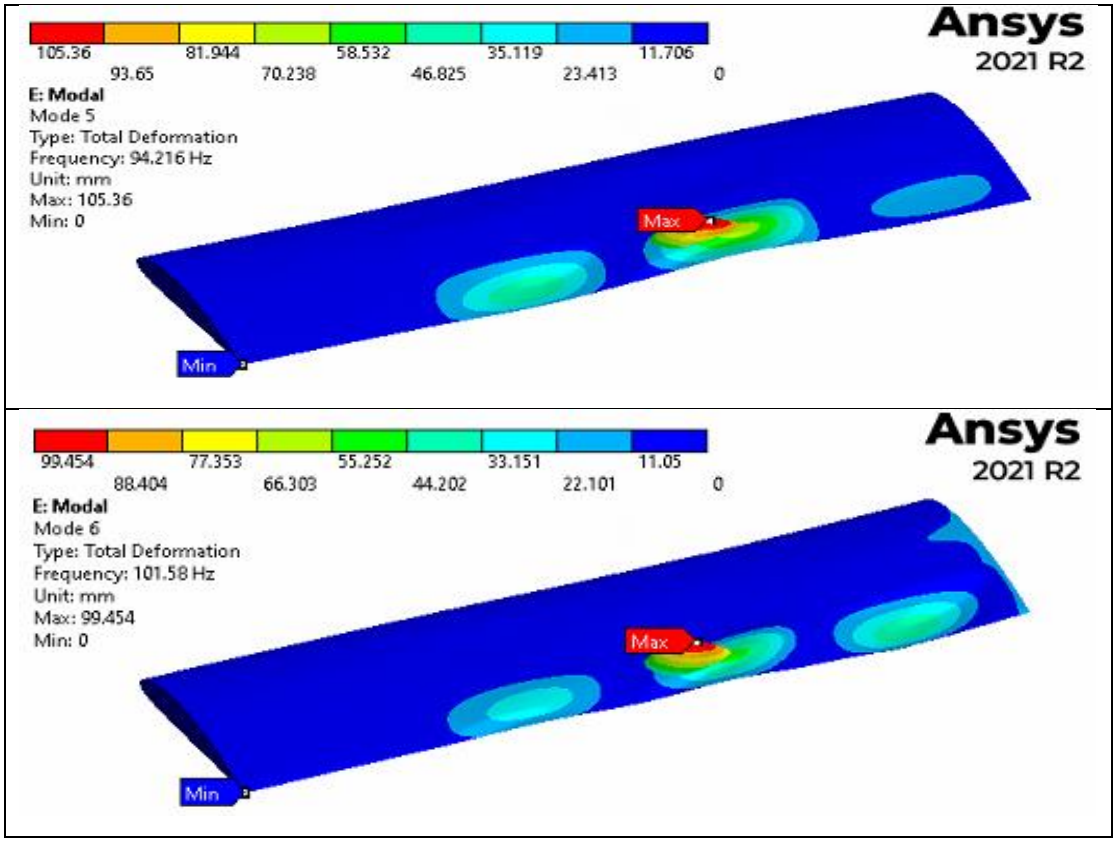
Ansys
2021 R2
105.36
93.65
81.944
70.238
58.532
46.825
35.119
23.413
11.706
0
E: Modal
Mode 5
Type: Total Deformation
Frequency: 94.216 Hz
Unit: mm
Max: 105.36
Min: 0
Max
Min
Ansys
2021 R2
99.454
88.404
77.353
66.303
55.252
44.202
33.151
22.101
11.05
0
E: Modal
Mode 6
Type: Total Deformation
Frequency: 101.58 Hz
Unit: mm
Max: 99.454
Min: 0
Max
Min